

REPRODUCTION  
COPY

2.3

---

---

# Static Load Cycle Testing of a Low-Aspect-Ratio Six-Inch Wall TRG-Type Structure TRG-4-6 (1.0, 0.25)

---

---

Prepared by C. R. Farrar, J. G. Bennett, W. E. Dunwoody, W. E. Baker

Los Alamos National Laboratory

Prepared for  
U.S. Nuclear Regulatory  
Commission

LOS ALAMOS NATIONAL LABORATORY  
3 9338 00322 0778

PLD

## AVAILABILITY NOTICE

### Availability of Reference Materials Cited in NRC Publications

Most documents cited in NRC publications will be available from one of the following sources:

1. The NRC Public Document Room, 2120 L Street, NW, Lower Level, Washington, DC 20555
2. The Superintendent of Documents, U.S. Government Printing Office, P.O. Box 37082, Washington, DC 20013-7082
3. The National Technical Information Service, Springfield, VA 22161

Although the listing that follows represents the majority of documents cited in NRC publications, it is not intended to be exhaustive.

Referenced documents available for inspection and copying for a fee from the NRC Public Document Room include NRC correspondence and internal NRC memoranda; NRC Office of Inspection and Enforcement bulletins, circulars, information notices, inspection and investigation notices; Licensee Event Reports; vendor reports and correspondence; Commission papers; and applicant and licensee documents and correspondence.

The following documents in the NUREG series are available for purchase from the GPO Sales Program: formal NRC staff and contractor reports, NRC-sponsored conference proceedings, and NRC booklets and brochures. Also available are Regulatory Guides, NRC regulations in the *Code of Federal Regulations*, and *Nuclear Regulatory Commission Issuances*.

Documents available from the National Technical Information Service include NUREG series reports and technical reports prepared by other federal agencies and reports prepared by the Atomic Energy Commission, forerunner agency to the Nuclear Regulatory Commission.

Documents available from public and special technical libraries include all open literature items, such as books, journal and periodical articles, and transactions. *Federal Register* notices, federal and state legislation, and congressional reports can usually be obtained from these libraries.

Documents such as theses, dissertations, foreign reports and translations, and non-NRC conference proceedings are available for purchase from the organization sponsoring the publication cited.

Single copies of NRC draft reports are available free, to the extent of supply, upon written request to the Office of Information Resources Management, Distribution Section, U.S. Nuclear Regulatory Commission, Washington, DC 20555.

Copies of industry codes and standards used in a substantive manner in the NRC regulatory process are maintained at the NRC Library, 7920 Norfolk Avenue, Bethesda, Maryland, and are available there for reference use by the public. Codes and standards are usually copyrighted and may be purchased from the originating organization or, if they are American National Standards, from the American National Standards Institute, 1430 Broadway, New York, NY 10018.

## DISCLAIMER NOTICE

This report was prepared as an account of work sponsored by an agency of the United States Government. Neither the United States Government nor any agency thereof, or any of their employees, makes any warranty, expressed or implied, or assumes any legal liability of responsibility for any third party's use, or the results of such use, of any information, apparatus, product or process disclosed in this report, or represents that its use by such third party would not infringe privately owned rights.

NUREG/CR-5222  
LA-11422-MS  
RD

---

---

# Static Load Cycle Testing of a Low-Aspect-Ratio Six-Inch Wall TRG-Type Structure TRG-4-6 (1.0, 0.25)

---

---

Manuscript Completed: April 1989  
Date Published: June 1989

Prepared by  
C. R. Farrar, J. G. Bennett, W. E. Dunwoody, W. E. Baker\*



Los Alamos National Laboratory  
Los Alamos, NM 87545

\*Consultant, University of New Mexico, Albuquerque, NM 87131

Prepared for  
Division of Engineering  
Office of Nuclear Regulatory Research  
U.S. Nuclear Regulatory Commission  
Washington, DC 20555  
NRC FIN A7221

LOS ALAMOS NATL. LAB. LIBS.



3 9338 00322 0778

## PREVIOUS REPORTS IN THE SERIES

E. G. Endebrock and R. C. Dove, "Seismic Response of Nonlinear Systems," Los Alamos National Laboratory report LA-8981-MS, NUREG/CR-2310 (September 1981).

E. G. Endebrock, R. C. Dove, and C. A. Anderson, "Margins to Failure - Category I Structures Program: Background and Experimental Plan," Los Alamos National Laboratory report LA-9030-MS, NUREG/CR-2347 (December 1981).

E. G. Endebrock, R. C. Dove, and W. E. Dunwoody, "Analysis and Tests on Small-Scale Shear Walls--FY 82 Final Report," Los Alamos National Laboratory report LA-10443-MS, NUREG/CR-4274 (September 1985).

R. C. Dove and J. G. Bennett, "Scale Modeling of Reinforced Concrete Category I Structures Subjected to Seismic Loading," Los Alamos National Laboratory report LA-10624-MS, NUREG/CR-4474 (January 1986).

R. C. Dove, J. G. Bennett, C. Farrar, and C. A. Anderson, "Seismic Category I Structures Program: Final Report, FY 1983-84," Los Alamos National Laboratory report LA-11013-MS, NUREG/CR-4924 (September 1987).

J. G. Bennett, R. C. Dove, W. E. Dunwoody, E. G. Endebrock, C. R. Farrar, and P. Goldman, "Simulated Seismic Tests on 1/42- and 1/14-Scale Category I, Auxiliary Buildings," Los Alamos National Laboratory report LA-11093-MS, NUREG/CR-4987 (October 1987).

J. G. Bennett, R. C. Dove, W. E. Dunwoody, C. R. Farrar, and P. Goldman, "The Seismic Category I Structures Program: Results for FY 1985," Los Alamos National Laboratory report LA-11117-MS, NUREG/CR-4998 (December 1987).

C. R. Farrar and J. G. Bennett, "Experimental Assessment of Damping in Low Aspect Ratio, Reinforced Concrete Shear Wall Structures," Los Alamos National Laboratory report LA-11325-MS, NUREG/CR-5154 (August 1988).

J. G. Bennett, R. C. Dove, W. E. Dunwoody, C. R. Farrar, and P. Goldman, "The Seismic Category I Structures Program: Results for FY 1986," Los Alamos National Laboratory report LA-11377-MS, NUREG/CR-5182 (September 1988).

## ABSTRACT

Quasi-static load cycle testing of a 6-in.-thick reinforced concrete shear wall structure is detailed in this report. The background of this program and results that led to this series of experiments are reviewed. Geometry of the test structure, design parameters, preliminary modal testing and analysis to verify undamaged dynamic properties, material property tests, instrumentation and results of this data reduction for stiffness, cracking values, and energy losses are given.

Results are compared with other investigators' results, as well as with the American Concrete Institute 318-349 code predictions.



## CONTENTS

ABSTRACT.....	iii
I. INTRODUCTION.....	1
II. BACKGROUND.....	3
III. REVIEW OF PREVIOUS STATIC TEST RESULTS OBTAINED IN THE SEISMIC CATEGORY I STRUCTURES PROGRAM.....	8
A. Isolated Shear Walls.....	8
B. 1/30-Scale, Single-Story, Diesel Generator Buildings.....	10
C. TRG-Type Structures.....	11
IV. TRG-4 Model Construction and Material Properties.....	12
V. MODAL TESTING AND RESULTS.....	17
VI. STATIC TEST SETUP AND LOAD SEQUENCE.....	25
VII. PRINCIPAL RESULTS AS REDUCED FROM THE INTERIOR GAGES AND COMPARED WITH SOM THEORY.....	27
VIII. ADDITIONAL RESULTS FROM EXTERIOR DISPLACEMENT GAGES.....	41
A. Comparison of Deformations from Relative and Absolute Displacements.....	41
B. Ratios of Deformation Components.....	52
C. Twisting Deformation.....	55
D. Motion of Shear Wall Relative to Floor and Ceiling.....	58
IX. HYSTERETIC ENERGY LOSSES IN THE TRG-4 STRUCTURE.....	63
X. OTHER INVESTIGATORS' RESULTS.....	67
XI. CONCLUSIONS.....	70
REFERENCES.....	71

## APPENDICES

A. STATISTICALLY PLANNED TEST MATRIX.....	74
B. MATERIAL PROPERTIES TEST TRG-4.....	81
C. ULTRASONIC INSPECTION OF TRG-4.....	107
D. METHODS FOR SEPARATING SHEAR AND BENDING DEFORMATION.....	114

## FIGURES

1. Prototype TRG structure.....	7
2. TRG-4 structure.....	13
3. North side layer of reinforcement in the shear wall and strain gage locations.....	14
4. South side layer of reinforcement in the shear wall and strain gage locations.....	14

FIGURES (continued)

5.	Exterior layer of reinforcement in the west end wall and strain gage locations.....	14
6.	Interior layer of reinforcement in the east end wall and strain gage locations.....	14
7.	Modal test setup.....	18
8.	Modal test excitation method.....	19
9.	Modal test measurement points.....	20
10.	Measured frequency response function Point 46-Y.....	21
11.	Measured frequency response function Point 76-Z.....	21
12.	Experimentally determined first mode.....	22
13(a)	Finite element mode shapes (only half the structure is displayed).....	22
13(b)	Comparison of an experimentally measured mode shape and the corresponding mode determined by finite element analysis.....	23
14.	Displacement transducer location.....	26
15.	Load history, force versus load step.....	26
16.	Load history, average base shear stress versus load step.....	27
17.	Force versus displacement, based on the average of the internal gage readings.....	28
18.	Force versus displacement, first 50-psi ABSS cycle, showing the actual data points connected by straight lines.....	28
19.	Force versus displacement, second 50-psi ABSS cycle. The actual data points (not shown) were connected by straight lines to produce this and subsequent plots.....	29
20.	Force versus displacement, first 100-psi ABSS cycle.....	29
21.	Force versus displacement, second 100-psi ABSS cycle.....	30
22.	Force versus displacement, third 100-psi ABSS cycle.....	30
23.	Force versus displacement, first 200-psi ABSS cycle.....	30
24.	Force versus displacement, second 200-psi ABSS cycle.....	30
25.	Force versus displacement, third 200-psi ABSS cycle.....	31
26.	Force versus displacement, failure cycle.....	31
27.	Force versus displacement, final 50-psi ABSS cycle.....	31
28.	Method for determining horizontal displacement from internal gage readings.....	32
29.	Free-body diagram of the TRG-4 structure.....	32
30.	Final crack pattern in the south side of the shear wall.....	34
31.	Final crack pattern in the north side of the shear wall.....	35
32.	The average maximum strain in the west end wall rebar during all 50-psi ABSS load cycles.....	38
33.	The average maximum strain in the west end wall rebar during all 100-psi ABSS load cycles.....	38
34.	The average maximum strain in the west end wall rebar during the 50-, 100- and 200-ABSS load cycles.....	38
35.	The average maximum vertical strain in the shear wall rebar during the 50-psi ABSS load cycles.....	39
36.	The average maximum vertical strain in the shear wall rebar during the 100-psi ABSS load cycles.....	39
37.	The average maximum strain in the shear wall rebar during the 50-psi and 100-psi ABSS load cycles.....	39



FIGURES (continued)

38.	X-component of total deformation for all load cycles based upon internal gages.....	42
39.	X-component of total deformation for all load cycles based upon external gages.....	42
40.	X-component of total deformation for the 50-psi load cycles from internal gages.....	43
41.	X-component of total deformation for the 50-psi load cycles from external gages.....	43
42.	X-component of total deformation for the 100-psi load cycles from internal gages.....	44
43.	X-component of total deformation for the 100-psi load cycles from external gages.....	44
44.	X-component of total deformation for the 200-psi load cycles from internal gages.....	44
45.	X-component of total deformation for the 200-psi load cycles from external gages.....	44
46.	X-component of total deformation for the failure load cycle from internal gages.....	45
47.	X-component of total deformation for the failure load cycle from external gages.....	45
48.	X-component of total deformation for the first cycle at each load increment from internal gages.....	46
49.	X-component of total deformation for the first cycle at each load increment from external gages.....	46
50.	X-component of shear deformation for all load cycles from internal gages.....	47
51.	X-component of shear deformation for all load cycles from external gages.....	47
52.	X-component of shear deformation for the 50-psi load cycles from internal gages.....	47
53.	X-component of shear deformation for the 50-psi load cycles from external gages.....	47
54.	X-component of shear deformation for the 100-psi load cycles from internal gages.....	48
55.	X-component of shear deformation for the 100-psi load cycles from external gages.....	48
56.	X-component of shear deformation for the 200-psi load cycles from internal gages.....	48
57.	X-component of shear deformation for the 200-psi load cycles from external gages.....	48
58.	X-component of shear deformation for the first cycle at each load increment from internal gages.....	49
59.	X-component of shear deformation for the first cycle at each load increment from external gages.....	49
60.	X-component of bending deformation for the first cycle at each load increment from internal gages.....	50
61.	X-component of bending deformation for the first cycle at each load increment from external gages.....	50
62.	Rigid body motion of model.....	51

FIGURES (continued)

63.	Total deformation for all load cycles from uncorrected external gages.....	52
64.	Total deformation for the first cycle at each load increment from uncorrected external gages.....	52
65.	Ratio of shear to total deformation from internal gages for all load cycles.....	53
66.	Ratio of shear to total deformation from external gages for all load cycles.....	53
67.	Ratio of shear to total deformation for the first cycle at each load increment from internal gages.....	54
68.	Ratio of shear to total deformation for the first cycle at each load increment from external gages.....	54
69.	Ratio of shear to total deformation for the failure load cycle from internal gages.....	54
70.	Ratio of shear to total deformation for the failure load cycle from external gages.....	54
71.	Angle of twist of the bottom edge for the 50-psi load cycles....	56
72.	Angle of twist of the bottom edge for the 100-psi load cycles....	56
73.	Angle of twist of the bottom edge for the 200-psi load cycles....	56
74.	Angle of twist of the top edge for the 50-psi load cycles.....	56
75.	Angle of twist of the top edge for the 100-psi load cycles.....	57
76.	Angle of twist of the top edge for the 200-psi load cycles.....	57
77.	Torsional deformation of the model for the 200-psi and failure load cycles.....	57
78.	Ratio of the twisting displacement to the center displacement, both at the bottom edge.....	58
79.	Ratio of the twisting displacement to the center displacement, both at the top edge.....	58
80.	Gage location for measurement of floor and ceiling motion relative to the shear wall.....	59
81.	Relative motion at the floor and shear wall interface for the 100-psi load cycle using uncorrected data.....	59
82.	Relative motion at the floor and shear wall interface for the 100-psi load cycle using uncorrected data.....	59
83.	Relative motion at the floor and shear wall interface for the 200-psi load cycle using uncorrected data.....	59
84.	Relative motion at the floor and shear wall interface for the last 200-psi load cycle and the failure cycle using uncorrected data.....	59
85.	Relative motion at the floor and shear wall interface for the 50-psi load cycle using corrected data.....	60
86.	Relative motion at the floor and shear wall interface for the 100-psi load cycle using corrected data.....	60
87.	Relative motion at the floor and shear wall interface for the 200-psi load cycle using corrected data.....	60
88.	Relative motion at the floor and shear wall interface for the last 200-psi load cycle and the failure cycle using corrected data.....	60
89.	Relative motion at the shear wall and ceiling interface for the 50-psi load cycles using uncorrected data.....	61

FIGURES (continued)

90.	Relative motion at the shear wall and ceiling interface for the 100-psi load cycles using uncorrected data.....	61
91.	Relative motion at the shear wall and ceiling interface for the 200-psi load cycles using uncorrected data.....	61
92.	Relative motion at the shear wall and ceiling interface for the last 200-psi load cycle and the failure load cycle using uncorrected data.....	61
93.	Relative motion at the shear wall and ceiling interface for the 50-psi load cycles using corrected data.....	62
94.	Relative motion at the shear wall and ceiling interface for the 100-psi load cycles using corrected data.....	62
95.	Relative motion at the shear wall and ceiling interface for the 200-psi load cycle using corrected data.....	62
96.	Relative motion at the shear wall and ceiling interface for the last 200-psi load cycle and the failure load cycle using corrected data.....	62
97.	Definitions of the quantities used to calculate the hysteretic energy loss per cycle.....	64
98.	Other investigators' results: theoretical versus measured stiffness.....	67
99.	Other investigators' results: split cylinder tensile strength versus principal stress at first cracking.....	68
100.	Other investigators' results: ACI tensile strength versus principal stress at first cracking.....	68
101.	Other investigators' results: ACI design load versus ultimate load.....	69
A-1.	Test matrix.....	76
A-2.	Testing flow chart.....	79
B-1.	Compression test set-up.....	104
B-2.	Failed compression test specimen.....	104
B-3.	Failure mode of compression test specimen.....	105
B-4.	Indirect tension test set-up.....	105
B-5.	Failed tensile test specimen.....	106
D-1.	Component of total deformation.....	116
D-2.	Displacement measurements for determining shear deformation.....	117
D-3.	Displacement measurement for determining bending deformation.....	119
D-4.	Two-dimensional finite element model of TRG-4.....	123
D-5.	Deformed shape of TRG-4 when subjected to 54,000-lb load.....	123
D-6.	Sample problem node locations.....	124
D-7.	A third method for calculating total deformations.....	127

TABLES

I.	Previous Static Test Results.....	9
II.	Measured Material Properties.....	16
III.	Ultrasonic Testing of TRG-4.....	17
IV.	Comparison of Experimental and Analytical Modal Analysis Results.....	23

TABLES (continued)

V.	The Ratio of Measured Stiffness to Stiffness Calculated by Finite Element Analysis for Various Values of $E_c$ .....	24
VI.	Theoretical Stiffness Values.....	37
VII.	Peak-To-Peak Total Deformations.....	46
VIII.	Peak-To-Peak Shear Deformations.....	49
IX.	Peak-To-Peak Bending Deformations.....	50
X.	Ratio of Shear to Total Deformation.....	55
XI.	Hysteretic Energy Losses for TRG-4.....	63
D-I.	Data from 2-D Finite Element Analysis of TRG-4.....	123

STATIC LOAD CYCLE TESTING OF A  
LOW-ASPECT-RATIO SIX-INCH WALL,  
TRG-TYPE STRUCTURE TRG-4-6  
(1.0, 0.25)

by

Charles R. Farrar,  
Joel G. Bennett,  
Wade E. Dunwoody,  
and  
William E. Baker

## I. INTRODUCTION

Previous work that has been carried out at Los Alamos National Laboratory (LANL) as part of the Seismic Category I Structures Program for the U.S. Nuclear Regulatory Commission (NRC) Office of Nuclear Regulatory Research has consistently measured stiffnesses less than strength-of-materials theory would predict in scale models of low-aspect-ratio shear wall structures subjected to working loads. In this context, working loads refer to load levels equivalent to those experienced by a structure during an operating basis earthquake, which would produce stresses on the order of 50-psi average base shear. The models tested thus far have been made of both microconcrete and conventional concrete and have been tested statically and seismically.

Upon review of these results at the Technical Review Group (TRG) meeting of April 4, 1986, it was decided to extend the experimental investigation of this reduced stiffness issue by performing a series of quasi-static load cycle tests on structures with the cross-sectional geometry of the structures previously recommended by this group (Ref. 1). The test structures were to be constructed with different aspect ratios and reinforcement percentages so that variations in these parameters that exist in actual category I structures could be taken into account in the experiments and the sensitivity to these variables could be identified.

One of the purposes of these tests was to investigate the possibility that, at equivalent stress levels, a similar reduction in stiffness occurs during static testing as has been observed during dynamic testing.\* In addition, the structures were to be instrumented so that the contribution to bending stiffness of the flexural boundary elements (shear walls in orthogonal planes) could be assessed. The structures were also instrumented so that the shear and bending contributions to the total stiffness could be measured separately. The separation of the shear and bending components of stiffness 540 intended to provide additional information concerning the mechanism for the reduction in stiffness.

A statistically planned test matrix covering height-to-length aspect ratios from 0.25 to 1.0 and percentage reinforcement ranging from 0.25% to 1.0% in each direction was developed (Appendix A). The first structure in the sequence was constructed with an aspect ratio of 1 and a percentage reinforcement of 0.25% in each direction. To remind the reader of the test geometries' basic characteristics, we will adopt the following notation:

TRG-No.-Wt (AR,%R)--sometimes abbreviated as TRG-No.--  
where,

TRG = the designation for the series of structures designed and tested using guidance from the program's Technical Review Group, a group of nationally recognized experts on nuclear structures,

---

\*Previous comparisons between static and dynamic tests of isolated shear walls, 1/30-scale, single-story, diesel generator buildings and the TRG-1 structure have shown that the reduction in stiffness was much more pronounced in dynamic tests than in static tests at similar average base shear stress levels. These structures were all small-scale microconcrete models.

- No. = the sequence number in the series,  
Wt = the shear wall thickness,  
AR = the height-to-length aspect ratio of the shear wall, and  
%R = total percentage by area of steel reinforcing in both directions.

Thus, this letter report concerns TRG-4-6 (1.0, 0.25).

A wall thickness of 6 in. was used so that reinforcement could be placed in two layers to further simulate actual shear wall construction. This report will summarize the results from this first test in the recommended statistically planned experiment set.

## II. BACKGROUND

The Seismic Category I Structures Program is being carried out at LANL under the sponsorship of the NRC's Office of Nuclear Regulatory Research and has the objective of investigating the structural dynamic response of Seismic Category I reinforced concrete structures (exclusive of containment) that are subjected to seismic loads beyond their design basis.

A number of meetings and interactions with the NRC staff have led to a set of specific program objectives, which are as follows:

1. to address the seismic response of reinforced concrete Category I structures, other than containment;
2. to develop experimental data for determining the sensitivity of structural behavior in the elastic and inelastic response range of Category I structures to variations in configuration, design practices, and earthquake loading;
3. to develop experimental data to enable validation of computer programs used to predict the behavior of Category I structures during earthquake motions that cause elastic and inelastic response;
4. to identify floor response spectra changes that occur during earthquake motions that cause elastic and inelastic structural response;
5. to develop a method for representing damping in the inelastic range and to demonstrate how this damping changes when structural response goes from the elastic to the inelastic ranges; and
6. to assess how shifts in structural frequency affect plant risk.

A principal characteristic of the typical structure under investigation is that shear rather than flexure is dominant; that is, the ratio of displacement values calculated from terms identified with shear deformation to the values contributed from bending deformation is one or greater; thus, these buildings are called "shear wall" structures.

The Seismic Category I Structures Program began in FY 1980 with an investigation that identified the typical shear wall structure of a nuclear facility and its characteristics (stiffnesses, frequencies, etc.) as areas where designers of facilities (Bechtel Corporation, Sargent & Lundy, and Tennessee Valley Authority) felt additional experimental data were needed. A combined experimental/analytical plan for investigation of the dynamic behavior of these structures was laid out as described in Ref. 2. During the first phase, the program concentrated on investigating isolated shear wall behavior using small models (1/30-scale, 1-in.-thick walls) that could be economically constructed and tested both statically and dynamically. Also, during this phase of the program, a TRG, consisting of nationally recognized seismic and concrete experts on nuclear civil structures, was established both to review the progress and to make recommendations regarding the technical directions of the program. The recommendations of this group have been evaluated in light of the needs of the NRC and, where possible, have been carefully integrated into the program.

Following the isolated shear wall phase, the program began testing and evaluating three-dimensional box-like model structures. It was recognized from the outset that scale model testing of concrete structures is a controversial issue in the U.S. civil engineering community. Thus, along with the testing of small-scale test structures, a task of demonstrating scalability of the results to prototype structures was initiated. The details and results of these investigations are reported in Refs. 3-8.

To give a brief synopsis of the situation at the end of FY 1984, the program had tested (in addition to the isolated shear walls), either statically or seismically, 23 different models representing two types of structure—a diesel generator building and an auxiliary building. Two different scales [(1/30, 1/10) and (1/42, 1/14)] of these buildings were used (1-in. and 3-in. walls). In addition, stories varied from one to three. Although a number of results on items, such as aging (cure time) and effect of increasing seismic magnitude, have been reported, two important and consistent conclusions came



out of the data from these tests. First, the scalability of the results was illustrated both in the elastic and inelastic range. Second, the so-called "working load" secant stiffness of the models was lower than the computed uncracked cross-sectional values by a factor of about 4.

During their review, the TRG pointed out the following:

1. Design of prototype nuclear plant structures is normally based upon an uncracked cross-section strength-of-materials approach that may or may not use a "stiffness reduction factor" for the concrete. But, if such a factor is used, it is never as large as 4.
2. Although the structures themselves appear to have adequate reserve margin (even if the stiffness is only 25% of the theoretical), any piping and attached equipment will have been designed using inappropriate floor response spectra.
3. Given that a nuclear structure designed to have a natural response of about 15 Hz really has a natural frequency of 7.5 Hz (corresponding to a reduction in stiffness of 4) and allowing further that the natural frequency will decrease because of degrading stiffness, the natural response of the structure will shift well down into the frequency range for which an earthquake's energy content is the largest. This will result in increased amplification in the floor response spectra at lower frequencies, and this fact potentially has significant impact on the equipment and on the piping design response spectra and their margins of safety.

All three points are related to the difference between the measured and calculated stiffnesses of these structures.

Having made these observations, several questions arose. Did our previous experimental data taken on microconcrete models represent behavior that would be observed in prototype structures? What is the appropriate value of the stiffness that should be used in design and for component response spectra computations in these structures? Should this value be a function of load level? Have the equipment and piping in existing buildings been designed to inappropriate response spectra?

Thus, the primary program emphasis at that time was to ensure the credibility of previous experimental work by beginning to resolve the "stiffness difference" issue. The TRG for this program believed that this important issue had to be addressed before the program objectives could be accomplished.

To address these stiffness-related concerns, it was agreed that a series of credibility experiments should be carried out using both large- and small-scale structures. For the large-scale structure, the TRG set limitations on the design parameters. The recommended "ideal" structure characteristics, in order of decreasing priority, were as follows:

1. maximum predicted bending and shear mode natural frequency  $\leq 30$  Hz,
2. minimum wall thickness = 4 in.,
3. height-to-depth ratio of shear wall  $\leq 1$ ,
4. use of actual No. 3 rebar for reinforcing,
5. use of realistic material for aggregate,
6. use of 0.1-1% steel (0.3% each face, each direction, i.e., 0.6% total each direction), and
7. use of water-blasted construction joints to ensure good aggregate interlock.

A prototype "TRG" structure designed to comply with these specifications (Fig. 1) was constructed using actual batch plant concrete and No. 3 rebar. In addition, a 1/4-scale model of the TRG structure was constructed with microconcrete and wire mesh rebar and was tested before the prototype was constructed. Both structures were tested statically and then seismically to failure or, in the case of the prototype, to machine limits. The 1/4-scale model was TRG-1-1 (1.0, 0.6), and the prototype was TRG-3-4 (1.0, 0.56). A second 1/4-scale model, TRG-2-1 (1.0, 0.6), was constructed and partially tested. That model had obvious visual flaws (cracked sections) upon form removal and was never fully tested or reported.

These tests were intended to show that the previously observed reductions in stiffness were not related to the use of microconcrete and that the static and dynamic test results of the microconcrete models could be scaled to conventional concrete structures.

During the static tests, the 1/4-scale model, TRG-1-1 (1.0, 0.6), showed results similar to those of the prototype, TRG-3-1 (1.0, 0.56), for stiffness and suggested that, for low-level static response, the microconcrete model did an adequate job of predicting the response of the conventional concrete prototype. A low-force-level experimental modal analysis performed before seismic excitation showed results concerning stiffness and scalability similar to those of the static test.

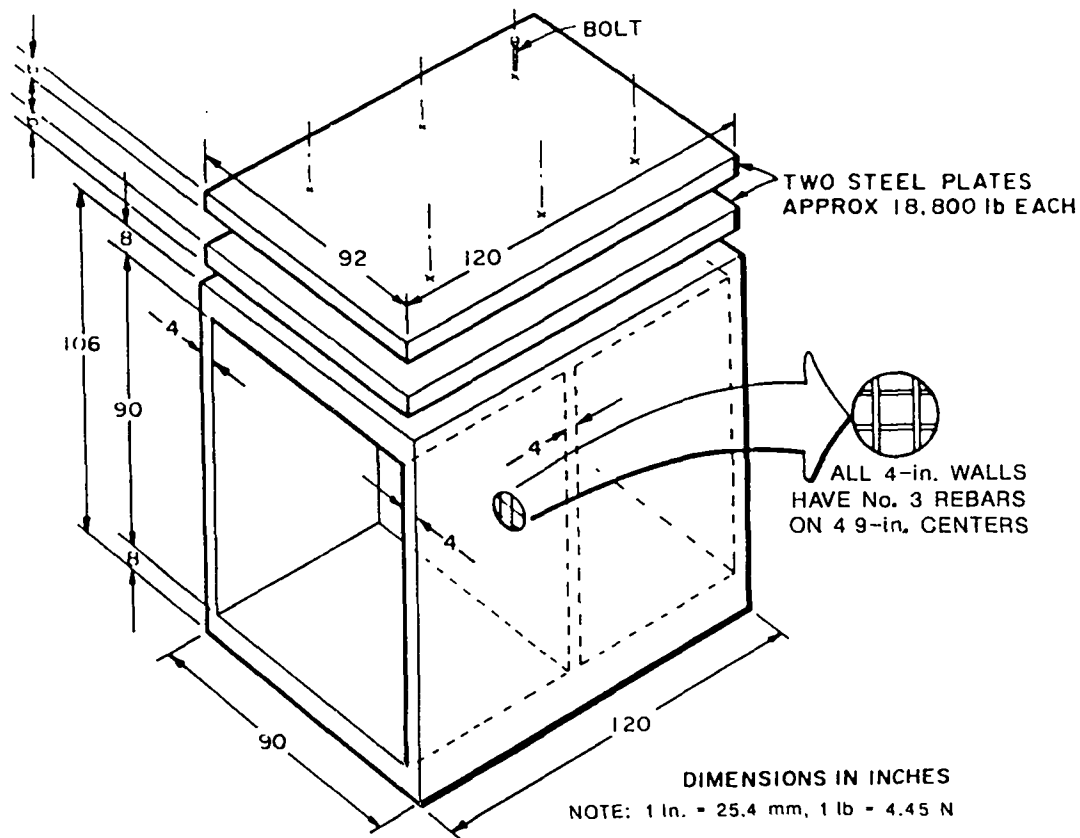


Fig. 1. Prototype TRG structure.

When the structures were tested dynamically on a shake table, both models showed reductions in stiffness consistent with previous test data, implying that the reduced stiffness could not be attributed to microconcrete. The prototype TRG structure with its added mass was too large to make reproduction of the input signal possible. This input signal was a scaled version of the one used on the 1/4-scale model, and, because it could not be accurately reproduced (frequency content of the signal was distorted), conclusions concerning the scalability of seismic response between the conventional concrete prototype and the microconcrete model could not be made. The results of these tests appear in detail in Refs. 5 and 8.

At the TRG meeting on December 19, 1986, the group suggested that a reduced statistical plan be carried out. The TRG was not concerned with the technical merit of the matrix of Appendix A but rather with the time and cost required to successfully complete the test matrix. The TRG was also concerned

with the deviation from original program objectives. The TRG suggested that one other model with an aspect ratio of 0.25 be statically tested, as well as a model identical to TRG-3-4 (1.0, 0.56), and this plan was adopted.

### III. REVIEW OF PREVIOUS STATIC TEST RESULTS OBTAINED IN THE SEISMIC CATEGORY I STRUCTURES PROGRAM

Previously in this program, measured stiffness values from static and dynamic tests have been compared with theoretical values that were determined using a modulus of elasticity calculated from the empirical formula in American Concrete Institute (ACI) 349-85.<sup>9</sup> This empirical formula generally gave a higher value for the concrete's modulus than was measured from test specimens. In the following summary of previous test results, theoretical stiffness values were determined using measured moduli. This investigation is concerned with determining the proper values of stiffness to be used in the analysis of Seismic Category I structures; hence, it is felt that the best estimate of actual material properties should be used when experimental results are compared with theory. The previously reported comparisons between measured and theoretical stiffness do, however, provide information concerning errors that could occur during the design process when material properties have yet to be measured. Table I summarizes the previous results using both the measured and design values for the concrete's modulus.

#### A. Isolated Shear Walls

The first static tests were performed on single-story isolated shear walls and were reported in Ref. 3. Five walls were tested, two monotonically and three cyclically. These specimens were made with microconcrete and wire mesh reinforcement. The amount of reinforcement at the interface of the shear wall base and shear wall top plate was varied along with the amount of moment reinforcement in the form of threaded steel rods located at the ends of the shear wall.

All specimens remained essentially linear up to a load producing an average base shear stress (ABSS) of 200 psi and a principal tensile stress (PTS) of 600 psi or more. The load at first cracking, as predicted from a strength-of-materials approach, agreed very well with the measured cracking strength of the walls and the average split cylinder tensile strength of 666 psi. Also, when the walls were subjected to repeated load cycles below the first cracking

TABLE I  
PREVIOUS STATIC TEST RESULTS

	Measured Stiffness before Cracking (lb/in.) 1	Ultimate <sup>a</sup> Compressive Strength $f_c$ (ksi)	Theoretical <sup>b</sup> Stiffness Using Measured Modulus (lb/in.) 2	Theoretical <sup>b</sup> Stiffness Using ACI Empirical Modulus (lb/in.) 3	Ratio of Columns		
					$\frac{2}{1}$	$\frac{3}{1}$	$\frac{2}{3}$
Isolated Shear Walls:							
1	$0.78 \times 10^6$	4.34	$1.60 \times 10^6$	$2.33 \times 10^6$	2.05	2.99	0.69
2	$0.79 \times 10^6$	5.89	-	$2.71 \times 10^6$	-	3.43	-
3	$1.0 \times 10^6$	7.35	$1.90 \times 10^6$	$3.03 \times 10^6$	1.90	3.03	0.63
4	$1.06 \times 10^6$	6.86	-	$2.92 \times 10^6$	-	2.75	-
5	$0.87 \times 10^6$	6.31	$1.75 \times 10^6$	$2.80 \times 10^6$	2.02	3.22	0.63
1/30-scale, 1-Story, Diesel Generator Buildings:							
3D-2	$0.76 \times 10^6$	2.70	$2.25 \times 10^6$	$2.90 \times 10^6$	2.96	3.82	0.78
3D-4	$1.74 \times 10^6$	3.32	$4.82 \times 10^6$	$6.08 \times 10^6$	2.77	3.49	0.79
3D-7	$0.92 \times 10^6$	2.35	$2.45 \times 10^6$	$2.71 \times 10^6$	2.66	2.95	0.90
3D-8	$0.80 \times 10^6$	2.30	$2.36 \times 10^6$	$2.68 \times 10^6$	2.95	3.35	0.88
3D-9	$1.67 \times 10^6$	2.69	$4.62 \times 10^6$	$5.47 \times 10^6$	2.77	3.27	0.84
3D-10	$1.14 \times 10^6$	3.27	-	$3.19 \times 10^6$	-	2.80	-
3D-11	$0.92 \times 10^6$	3.09	-	$3.11 \times 10^6$	-	3.38	-
3D-12	$1.23 \times 10^6$	2.05	-	$2.53 \times 10^6$	-	2.06	-
3D-13	$0.88 \times 10^6$	2.04	-	$2.52 \times 10^6$	-	2.86	-
3D-19	$0.80 \times 10^6$	4.70	-	$3.83 \times 10^6$	-	4.79	-
3D-20	$1.08 \times 10^6$	4.30	$3.22 \times 10^6$	$3.65 \times 10^6$	2.98	3.38	0.88
TRG-1	$0.92 \times 10^6$	3.77	$1.2 \times 10^6$	$1.3 \times 10^6$	1.25	1.38	0.92
TRG-3	$4.4 \times 10^6$	3.81	$3.0 \times 10^6$	$5.0 \times 10^6$	0.68	1.13	0.60

<sup>a</sup>The empirical modulus,  $E_{C_{ACI}}$ , is  $57,000 \sqrt{f'_c}$ , and the measured modulus,  $E_{C_m}$ , can be computed by the following formula:

$$E_{C_m} = 57,000 \sqrt{f'_c} \left( \frac{\text{Stiffness Col. 2}}{\text{Stiffness Col. 3}} \right)$$

<sup>b</sup>Based on the gross section.

load, there was no evidence of stiffness degradation or of increase in the area of the hysteresis loop for a given load level. Above the first cracking load, stiffness degraded and the area of the hysteresis loop increased with increased load and increased cycles at a constant load. The ultimate strength of the walls exceeds the provisions for shear capacity as determined by ACI 349-85 11.10. The measured stiffnesses in the linear region were down by a factor of 1.90 to 2.05 from the calculated uncracked cross-section stiffness using a measured modulus.

When normalized to a common modulus of elasticity, these static stiffness values can be compared with those measured dynamically during sine sweep and simulated seismic tests of similar models. At force levels that were 10% of the load required to produce first cracking in the static test, stiffness measured during both the sine sweep and simulated seismic tests were reduced considerably from the static tests and even further reduced from the calculated uncracked cross-section value. The sine sweep and seismic stiffness values were lower by an average factor of 6.95 and 3.85 from the calculated uncracked value, respectively, and down by an average factor of 2.93 and 1.86 from the average measured static value.

#### B. 1/30-Scale, Single-Story, Diesel Generator Buildings

Eleven 1/30-scale, single-story, diesel generator buildings were statically tested to failure and are reported in Ref. 4. Nine models were tested monotonically, eight in the transverse direction and one in the longitudinal direction. Two models were tested cyclically, one each in the transverse and longitudinal directions. These specimens were all made with microconcrete and wire mesh reinforcement. Other than the direction of applied load, the only parameters that were varied in these tests were the amount of cure time each model experienced before testing and the distance the reinforcement was embedded in the base of the structure.

As with the isolated shear walls, all specimens remained linear up to the load that produced cracking. This load produced an ABSS on the order of 200 psi and a PTS on the order of 340 psi. At a given load level below the first cracking load, the area under the hysteresis loop remained constant when the load was cycled, and the stiffness remained constant. Above the cracking load, stiffness again was observed to degrade, and the area of the hysteresis loop increased either with increases in load level or increases in the number

of load cycles. The load at first cracking was in good agreement with the value predicted from strength of materials and with the measured tensile stress of the concrete. Provisions for the shear capacity of the walls from ACI 349-85 were exceeded. Stiffness based on a secant from the origin to half the ultimate load were down by factors ranging from 2.7 to 3.0 when compared with the calculated stiffness, based upon an uncracked cross-section and a measured modulus.

When similar models were tested dynamically with a 0.5-g peak acceleration random input, producing an ABSS of 6.3 psi and a PTS of 10.6 psi, the models were again found to behave with a stiffness down by a factor of 2.9 to 3.8 from the strength-of-materials prediction using a measured modulus.

The moment of inertia used in the calculated stiffness value considered the entire end wall to contribute to the flexural stiffness of the shear wall, and the modulus of elasticity was based upon the measured values. No effect from cure time or embedment length was observed.

### C. TRG-Type Structures

TRG-3 and its two 1/4-scale models, TRG-1 and -2, were tested statically and monotonically at low-load levels that produced an ABSS of 28 psi and a PTS of 40 psi on TRG-3 and an ABSS of 53 psi and a PTS of 80 psi on TRG-1 and -2. These tests were repeated several times and were intended to identify the initial stiffness condition of each model while introducing a minimum amount of damage into the test structure. TRG-3 was constructed with conventional concrete and No. 3 rebar, and TRG-1 and -2 were made with microconcrete and wire mesh reinforcement.

TRG-3 showed a measured stiffness down by a factor of 1.54 from theory, and TRG-1 showed a reduction of 1.25 from theory. In both cases, the theoretical stiffness was computed with a measured value of  $E_c$ . (TRG-2 was found to have significant shrinkage cracks, and results from this model were not considered meaningful.) When properly scaled, the static stiffness values for the two models were in reasonable agreement, showing that stiffness can be scaled from microconcrete to conventional concrete in this low-load-level region. Following static testing, both TRG-1 and TRG-3 were also tested seismically and dynamically. When TRG-1 was subjected to a 0.5-g peak acceleration random input, it responded with a stiffness that was down by a factor of 2.6 from theory even though this excitation produced only 16.3 psi

ABSS and 16.6 psi PTS. Similar stiffness values were obtained during a 0.5-g seismic test. TRG-3 responded to a 0.73-g seismic test with a stiffness that was down by a factor of 4.0 from theory at an ABSS of 91 psi and a PTS of 92 psi.

#### IV. TRG-4 MODEL CONSTRUCTION AND MATERIAL PROPERTIES

A primary concern in construction of this model was that it require a minimum amount of handling once it was built. This requirement would eliminate questions about damage caused by handling as a possible source of any measured reduction in stiffness. Thus, the model was constructed in place on the base of the load frame that was to be used in the cyclic testing. The load frame was designed to keep maximum base deflections less than 0.001 in. The frame was located in an indoor test facility so that construction, concrete placement, curing, and testing of the model could be performed in a controlled environment.

The reinforcement in both the shear walls and the end walls consisted of No. 3 (3/8-in. diameter) rebar with a specified minimum yield strength of 60,000 psi. The bars were spaced at 14.5 in. on center near both faces of the walls, providing two staggered layers of reinforcement in both the horizontal and vertical direction as shown in Fig. 2. Both the amount of horizontal and vertical reinforcement (0.25% by area, each direction) are the minimum allowed by ACI 349-85, 11.10.9.2 and 11.10.9.4. Unless otherwise stated, compliance with a section of ACI 349 implies compliance with the same section in ACI 318.<sup>10</sup>

As shown in Fig. 2, a minimum 1 in. of cover was provided for all reinforcement. This amount exceeds the cover requirements of ACI 349-85, 7.7 for interior walls, but did not meet the required 1.5-in. cover for exterior walls. However, because this model would remain indoors, it was believed that the 1.0-in. cover was sufficient and that the structural properties of the wall would not be adversely affected.

The top and bottom slabs were heavily reinforced with two layers of No. 4 rebar spaced at 6 in. on center. In addition to meeting the reinforcing requirements of ACI 349, the reinforcement met the special provisions for seismic design of ACI 318-83, Appendix A, except at the interface of the shear



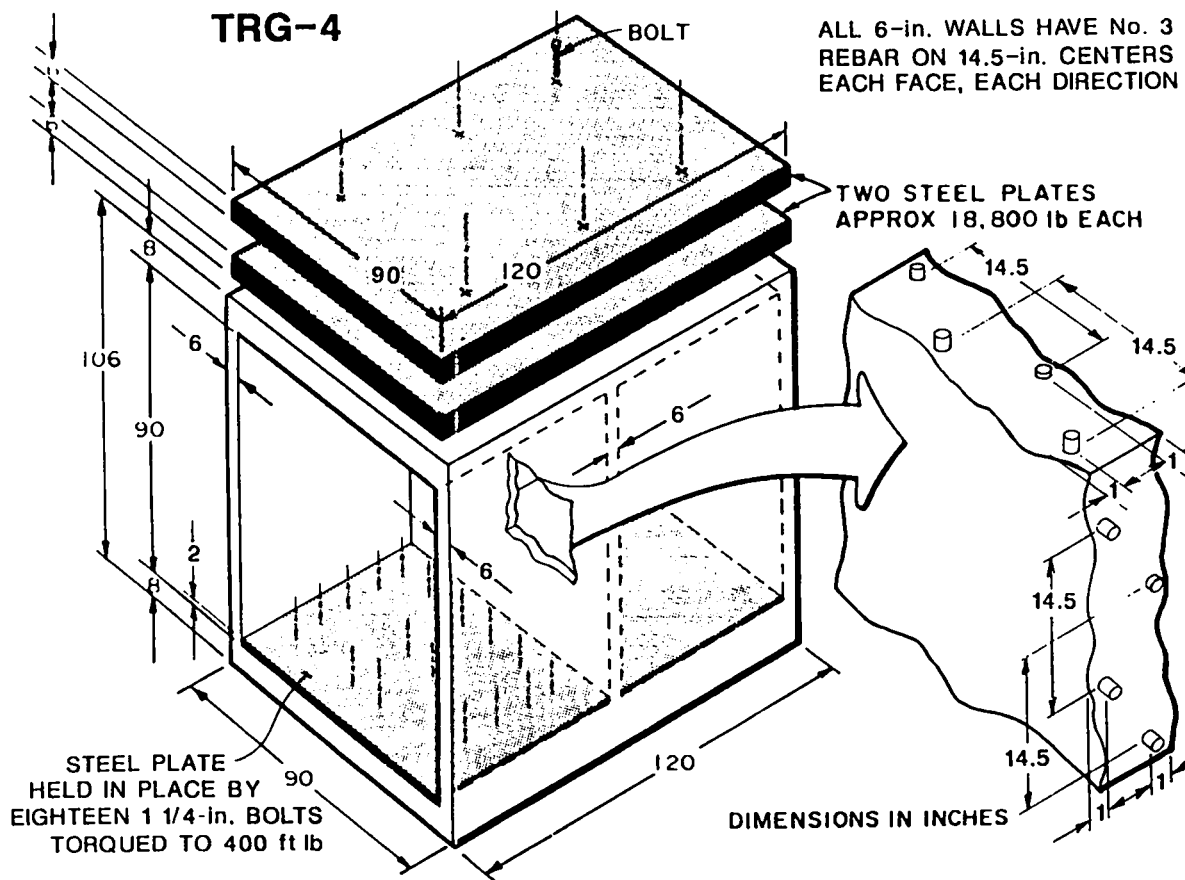


Fig. 2. TRG-4 structure.

wall and end wall. ACI 318-83 has special provisions for reinforcing this area that are new to the code. However, it is felt that existing Seismic Category I structures, all of which were designed before the adoption of ACI 318-83, would not have invoked this criterion.

Before placing the concrete, 30 Eaton weldable strain gages were attached to the reinforcement at the locations shown in Figs. 3-6. The gages were wrapped with fiberglass tape and coated with caulk to prevent damage caused by compaction and moisture.

Next, form work was put into place on top of the load frame base. The bottom 18 in. of the interior wall forms were made of plexiglass so that the



concrete placement and compaction could be visually monitored in this structurally critical region. The concrete was placed on December 9, 1986; the first truck arrived at 9:00 a.m. containing 3 yd<sup>3</sup> of concrete. Slump from this truck was measured per ASTM C143-78<sup>11</sup> and was found to be 3-1/2 in. After difficulties occurred with the hopper used to transport the concrete from the mixer to the model, 9 gal. of water were added to the mix, increasing the slump to 5 in. This batch of concrete was used to pour the base and was then thoroughly compacted with mechanical vibrators. Fourteen standard 6-in.-diameter by 12-in.-high concrete cylinders were taken during the middle of this placement per ASTM standards C172-82<sup>12</sup> and C31-84.<sup>13</sup> The second truck arrived at 11:15 a.m., approximately a half hour after the placement of concrete from the first truck was complete. This truck contained 5-1/2 yd<sup>3</sup> of concrete. Initially, slump from the second truck was measured at 3 in., and, after adding 5 gal. of water to the mix, the slump was measured at 3-1/2 in. The concrete from this second truck was used to complete the model. Again, 14 test specimens were taken during the middle of the placement.

The concrete was specified as minimum 3000-psi ultimate compressive strength. Five and one-half sacks of cement were used per cubic yard of concrete, and the cement was Ideal Type 1-2 low alkali. The coarse aggregate was 0.75-in. maximum, crusher run, Rio Grande river rock, and the fine aggregate was No. 4 sand with gradation conforming to ASTM C33-85.<sup>14</sup>

The test cylinders were removed from their forms and were placed in a curing chamber approximately 80 hr after they had been poured and remained in the chamber for the next 30 days. Forms were left on the model until January 6, 28 days after the model was poured. The exposed surfaces of both the top and bottom slab were kept moist and covered with tarps during this 28-day period.

The test cylinders were taken to Albuquerque Testing Laboratories (ATL), where they were tested on January 23-26, 1987, 45 days after they were originally cast. To avoid damage to the specimens while in transit to Albuquerque, a foam-lined transportation box was constructed and foam was placed between each of the individual cylinders. The tests included ultimate compressive strength (ASTM C39-84),<sup>15</sup> modulus of elasticity (ASTM C469-83),<sup>16</sup> split cylinder tensile strength (ASTM C496-85)<sup>17</sup> and density. Ten specimens from each truck were tested for ultimate compressive strength and modulus of elasticity, and four specimens from each truck were tested for tensile

strength. The specimens were weighed to the nearest 0.01 lb. The results of the tests are summarized in Table II, and the report from the testing lab is included as Appendix B.

TABLE II  
MEASURED MATERIAL PROPERTIES

	Density (lb/ft <sup>3</sup> )	<sup>a</sup> Ultimate Compressive Strength (psi)	<sup>b</sup> Tensile Strength (psi)	<sup>c</sup> Modulus of Elasticity (psi)	57,000 $\sqrt{f'_c}$ <sup>d</sup> (psi)	$33w^{3/2} \sqrt{f'_c}$ <sup>d</sup> (psi)
Average Truck 1	137	3936	350	3.09x10 <sup>6</sup>	3.58x10 <sup>6</sup>	3.33x10 <sup>6</sup>
Minimum	136	3767	302	2.96x10 <sup>6</sup>	3.50x10 <sup>6</sup>	3.25x10 <sup>6</sup>
Maximum	138	4173	384	3.19x10 <sup>6</sup>	3.68x10 <sup>6</sup>	3.42x10 <sup>6</sup>
Average Truck 2	139	4368	364	3.36x10 <sup>6</sup>	3.77x10 <sup>6</sup>	3.58x10 <sup>6</sup>
Minimum	138	3961	348	3.11x10 <sup>6</sup>	3.59x10 <sup>6</sup>	3.40x10 <sup>6</sup>
Maximum	140	4562	386	3.71x10 <sup>6</sup>	3.85x10 <sup>6</sup>	3.65x10 <sup>6</sup>
Ave. Both Trucks	138	4152	357	3.23x10 <sup>6</sup>	3.67x10 <sup>6</sup>	3.45x10 <sup>6</sup>

<sup>a</sup> Measured on 6-in.-diameter x 12-in. specimens per ASTM C39-84.

<sup>b</sup> Measured on 6-in.-diameter x 12-in. specimens per ASTM C496-85.

<sup>c</sup> Measured on 6-in.-diameter x 12-in. specimens per ASTM C469-83.

<sup>d</sup> Modulus of elasticity determined per ACI 349-85, 8.5.1.

On January 15, 1987, Luke Snell, a faculty member at Southern Illinois University and an experienced independent consultant in the field of ultrasonic testing of reinforced concrete structures, performed an ultrasonic test on the model. He began by visually inspecting the model for surface cracks and found none. Next, he calibrated his testing equipment with a standard steel specimen and proceeded to test the 6-in.-diameter by 12-in.-long test specimens. The test consisted of applying an audio pulse to the end of the specimen and measuring the time required for that pulse to travel over the distance of the specimen. From this information, the speed of sound in the concrete can be estimated and defects in the concrete can be identified when the speed is altered as the sound wave cannot travel across a void but, rather, must go around it. The cylinders from the two different trucks showed no significant difference in pulse speed, and tests at different locations on the model that were known to contain concrete from the different trucks showed no significant difference in pulse velocity. Pulse velocities were determined at 185 locations on the model, and the results are summarized in Table III. From these results, Mr. Snell concluded that the model showed no signs of defects and that material properties determined from the cylinder test specimens would indeed be indicative of the properties of the TRG-4 structure. Mr. Snell's test report is included as Appendix C.

TABLE III  
ULTRASONIC TESTING OF TRG-4

	Cylinders	Shear Wall	West End Wall	East End Wall	Top *	Base *
Average Pulse Velocity (ft/s)	13,290	13,260	13,235	13,270	14,190	14,770

\* The increased velocities in the top and base were caused by the large amount of reinforcing steel in each of these slabs.

Other investigations, Ref. 18, have correlated the speed of sound in concrete to the static modulus of elasticity. However, these investigations do not specify the type of static modulus (that is, initial tangent, secant to 40% of ultimate, etc). A similar correlation, made by interpolating between the data points in Ref. 18 with the results of Mr. Snell's test, yield an average modulus of  $3.2 \times 10^6$  psi for the TRG-4 structure.

#### V. MODAL TESTING AND RESULTS

The first test performed on the TRG-4 structure was a low-load-level experimental modal analysis. This test was used to characterize the initial stiffness of the model without introducing damage and to demonstrate that the dynamic properties of the structure could be accurately measured at very low load levels. Also, these tests provided an indirect measure of the concrete's modulus of elasticity. Two test setups were tried with the intent of obtaining free-boundary conditions. Both set-ups are depicted in Fig. 7.

The first attempt at obtaining free-boundary conditions was to suspend the model with nylon straps from an overhead crane. This test configuration proved difficult in that it was hard to align the structure with the shaker because of the coarseness of the control system of the crane. Also, when technicians had to climb on the model to move accelerometers, the motion induced by their movement did not dampen out readily.

The second configuration consisted of supporting the model by placing five air bearings under its base. This configuration was considerably better because it was much easier to adjust the height of the model by changing the

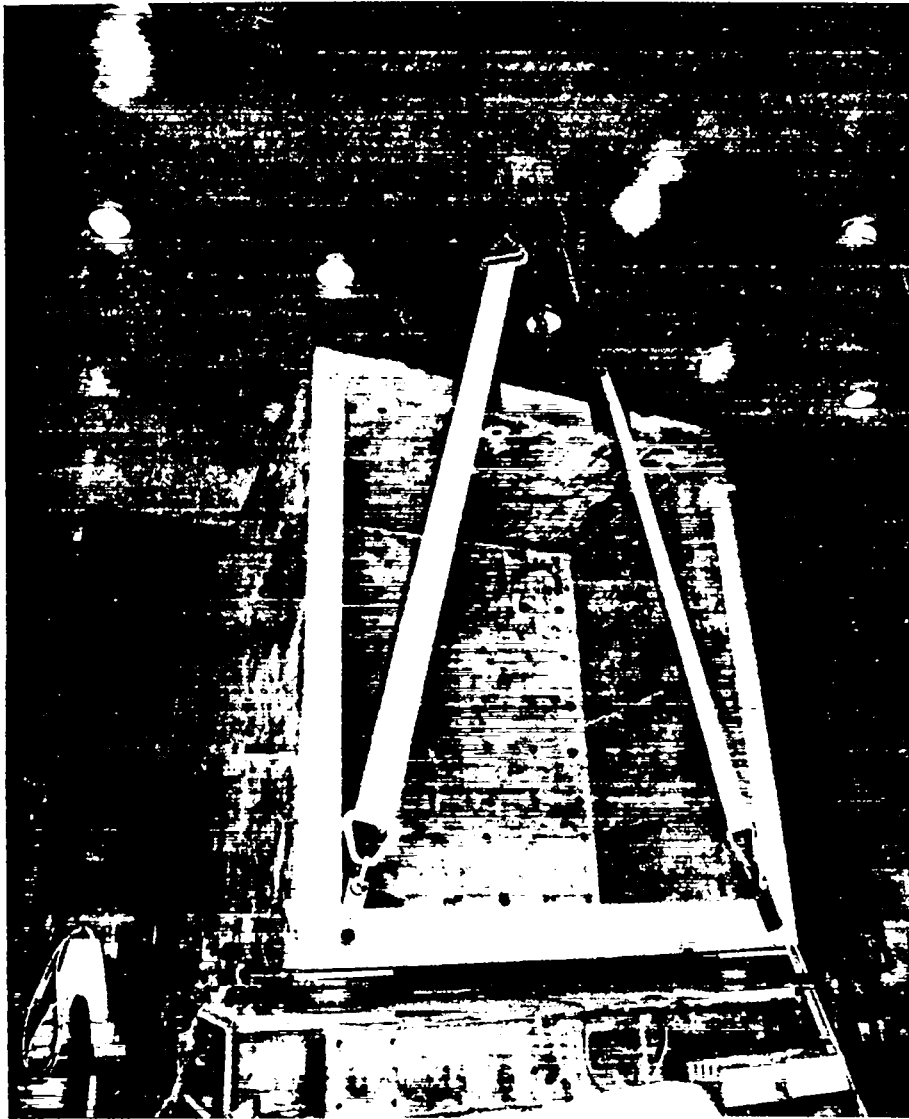


Fig. 7. Modal test setup.

pressure in the air bearings, and the motion caused by people walking on the model dampened out much faster. Both test configurations gave identical values for the fundamental frequency of the structure. Free-boundary conditions were chosen because they can be most accurately compared with analytical results from either finite element analysis (FEA) or strength-of-materials (SOM) analysis.

A 300-lb-peak force shaker was attached using a "stinger," a thin rod that can transmit only axial force, to the northwest end wall 4 in. from the bottom, as shown in Fig. 8. A transducer, located between the shaker's stinger and the model, measured force as the input quantity. A random excitation signal with a uniform power spectral density between 0 and 200 Hz was used to drive the shaker. Acceleration response was measured in three orthogonal directions at 89 points on the structure. The measurement points are shown in Fig. 9 (as the intersections of two or more lines), along with the excitation point.

The force input and acceleration responses were recorded, transformed into the frequency domain, and analyzed with a commercially available experimental modal analysis software package. Coherence functions showed that the 300-lb

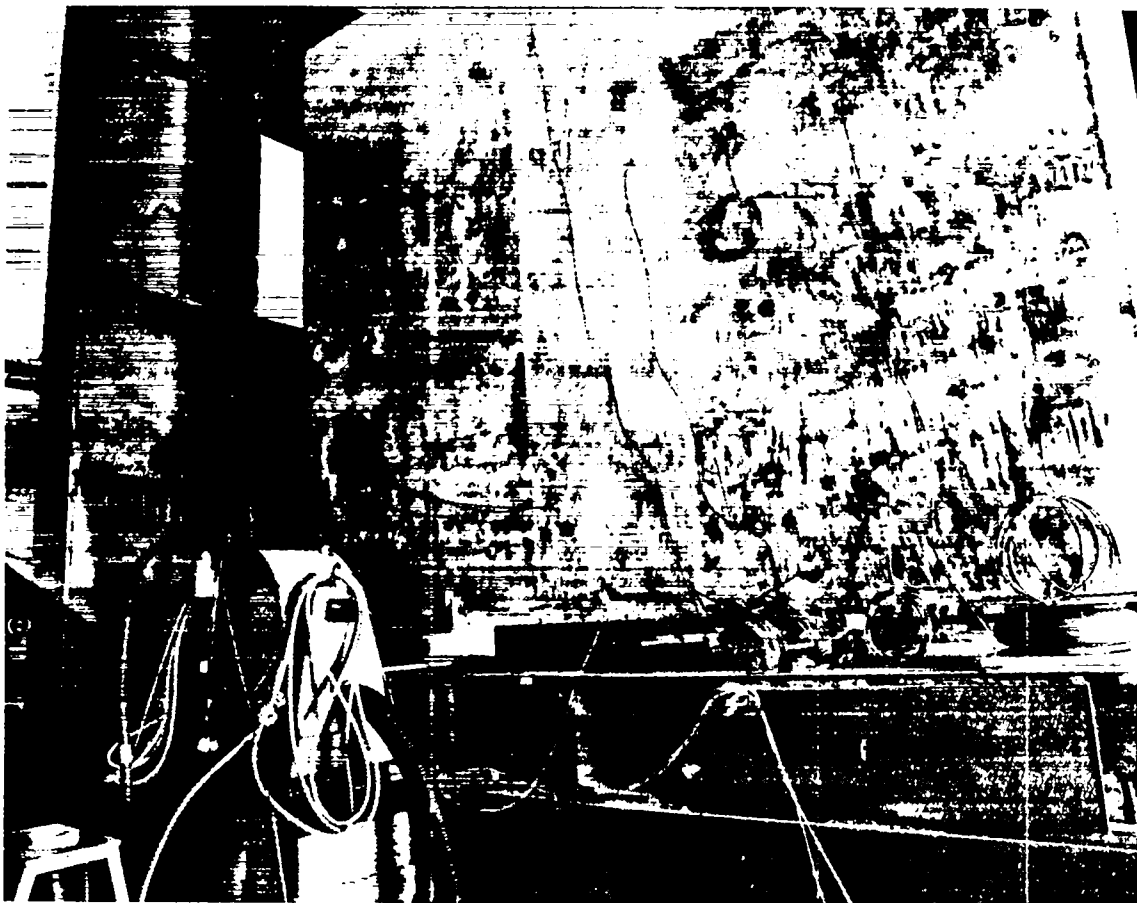


Fig. 8. Modal test excitation method.

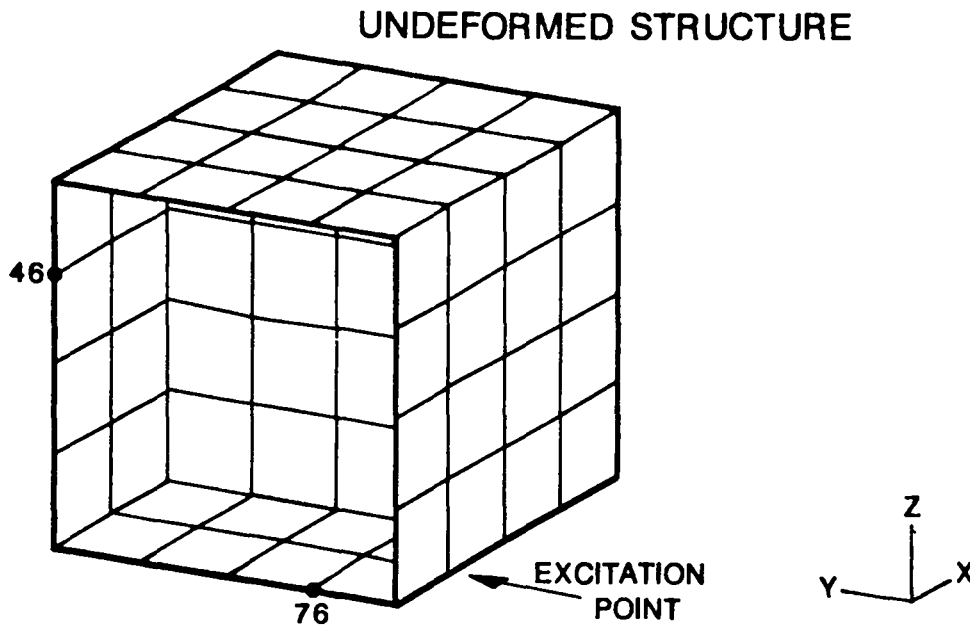


Fig. 9. Modal test measurement points.

shaker had only enough energy to excite the structure at its resonant frequencies. The frequency domain representation of the input and response was used to calculate a set of frequency response functions. Typical examples of the frequency response functions are shown in Figs. 10 and 11 and correspond to responses measured at Points 46 and 76 in the y and z direction, respectively. From these plots, resonant frequencies can be identified from zero crossings in the real portion that correspond to peaks in the imaginary portion. Eight resonant frequencies and corresponding mode shapes were experimentally identified between 0 and 200 Hz. The mode corresponding to the fundamental frequency is shown in Fig. 12.

A finite element analytical modal analysis was also run for comparison with the experimental modal analysis. Half the structure was modeled with free-boundary conditions at the base, and appropriate boundary conditions were applied along the plane of symmetry so that all modes below 200 Hz could be identified. The undeformed mesh and the first three modes corresponding to asymmetric boundary conditions are shown in Fig. 13a, and a direct comparison between an experimental and FEA mode is shown in Fig. 13b. Actual measured material properties were used in these calculations (modulus of elasticity of concrete =  $3.23 \times 10^6$  psi). A comparison of the corresponding analytical



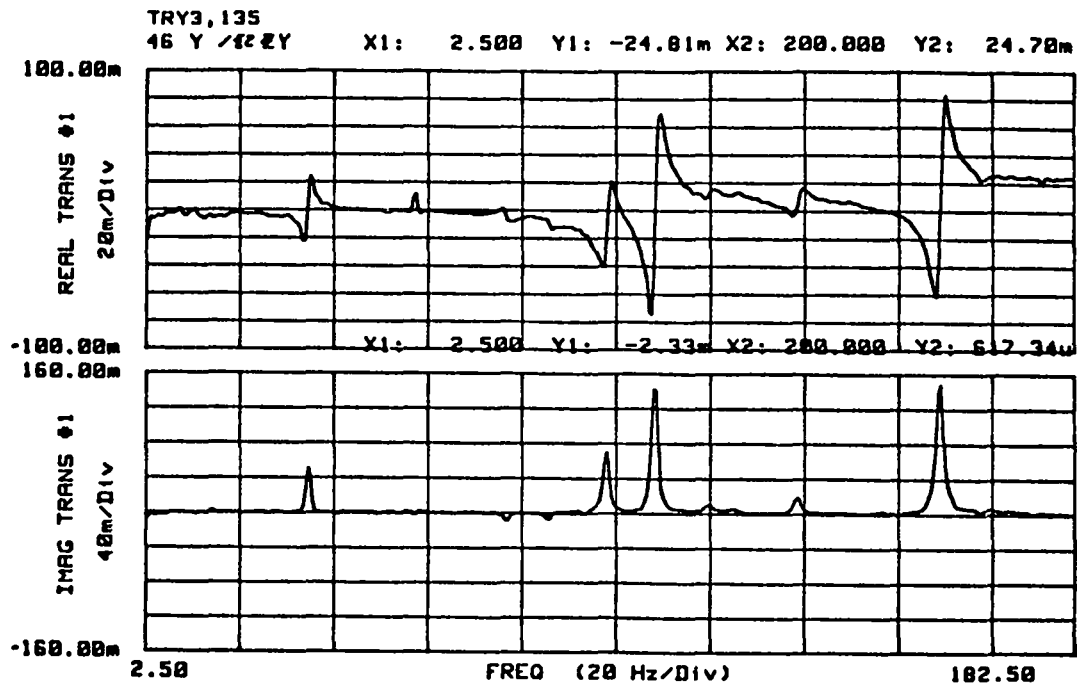


Fig. 10. Measured frequency response function Point 46-Y.

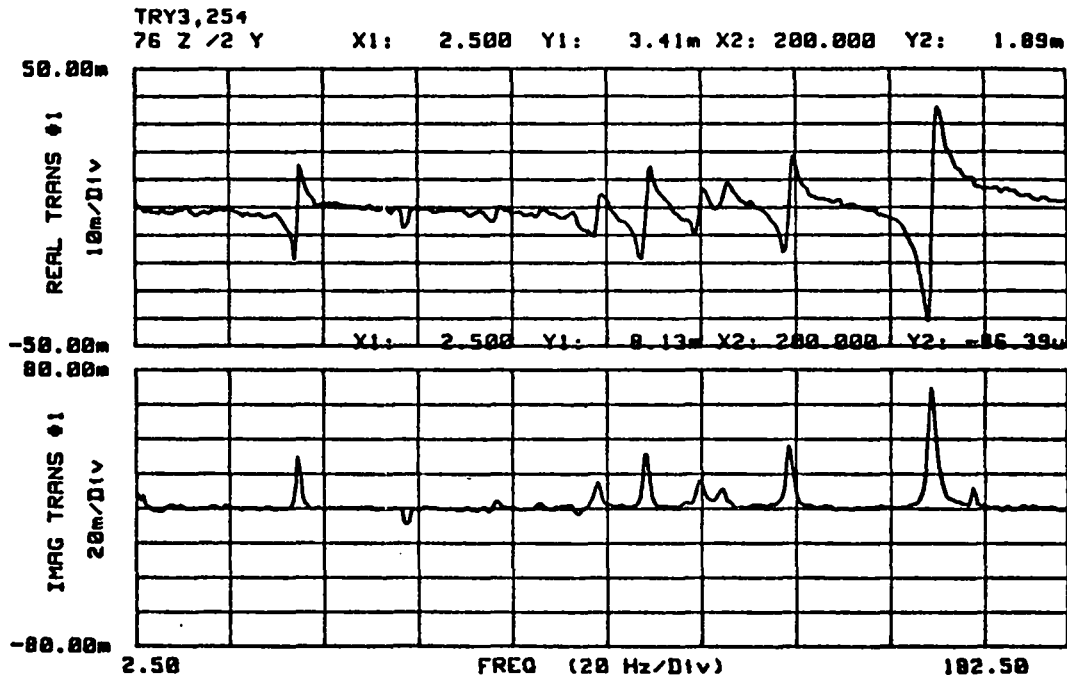


Fig. 11. Measured frequency response function Point 76-Z.

and experimental modes is presented in Table IV. The modes, which showed up in the FEA but did not show up in the experimental modal analysis, were not sufficiently excited by the amplitude and direction of the applied excitation.

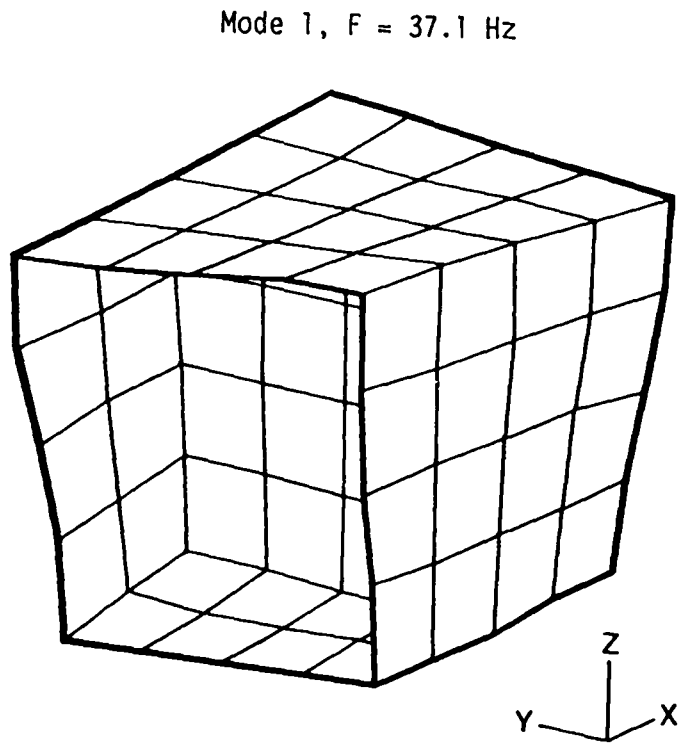
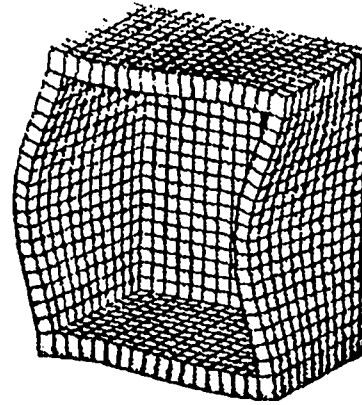
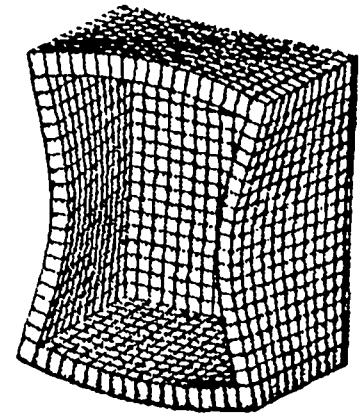


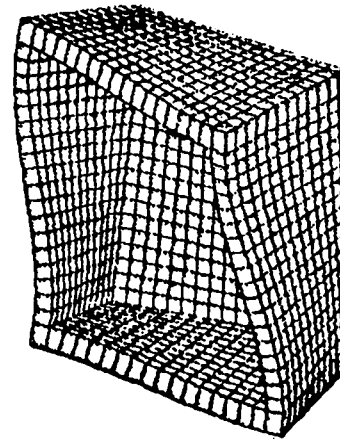
Fig. 12. Experimentally determined first mode.



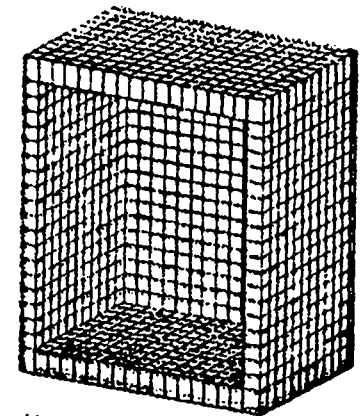
Mode 4,  $F = 102$  Hz



Mode 2,  $F = 77.8$  Hz



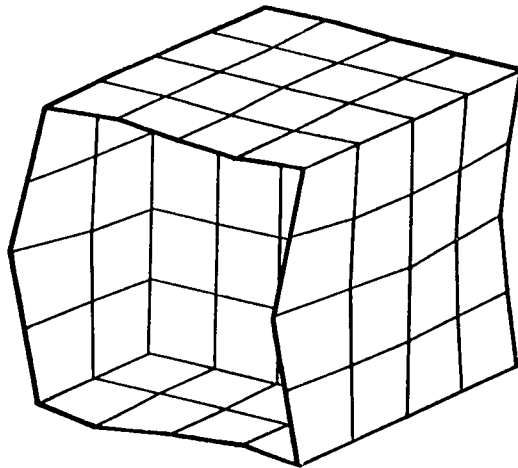
Mode 1,  $F = 36.3$  Hz



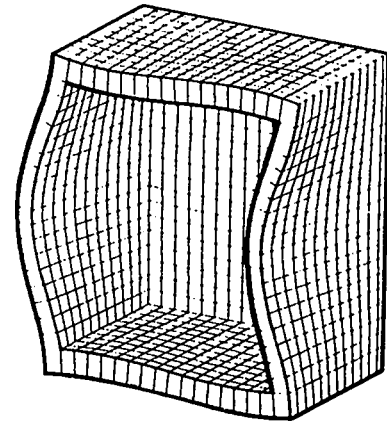
Undeformed

TRG Structure  
 6-in. wall, 0.25% rein.,  
 A.R. = 1  
 Free-free, asymm., B.C.'s

Fig. 13(a). Finite element mode shapes (only half the structure is displayed).



MODE 5, 111 Hz  
EXPERIMENTALLY DETERMINED



MODE 5, 111 Hz  
DETERMINED WITH ABAQUS  
F.E. PROGRAM

Fig. 13(b). Comparison of an experimentally measured mode shape and the corresponding mode determined by finite element analysis.

TABLE IV  
COMPARISON OF EXPERIMENTAL AND  
ANALYTICAL MODAL ANALYSIS RESULTS

Mode	Experimental	FEA with Measured Modulus	SOM with Measured Modulus
1	37.1	36.3	22.2 <sup>b</sup>
2	79.2	77.8	
3	88.3	86.0	
4	100	102	
5	111	111	134
6	122	120	
7	a	130	
8	141	136	
9	a	143	
10	172	154	
11	a	162	

<sup>a</sup> Not identified.

<sup>b</sup> The difference between this value and the FEA is attributed to the restraint of warping provided by the base and top slab. This restraint is not accounted for in the strength-of-materials analysis. Restraint of the warping would stiffen the structure torsionally and increase the natural frequency.

A larger shaker and/or change in the direction and location of excitation would have identified these modes. However, it was felt the objectives of the modal testing were accomplished with the one excitation location. Based on the fundamental frequency and noting that

$$\frac{f_{\text{measured}}}{f_{\text{calculated}}} = \frac{\sqrt{k_{\text{measured}}}}{\sqrt{k_{\text{calculated}}}}$$

where  $f$  is frequency in Hz, a comparison can be made between the low-load-level dynamic stiffness and the calculated stiffness from FEA. The measured stiffness as a percentage of theoretical is summarized for various moduli values in Table V.

TABLE V  
THE RATIO OF MEASURED STIFFNESS TO STIFFNESS  
CALCULATED BY FINITE ELEMENT ANALYSIS  
FOR VARIOUS VALUES OF  $E_c$

$K_m/K_t$	Measured $E_c$	$E_c = 57,000 \sqrt{f_c^r}$	$E_c = 33w^{3/2} \sqrt{f_c^r}$
	1.04	0.92	0.98

Finally, by adjusting the modulus in the finite element analysis so that the fundamental frequencies match the measured fundamental frequency, one can indirectly estimate the actual modulus of the concrete in the TRG-4 model. The value of  $E_c$  that made the FEA agree with the measured fundamental frequency was  $3.37 \times 10^6$  psi.

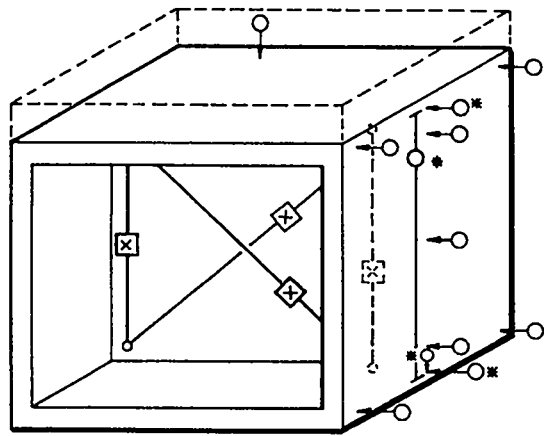
The results of the experimental modal analysis show excellent agreement with the analytical modal analyses and seem to verify Mr. Snell's conclusions about the initial state of the TRG-4 model and that the initial stiffness was very close to theoretical. When examining the results, it should be remembered that if nonlinearities caused by cracking or voids had existed, they would have produced excitation-amplitude-dependent response in the structure and that, at the load levels used in this test, the effects of these nonlinearities might not have appeared.

The lifting of the TRG-4 structure during the modal analysis was the only handling of the structure during the entire testing sequence and amounted to lifting the structure a few feet vertically and replacing it on the base.

## VI. STATIC TEST SETUP AND LOAD SEQUENCE

After the modal testing had been completed, the structure was bolted to the load frame base (Fig. 2). Two 2-in.-thick steel plates were placed on top of the base, grouted level, and thirty-six 1.25-in.-diameter steel bolts were placed through the plates and base in an attempt to obtain a truly fixed-base boundary condition. The bolts were torqued to 400 ft lb. Next, the two 6-in.-thick steel plates (Fig. 2) were placed on top of the model, grouted level, and held in place by thirty-six 1.25-in.-diameter steel bolts torqued to 400 ft lb. Because the load was to be applied by a force acting on the bottom 6-in.-thick steel plate, the connection of these steel plates to the concrete slab was designed to provide a friction connection and to produce a distributed load over the top of the structure. This type of loading is more indicative of that introduced by a seismic event.

The load frame was then assembled around the model, and an instrumentation frame was also assembled around the model independently of the load frame. Twenty-four Ono-Sokki EG-233 displacement transducers were placed on the model and on the instrumentation frame at the locations shown schematically in Fig. 14. Ten gages were mounted on the model itself, providing relative displacement readings that were independent of any rigid body rotation and translation. Of these ten, eight were located on the shear wall and were used to obtain the readings necessary to separate the shear and bending components of displacement. Overall structural deformations, including rigid body motion, were monitored with the remaining 14 gages attached to the load frame. These external gages were also used to measure torsional motion and sliding shear at the base of the structure. Before the actual test cycles, 0.375-in.-gage blocks were placed between the displacement gages on the exterior frame and the model to measure the deformation of the instrumentation frame caused by the return spring force of the gage. This deformation was found to be less than the resolution of the gages ( $4 \times 10^{-5}$  in.) and was considered to introduce insignificant error into the data acquisition.



- □ RELATIVE DISPLACEMENT
- ← ○ DISPLACEMENT, FIXED REFERENCE
- \* FOUR GAGES CORRESPONDING TO THOSE ON THE OTHER END
- x FOUR GAGES CORRESPONDING TO THOSE ON THE OTHER SIDE OF THE SHEAR WALL

Fig. 14. Displacement transducer location.

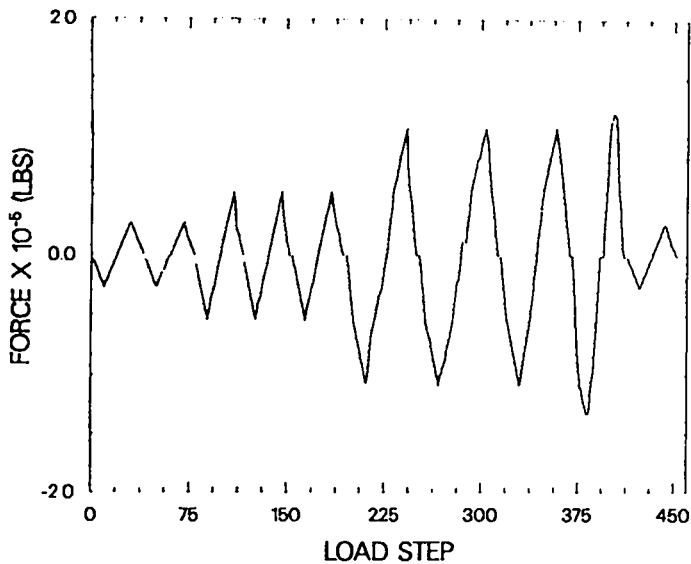


Fig. 15. Load history, force versus load step.

An ENERPAC hydraulic actuator was used to load the structure, and force input was monitored with a load cell located between the actuator and the steel plate. At specified load increments, the strain gages, displacement transducers, and load cell were scanned with an HP 3497A data scanner and were recorded on floppy disks by an HP 87 computer. After some initial low-level tests to check out the instrumentation, the load history shown in Figs. 15 and 16 was followed until the structure would no longer hold the applied load. Each integer on the horizontal axis in Figs. 15 and 16 represents a point at which the data were scanned. The complete load reversals shown in this load history were intended to represent the forces induced in a Seismic Category I structure during seismic excitation. The breaks in the load history at the end of a cycle were the result of zeroing the displacement gages and load cell before the start of the next cycle. This discontinuity was accounted for in the final data reduction by updating the total displacements and loading recorded on each record.

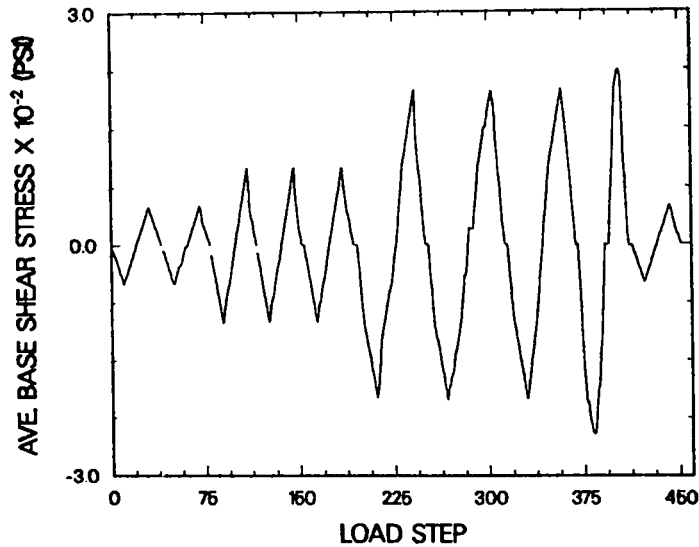


Fig. 16. Load history, average base shear stress versus load step.

#### VII. PRINCIPAL RESULTS AS REDUCED FROM THE INTERIOR GAGES AND COMPARED WITH SOM THEORY

The overall horizontal deformation versus load, as determined from the interior relative displacement gages, is shown in Figs. 17-27 for the entire load history and for each individual load cycle. This is the displacement at the top of these gages relative to the bottom of the gages. Because the displacement field over this region is nonhomogeneous, the displacements computed in this manner represent an average value for the wall. The method for computing the horizontal displacement is illustrated in Fig. 28, and, with the instrumentation used in this test, four values of horizontal displacement could be determined and averaged. Also, it is assumed that these displacement values do not significantly change when extrapolated to the exterior of the structure. This assumption was verified with a two-dimensional FEA of the shear wall (Appendix D). From this analysis, the horizontal displacement at the terminal point, Point C in Fig. 29, of the diagonal gage had a displacement of  $6.669 \times 10^{-3}$  in. when subjected to a 100-psi ABSS, while the exterior point, D, at the same elevation had a displacement of  $6.694 \times 10^{-3}$  in., a 0.4% difference. The data from the interior relative displacement gages is independent of rigid body rotation and translation and the assumptions necessary to remove those quantities.

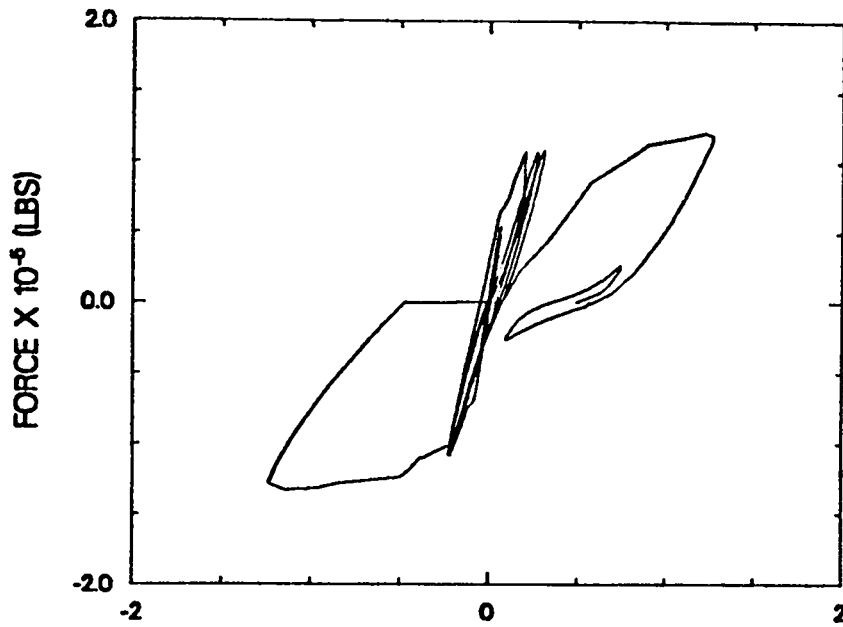


Fig. 17. Force versus displacement, based on the average of the internal gage readings.

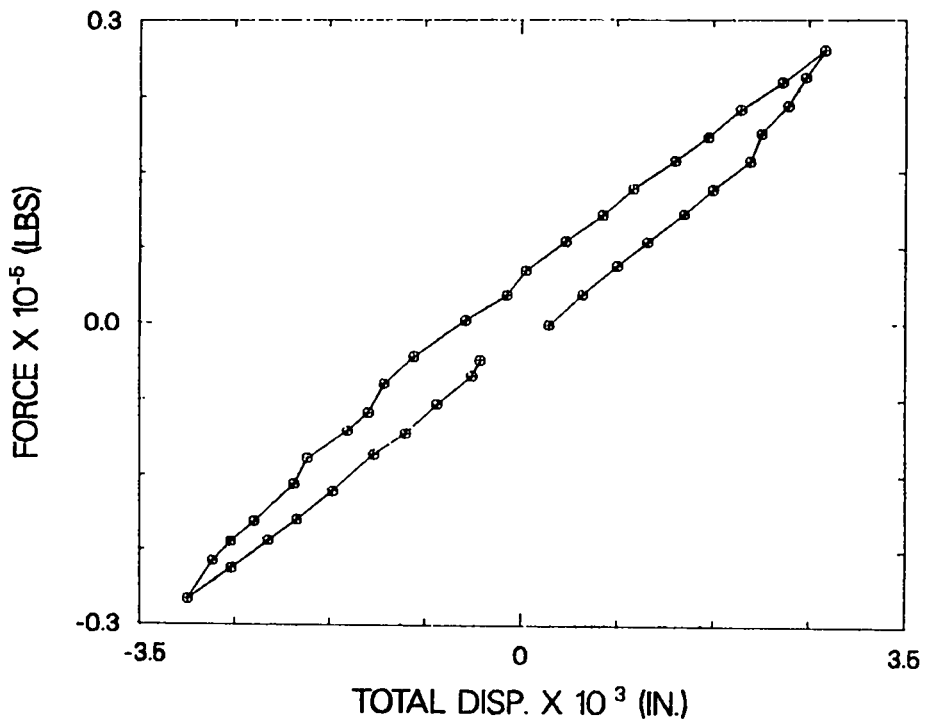


Fig. 18. Force versus displacement, first 50-psi ABSS cycle, showing the actual data points connected by straight lines.



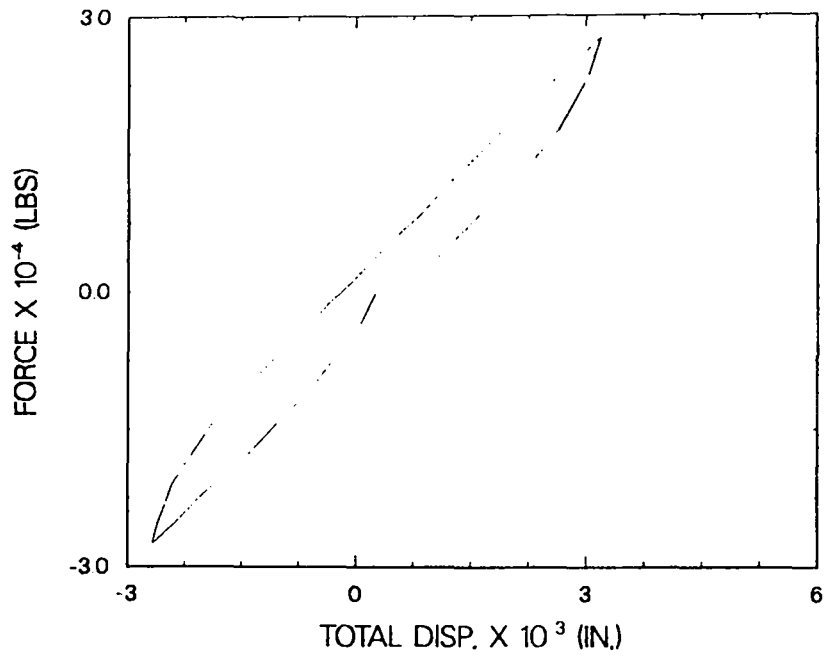


Fig. 19. Force versus displacement, second 50-psi ABSS cycle. The actual data points (not shown) were connected by straight lines to produce this and subsequent plots.

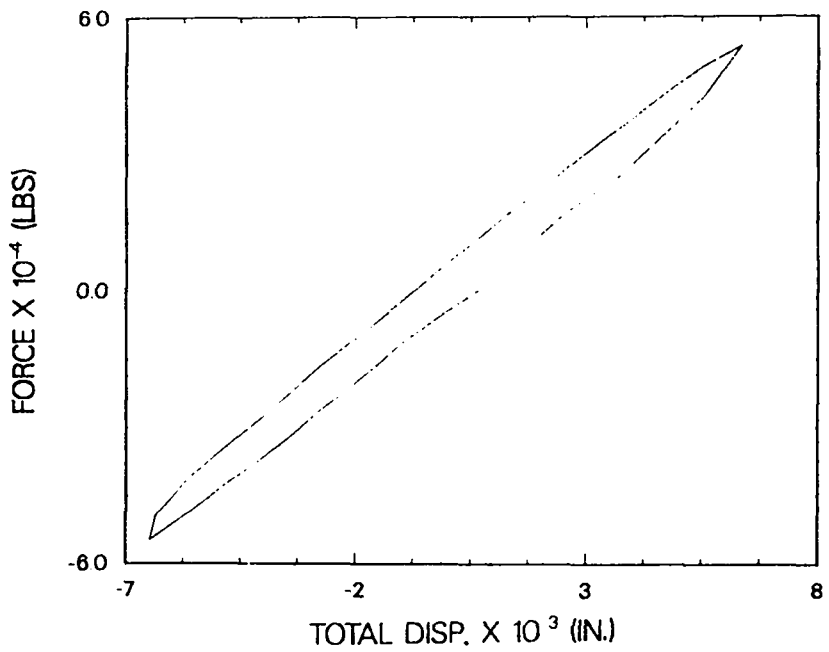


Fig 20. Force versus displacement, first 100-psi ABSS cycle.

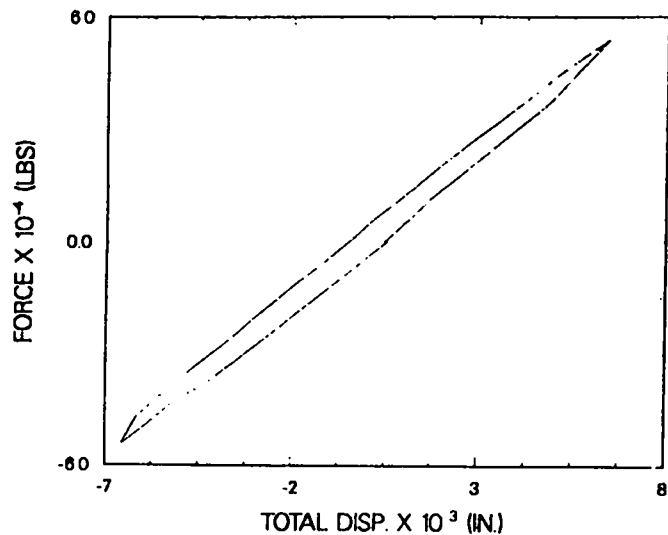


Fig. 21. Force versus displacement, second 100-psi ABSS cycle.

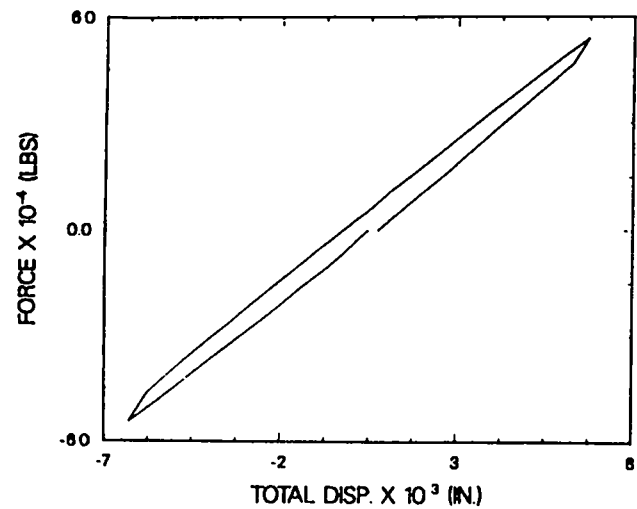


Fig. 22. Force versus displacement, third 100-psi ABSS cycle.

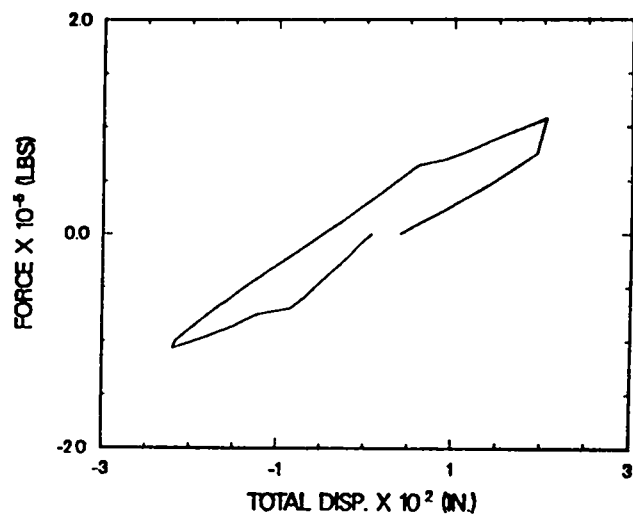


Fig. 23. Force versus displacement, first 200-psi ABSS cycle.

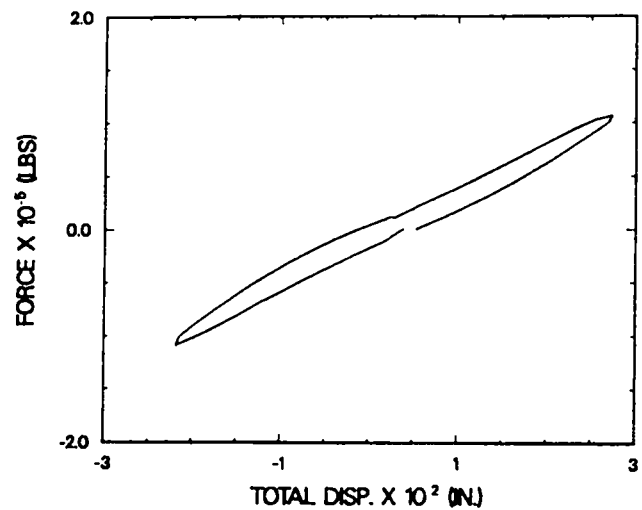


Fig. 24. Force versus displacement, second 200-psi ABSS cycle.

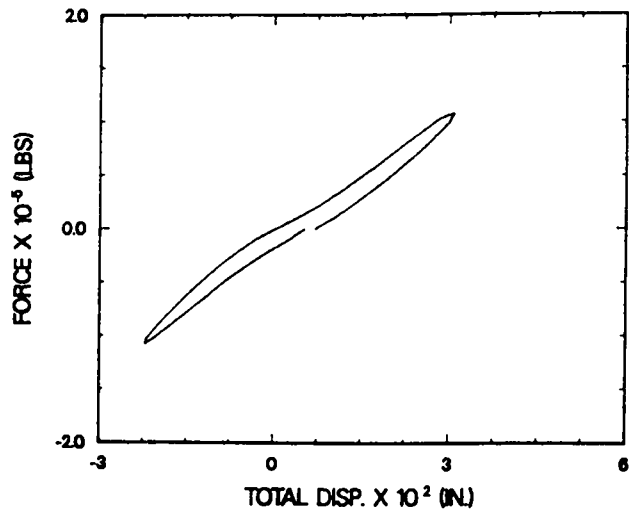


Fig. 25. Force versus displacement, third 200-psi ABSS cycle.

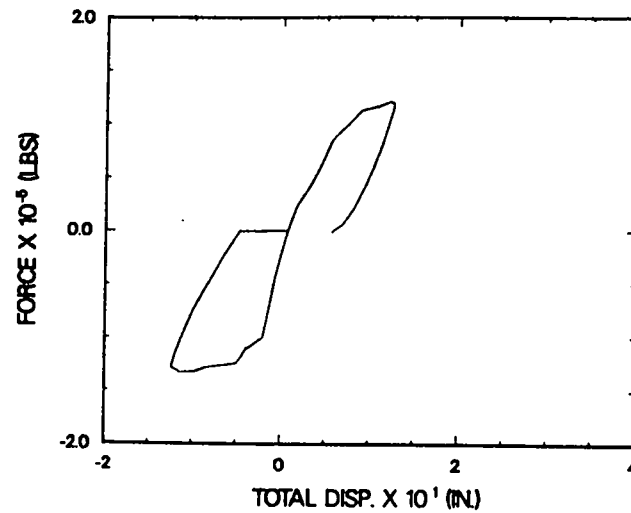


Fig. 26. Force versus displacement, failure cycle.

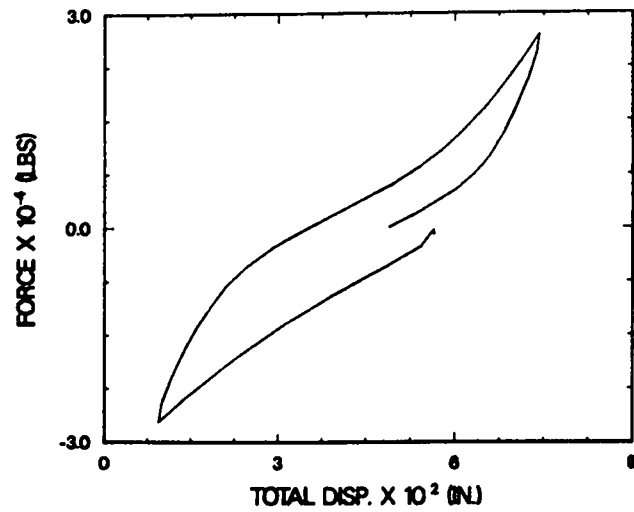
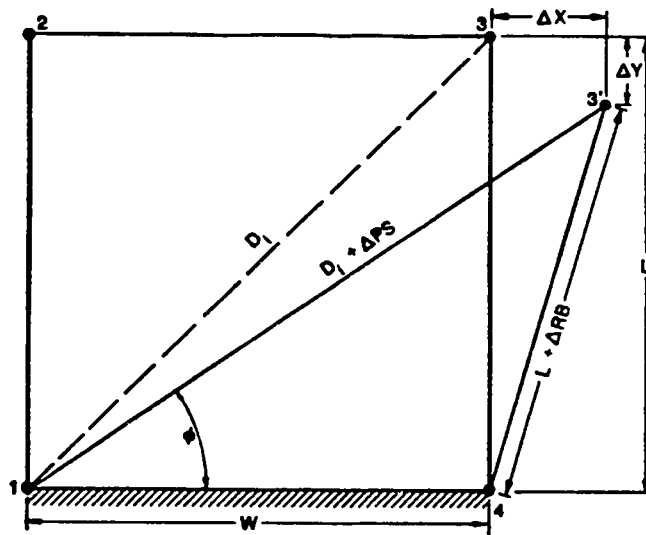


Fig. 27. Force versus displacement, final 50-psi ABSS cycle.



$$\Delta X = (D_1 + \Delta PS) \cos \phi - W$$

$$\Delta Y = (D_1 + \Delta PS) \sin \phi - L$$

$$\phi = \cos^{-1} \left[ \frac{W^2 + (D_1 + \Delta PS)^2 - (L + \Delta RB)^2}{2W(D_1 + \Delta PS)} \right]$$

**ΔPS - DIAGONAL DISPLACEMENT GAGE READING**  
**ΔRB - VERTICAL DISPLACEMENT GAGE READING**

Fig. 28. Method for determining horizontal displacement from internal gage readings.

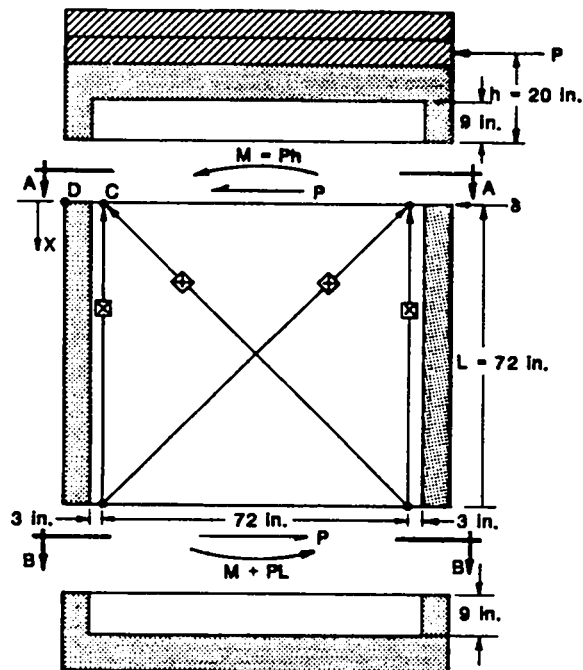


Fig. 29. Free-body diagram of the TRG-4 structure.

The structure exhibited linear response through all of the 50-psi and 100-psi ABSS load cycles and the measured stiffnesses during these precracking load cycles, based on the average displacements determined from the interior gage readings, were

$$K_T = 8.5 \times 10^6 \text{ lb/in.},$$

$$K_B = 52.6 \times 10^6 \text{ lb/in.}, \text{ and}$$

$$K_S = 10.2 \times 10^6 \text{ lb/in.}$$

The method for separating the horizontal displacement into shear and bending components is summarized in Appendix D. A comparison of data reduced from the external and internal instrumentation is given in Section VIII.

During the initial loading of the first 200-psi ABSS load cycle, the structure cracked at a load of 71,000 lb, and cracking was again observed at a load level of 65,000 lb during the reverse cycle. After completion of this load cycle, visual inspection revealed several diagonal cracks in the shear wall. The structure appeared to behave in a linear manner during the subsequent 200-psi load cycles; however, the stiffness was reduced by a factor of two from the uncracked value. In terms of percentage, the loss of stiffness occurred almost equally in the shear and bending components. The new values of stiffness were

$$K_T = 4.05 \times 10^6 \text{ lb/in.},$$

$$K_B = 23.0 \times 10^6 \text{ lb/in.}, \text{ and}$$

$$K_S = 4.91 \times 10^6 \text{ lb/in.}$$

The structure reached its ultimate strength during the initial loading of the first 300-psi load cycle. At the ultimate load of 140,000 lb, a large horizontal flexural crack opened completely through the tensile end wall and propagated at approximately  $45^\circ$  through the shear wall. Other shear cracks also opened, and previously existing cracks extended. During the reverse load cycle, the structure was able to sustain a load of 125,000 lb. Similar cracking occurred during this reverse cycle, but these cracks were not as pronounced as they were in the initial portion of the cycle. The final crack patterns on both sides of the shear wall are shown in Figs. 30 and 31. The horizontal cracks visible in the end wall were the ones produced during the initial load increase of the failure cycle.

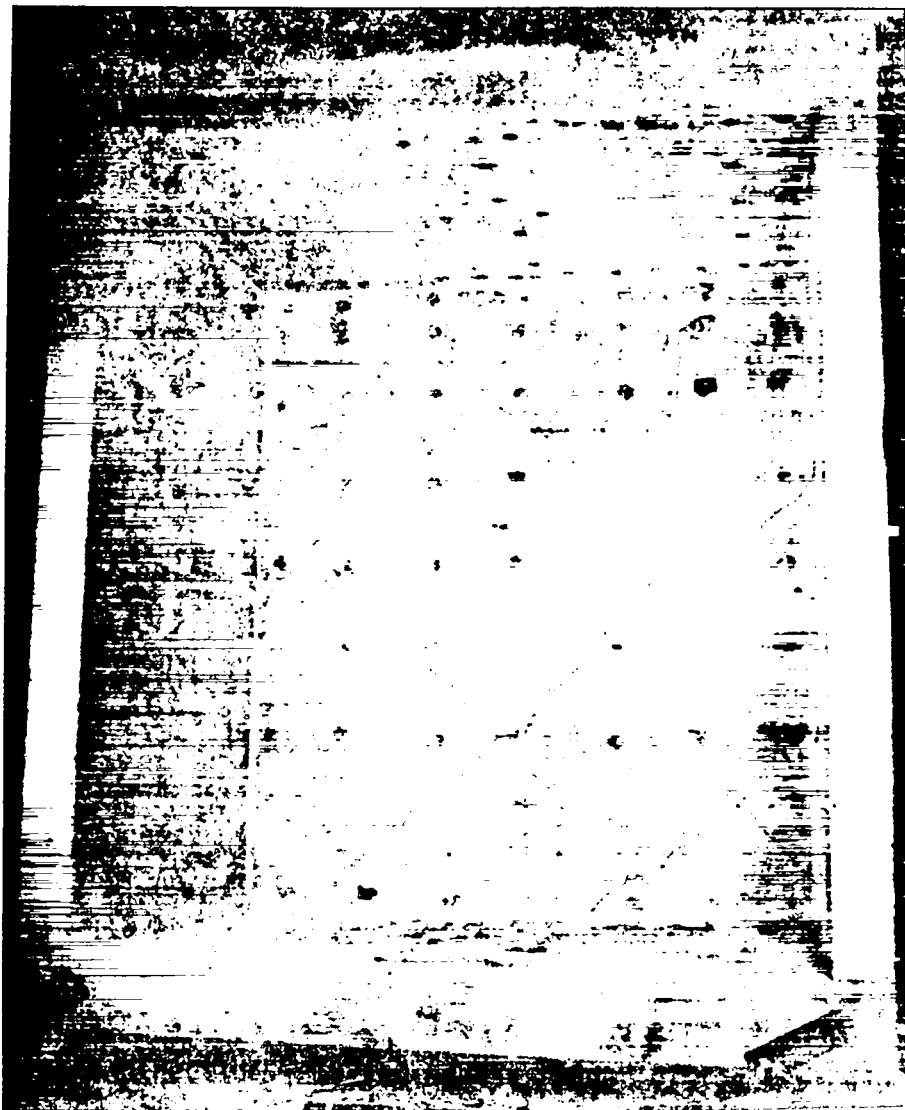


Fig. 30. Final crack pattern in the south side of the shear wall.

Initially, the response during the final 50-psi load cycle appeared linear with stiffness values of

$$K_T = 5.42 \times 10^5 \text{ lb/in.},$$

$$K_B = 48.4 \times 10^5 \text{ lb/in.}, \text{ and}$$

$$K_S = 6.11 \times 10^5 \text{ lb/in.}$$

However, during unloading after the initial force increase and during the load reversal, the displacements appeared nonlinear.



Fig. 31. Final crack pattern in the north side of the shear wall.

Theoretical stiffnesses that can be compared with stiffness values computed from the measured relative displacement readings were determined using Castigliano's theorem. By examining the free-body diagram in Fig. 29, the expression for internal strain energy stored in the structure between Sections A-A and B-B can be written as

$$U = \int_0^L \frac{(M + Px + wx)^2}{2EI} dx + \int_0^L \frac{(P + w)^2}{2 A_e G} dx \quad , \quad (1)$$

where

- U = internal strain energy,
- M = moment at Section A-A,
- P = shear force at Section A-A,
- w = imaginary unit load,
- E = concrete modulus of elasticity,
- I = cross-sectional moment of inertia, which includes entire end wall but neglects steel effects,
- G = shear modulus,
- A<sub>e</sub> = effective shear area, and
- L = length of the wall between Planes A-A and B-B.

Based on this expression for the internal strain energy and on standard energy principles described by Popov,<sup>19</sup> the horizontal displacement of the structure at Plane A-A relative to Plane B-B can be determined, and the stiffness of this portion of the structure can be expressed as

$$K_T = \frac{1}{\frac{hL^2}{2EI} + \frac{L^3}{3EI} + \frac{L}{A_e G}} .$$

This total stiffness may be decomposed into a bending component and a shear component yielding

$$K_B = \frac{6EI}{2L^3 + 3hL^2} ,$$

and

$$K_S = \frac{A_e G}{L} .$$



Table VI summarizes the various stiffness values that could be calculated for this test structure, depending upon how effective the end walls are assumed to be and also depending upon which value for modulus of elasticity is used.

The average peak strain gage readings on the rebar for the 50-, 100-, and 200-psi ABSS load cycles are plotted in Figs. 32-37. Also shown on these plots are the strains calculated from FEA and SOM. In the linear region, consistent results were obtained for both the end wall and the shear wall. These results compared very well with the calculated strain values (FEA and SOM). During the 200-psi ABSS cycle, cracking can be identified by the large jump in strain values, particularly at the north portion of the end wall.

Based on the results of the modal analysis and the initial precracking load cycles up to 100-psi ABSS, the initial stiffness of this structure is within 96-99% of the theoretical stiffness as determined from either a finite

TABLE VI  
THEORETICAL STIFFNESS VALUES

Effect of End Wall on the Moment of Inertia / Modulus of Elasticity	Average from Test Cylinder $3.23 \times 10^6$ psi	$57,000 \sqrt{f_c}$ $3.68 \times 10^6$ psi	$33w^{1.5} \sqrt{f_c}$ $3.43 \times 10^6$ psi	Ultrasonic $3.2 \times 10^6$ psi	Modal Analysis $3.45 \times 10^6$ psi
Full Section $2.78 \times 10^6$ in. <sup>4</sup>	$K_T = 8.42 \times 10^6$	$9.60 \times 10^4$	$8.95 \times 10^6$	$8.35 \times 10^6$	$9.00 \times 10^6$
	$K_B = 50.6 \times 10^6$	$58.1 \times 10^6$	$54.7 \times 10^6$	$50.6 \times 10^6$	$54.0 \times 10^6$
	$K_S = 10.1 \times 10^6$	$11.5 \times 10^6$	$10.7 \times 10^6$	$10.0 \times 10^6$	$10.8 \times 10^6$
ACI T Beam Criteria $7.46 \times 10^5$ in. <sup>4</sup>	$K_T = 5.81 \times 10^6$	$6.62 \times 10^6$	$6.17 \times 10^6$	$5.75 \times 10^6$	$6.20 \times 10^6$
	$K_B = 13.7 \times 10^6$	$15.6 \times 10^6$	$14.6 \times 10^6$	$13.5 \times 10^6$	$14.6 \times 10^6$
	$K_S = 10.1 \times 10^6$	$11.5 \times 10^6$	$10.7 \times 10^6$	$10.0 \times 10^6$	$10.8 \times 10^6$
Total Neglect of End Walls $3.645 \times 10^5$ in. <sup>4</sup>	$K_T = 4.02 \times 10^6$	$4.58 \times 10^6$	$4.27 \times 10^6$	$3.98 \times 10^6$	$4.29 \times 10^6$
	$K_B = 6.68 \times 10^6$	$7.61 \times 10^6$	$7.10 \times 10^6$	$6.61 \times 10^6$	$7.12 \times 10^6$
	$K_S = 10.1 \times 10^6$	$11.5 \times 10^6$	$10.7 \times 10^6$	$10.0 \times 10^6$	$10.8 \times 10^6$

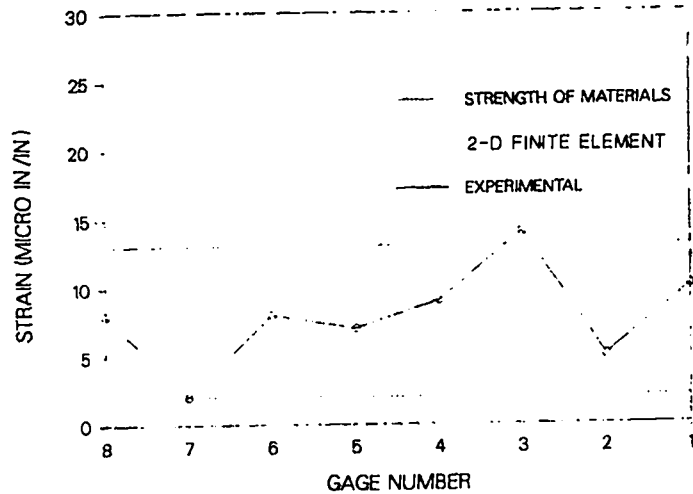


Fig. 32. The average maximum strain in the west end wall rebar during all 50-psi ABSS load cycles.

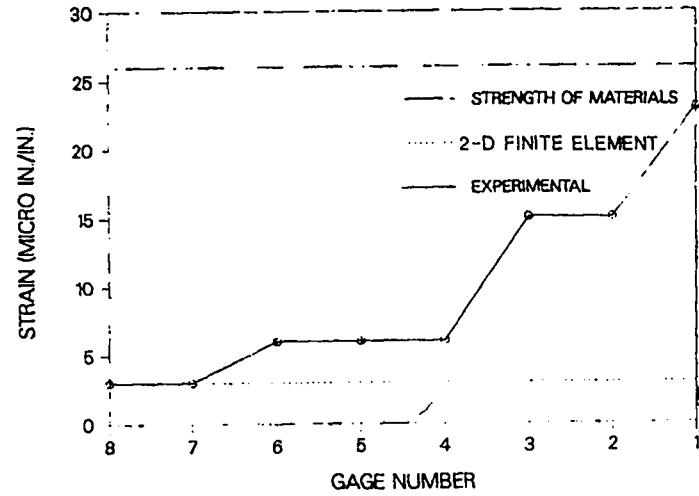


Fig. 33. The average maximum strain in the west end wall rebar during all 100-psi ABSS load cycles.

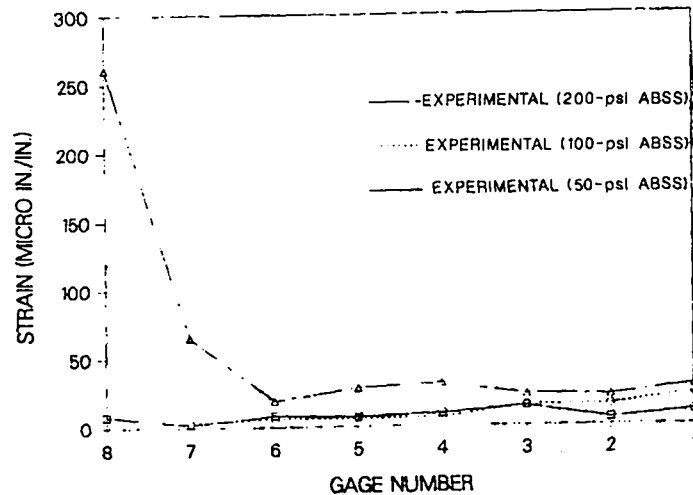


Fig. 34. The average maximum strain in the west end wall rebar during the 50-, 100- and 200-ABSS load cycles.

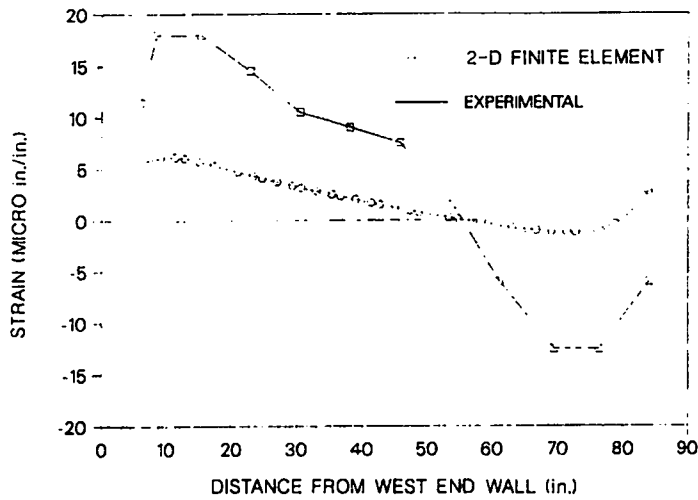


Fig. 35. The average maximum vertical strain in the shear wall rebar during the 50-psi ABSS load cycles.

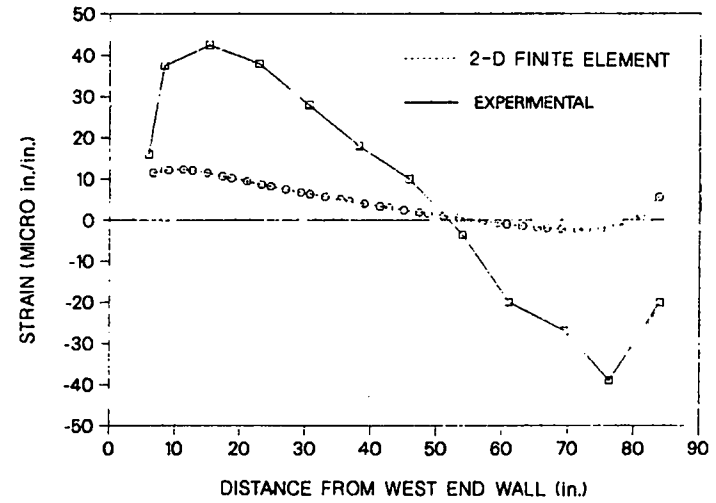


Fig. 36. The average maximum vertical strain in the shear wall rebar during the 100-psi ABSS load cycles.

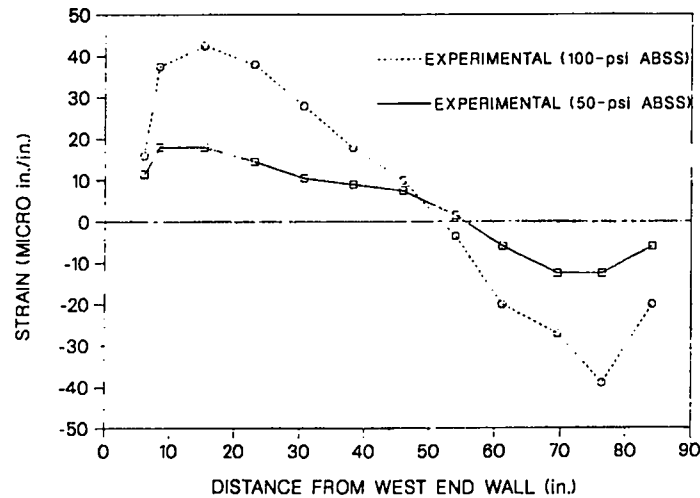


Fig. 37. The average maximum strain in the shear wall rebar during the 50-psi and 100-psi ABSS load cycles.

element analysis or a strength-of-materials approach. These results also show that, before cracking, the entire end wall contributes to the flexural stiffness of the shear wall. This width clearly exceeds the portion of the walls that would be considered effective based on ACI 349-85 T-beam criteria. This result implies that the usual assumption that plane sections remain plane during deformation is probably "helped" by the steel plates on top of the structure.

The first cracking load of 71,000 lb, which corresponds to an ABSS of 130 psi and which produces a maximum normal tensile stress of 171 psi, was considerably less than would have been predicted from a strength-of-materials analysis using either the split cylinder tensile strength (SCTS) or the modulus of rupture,  $7.5\sqrt{f_c}$ , per ACI 349-85. However, this cracking load agrees fairly well with the load that ACI 349-85 would predict for first cracking, 82,600 lb. This prediction assumes that cracking will occur when the PTS reaches  $4\sqrt{f_c}$ .

A possible source of discrepancies in the strength-of-materials analysis is that the end walls are only partially effective at the time of cracking. Agreement between predictions based on the PTS and the SCTS can be obtained at this load if this assumption is made; however, this assumption cannot be verified from the instrumentation readings obtained during the test.

This first cracking load would correspond to the load induced by a 1.6-g maximum horizontal acceleration earthquake with no amplification. The previous large-scale shear wall structure, TRG-3, which is similar to the structure reported herein but with 4.0-in. walls and which was dynamically tested and reported in Ref. 5, showed a reduction in stiffness of 4 during a 0.73-g peak horizontal acceleration earthquake. This seismic excitation corresponded to an equivalent static load of 32,900 lb., an ABSS of 91 psi, and a principal tensile stress of 92 psi, well below stress levels predicted to produce cracking. Obviously, there still remains a significant difference between the static and dynamic response of the similar structures tested at similar load levels. It is felt that at least one additional dynamic test will be required to clear up this discrepancy. Ideally, this test should be performed on a structure made of typical reinforced concrete (3/4-in. aggregate and No. 3 rebar). Also, the structure should be constructed at the test site to eliminate shipping damage as a possible source of reduced stiffness.

The ultimate load of this structure exceeds the design load specified by ACI 349-85 (126,000 lb). However, it should be pointed out that the reference on which the ACI design criteria is based, Cardenas et al.,<sup>20</sup> does not consider the effects of the boundary elements. The ABSS at failure, 260 psi, was slightly lower than had been observed in other static tests carried out in this program on microconcrete isolated shear walls (290-psi ABSS). This reduction was partly caused by the relatively higher tensile strength of microconcrete as compared with conventional concrete.

### VIII. ADDITIONAL RESULTS FROM EXTERIOR DISPLACEMENT GAGES

The results of data obtained during the static load test on the TRG-4 model presented thus far are based primarily upon the eight displacement gages that measure relative motion of an interior segment of the shear wall and on the strain gage data. A total of 24 displacements was measured during the test, as shown in Fig. 14, and these additional 16 displacement measurements permit additional results related to the deformation process of the model to be determined. The further data reduction has been done from these exterior gages, and the results are presented in this section.

#### A. Comparison of Deformations from Relative and Absolute Displacements

The locations of the displacement gages on the model were selected so that the deformations could be determined two different ways. The eight gages mounted on the interior of the shear wall measured relative displacements of the two ends of the gaged length, and these gages have been referred to as the interior or internal gages. The 16 gages mounted around the exterior of the model are referred to as the external gages. All except two of the external gages measured displacements with respect to a fixed reference (i.e., fixed for practical purposes). The two exceptions were the two gages on the exterior, which measured relative vertical displacements. In this section, certain deformation quantities are determined from both the internal and external gages and compared.

Figures 38 and 39 show the average base shear stress versus the horizontal or X-component of the total deformation for all of the load cycles,

based upon the internal gages and external gages, respectively. Figure 38 is the same as Fig. 17, except that it is shown in terms of shear stress, and is included here for ease of comparison. A study of these graphs shows that during the failure cycle the deformation shown by the external gages is substantially greater than that shown by the internal gages, indicative of crack

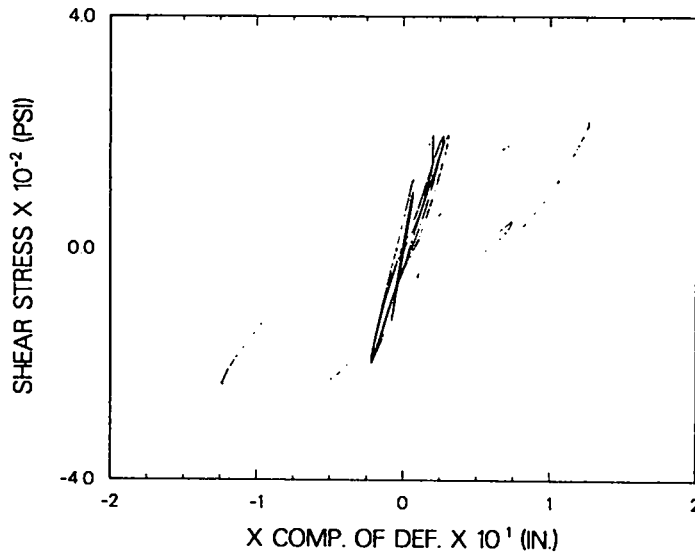


Fig. 38. X-component of total deformation for all load cycles based upon internal gages.

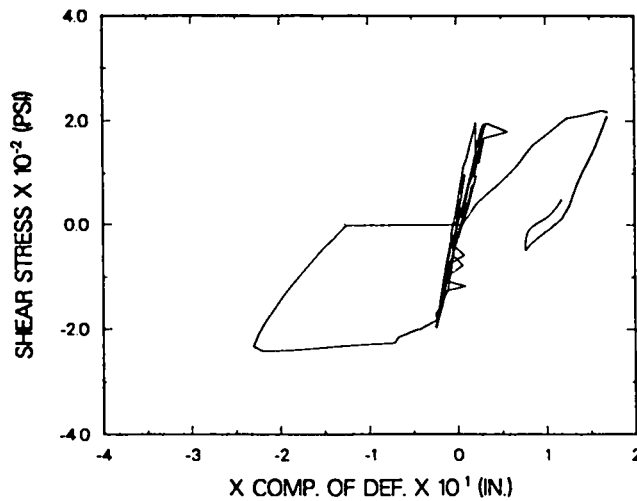


Fig. 39 X-component of total deformation for all load cycles based upon external gages.

formation in the wing wall area. Figure 39 also shows that there were several spurious data points during the 200-psi load cycle, but they did not cause problems in interpreting the results.

Figures 40 through 45 show the total deformation results for the 50-psi, 100-psi, and 200-psi load cycles individually, and Figs. 46 and 47 are for the failure cycle. Of note on these graphs are the following:

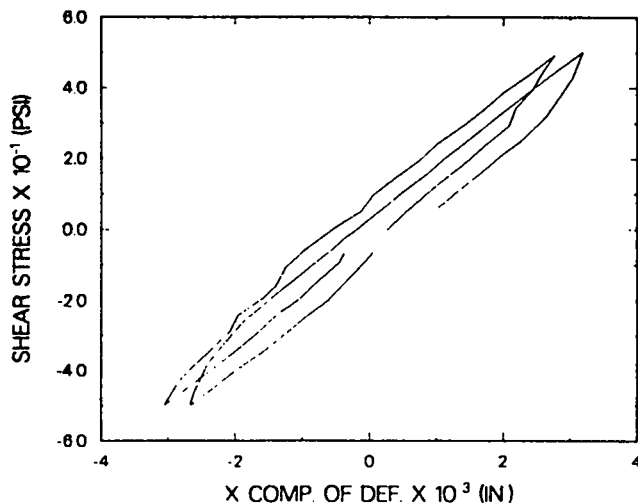


Fig. 40 X-component of total deformation for the 50-psi load cycles from internal gages.

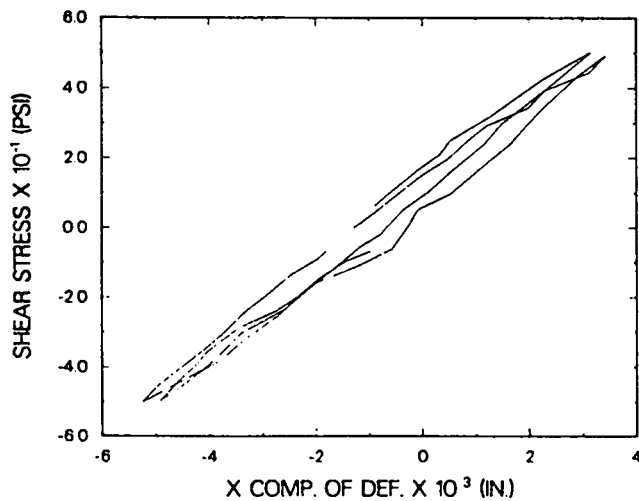


Fig. 41 X-component of total deformation for the 50-psi load cycles from external gages.

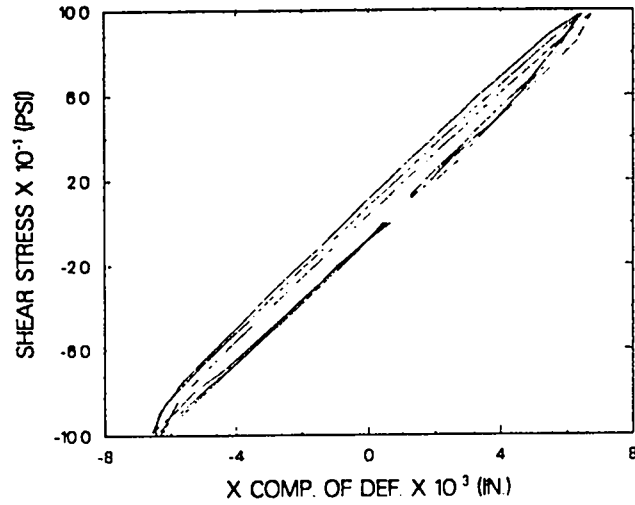


Fig. 42 X-component of total deformation for the 100-psi load cycles from internal gages.

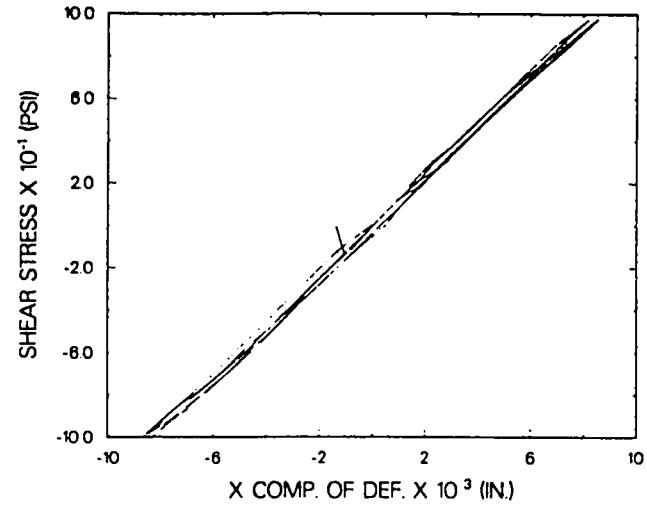


Fig. 43 X-component of total deformation for the 100-psi load cycles from external gages.

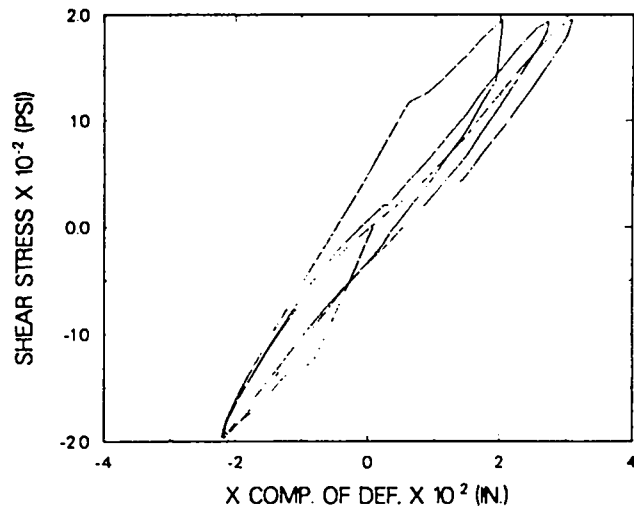


Fig. 44 X-component of total deformation for the 200-psi load cycles from internal gages.

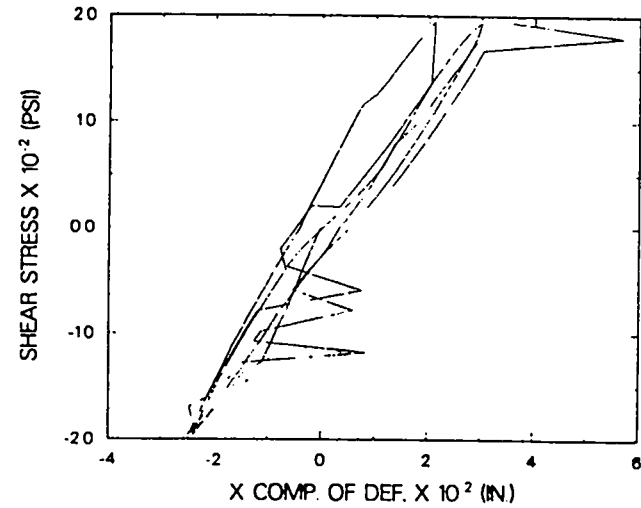


Fig. 45 X-component of total deformation for the 200-psi load cycles from external gages.



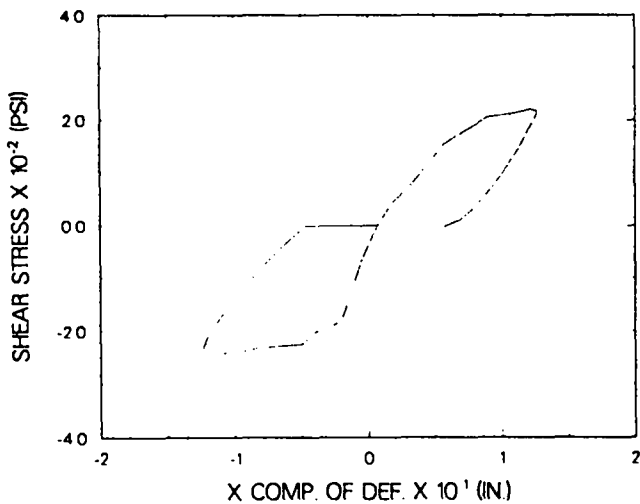


Fig. 46 X-component of total deformation for the failure load cycle from internal gages.

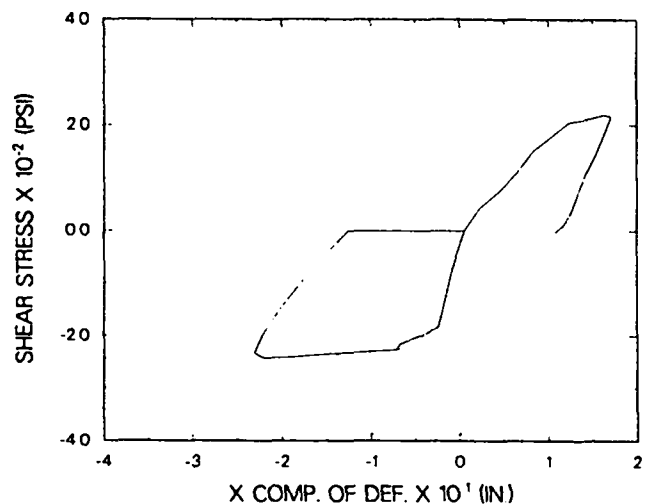


Fig. 47 X-component of total deformation for the failure load cycle from external gages.

1. the presence of hysteresis even at the lowest stress level;
  2. the formation of the first crack at approximately 120 psi during the first 200-psi load cycle for each direction of load; and
  3. the decrease in the slope after the formation of the first crack;
- both internal and external gages show this feature.

Figures 48 and 49 show the results for the first load cycle at each stress level.

Table VII is included for ease of comparison of numerical values for the internal and external gage results. In this table and subsequent similar tables, the peak-to-peak deformation has been given rather than zero-to-peak deformation to eliminate the effect of the apparent zero shifts. The last column has been included to make internal and external gage results comparable. The internal gages cover a shear wall height of 72 in., and the external gages cover a height of 98 in. The factor 98/72 was used as a multiplier for the internal gage values to determine the "adjusted" gage readings given in the last column. A comparison of the total deformation from the external gages and the adjusted internal gages shows that there is excellent agreement before the cracking of the shear wall. After cracking, the agreement is not as good, as might be expected because of the effect of the cracks.

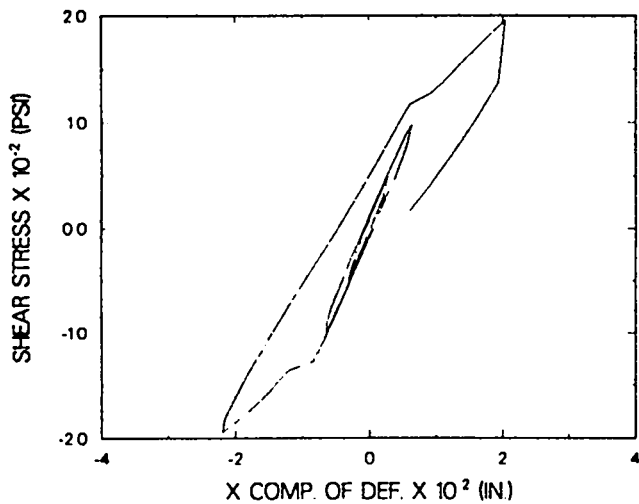


Fig. 48. X-component of total deformation for the first cycle at each load increment from internal gages.

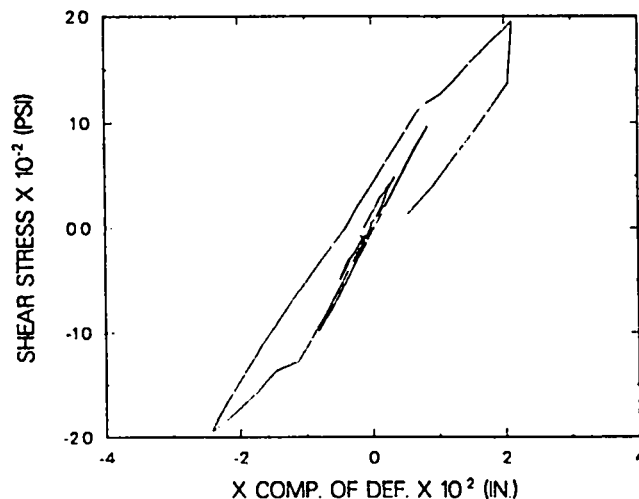


Fig. 49. X-component of total deformation for the first cycle at each load increment from external gages.

TABLE VII

PEAK-TO-PEAK TOTAL DEFORMATIONS

Stress Level	Total Deformation (in.)		
	Internal Gages	External Gages	Internal Gages* Adjusted
50 psi	0.0059	0.0083	0.0080
100 psi	0.0139	0.0188	0.0189
200 psi (1st cycle)	0.042	0.044	0.057
200 psi (3rd Cycle)	0.053	0.055	0.072
Failure	0.25	0.40	0.34

\* Linearly adjusted for the difference in shear wall height covered by gaging.

Figures 50-59 show the corresponding graphs from both internal and external gage for the shear deformation only. The characteristics observed in the total deformation results are also seen in the shear deformation results.

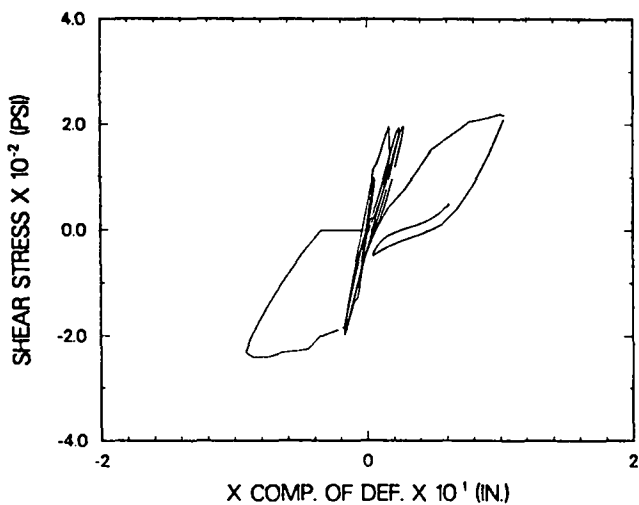


Fig. 50. X-component of shear deformation for all load cycles from internal gages.

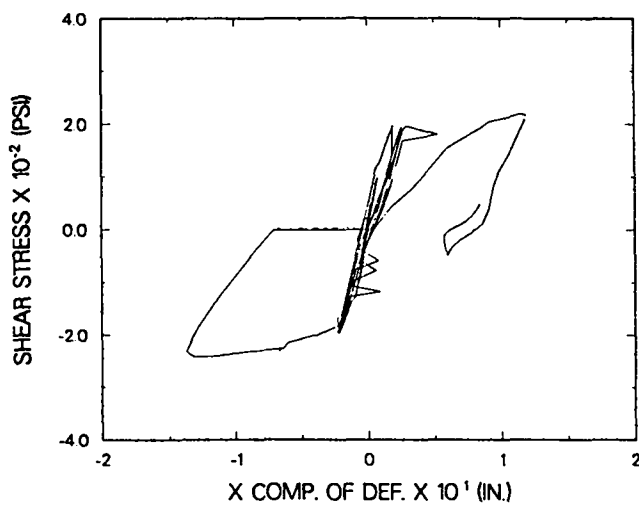


Fig. 51. X-component of shear deformation for all load cycles from external gages.

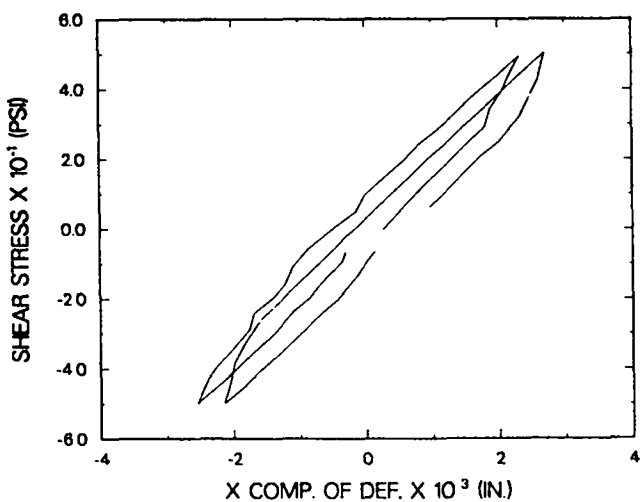


Fig. 52. X-component of shear deformation for the 50-psi load cycles from internal gages.

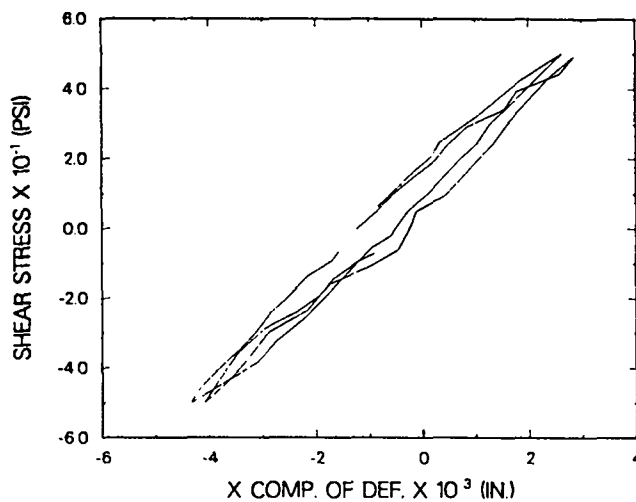


Fig. 53. X-component of shear deformation for the 50-psi load cycles from external gages.

Table VIII shows the corresponding numerical values. The agreement is again excellent for the load cycles before cracking.

The bending deformation for the first load cycle at each stress level is shown in Figs. 60 and 61, and Table IX shows numerical values from the graphs for comparison. There was still excellent agreement between the comparable internal and external values before the first crack appeared.

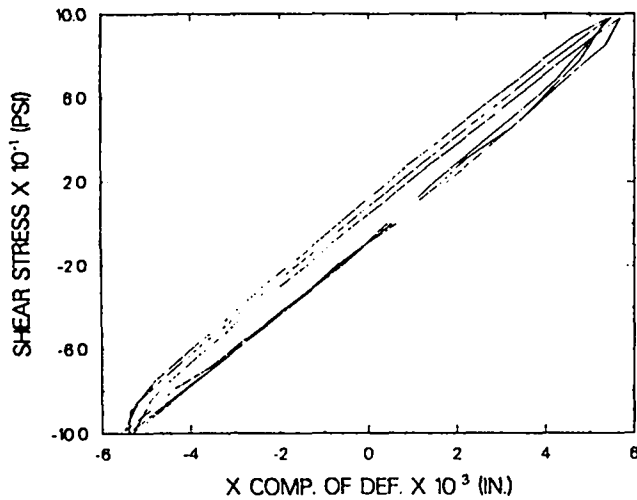


Fig. 54. X-component of shear deformation for the 100-psi load cycles from internal gages.

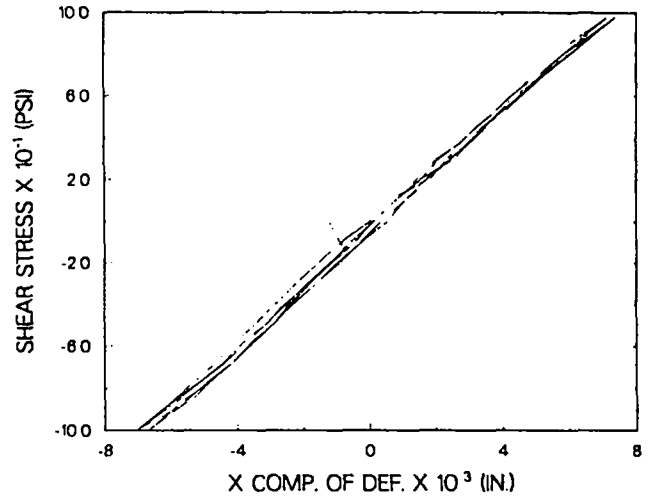


Fig. 55. X-component of shear deformation for the 100-psi load cycles from external gages.

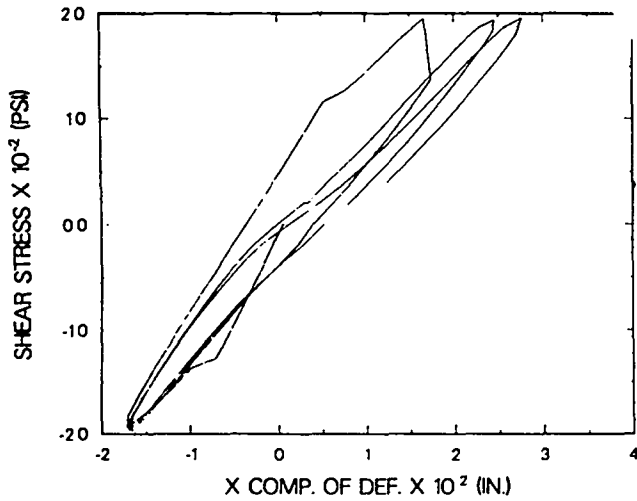


Fig. 56. X-component of shear deformation for the 200-psi load cycles from internal gages.

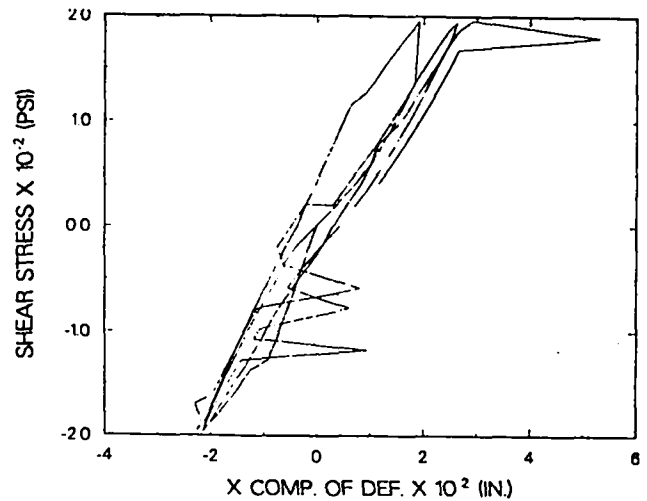


Fig. 57. X-component of shear deformation for the 200-psi load cycles from external gages.

In comparing the numerical values for the internal and external gage results, it is of interest to consider the data reduction process used to obtain the external gage results. The external gages measure displacements with respect to a fixed reference frame (i.e., the external frame supporting the gages), and the test item/loading frame assembly moves relative to the fixed frame. Therefore, it is necessary to correct the displacement gage

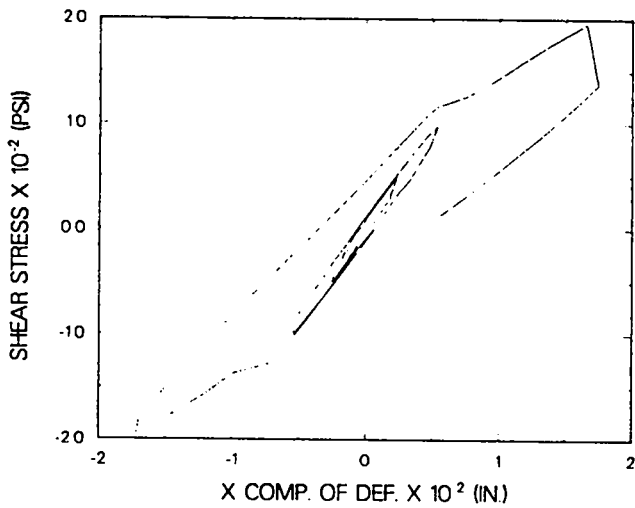


Fig. 58. X-component of shear deformation for the first cycle at each load increment from internal gages.

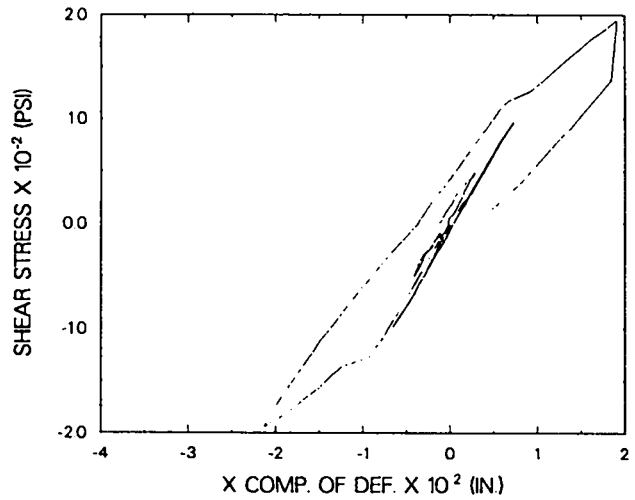


Fig. 59. X-component of shear deformation for the first cycle at each load increment from external gages.

TABLE VIII

PEAK-TO-PEAK SHEAR DEFORMATIONS

Stress Level	Shear Deformations (in.)		
	Internal Gages	External Gages	Internal Gages* Adjusted
50 psi	0.0049	0.0069	0.0066
100 psi	0.0109	0.0140	0.0149
200 psi (1st cycle)	0.034	0.041	0.046
200 psi (3rd cycle)	0.045	0.050	0.060

\* Linearly adjusted for the difference in shear wall height covered by gaging.

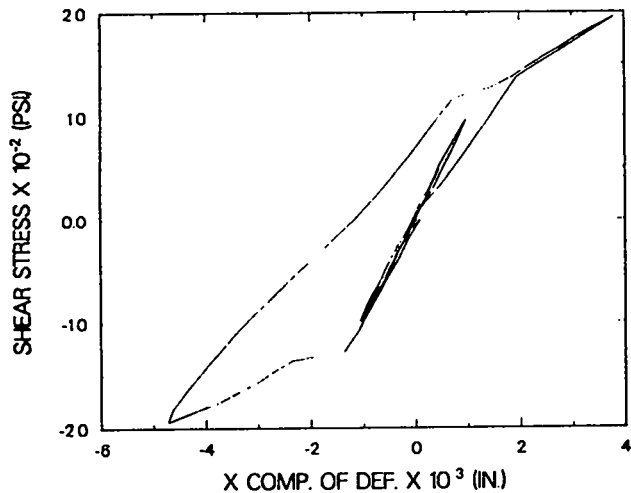


Fig. 60. X-component of bending deformation for the first cycle at each load increment from internal gages.

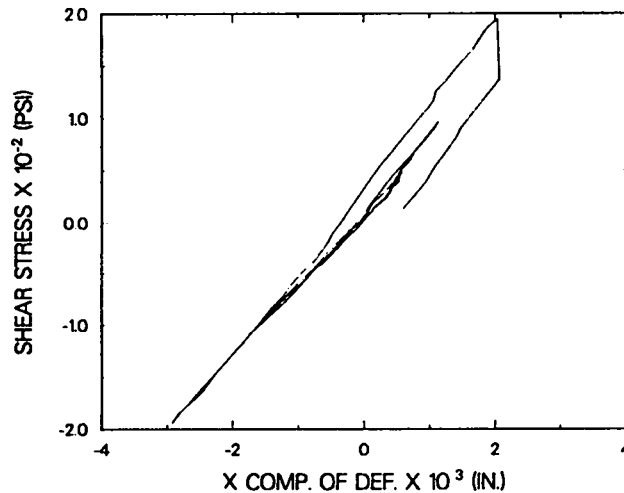


Fig. 61. X-component of bending deformation for the first cycle at each load increment from external gages.

TABLE IX

PEAK-TO-PEAK BENDING DEFORMATIONS

Stress Level	Bending Deformation (in.)		
	Internal Gages	External Gages	Internal Gages Adjusted
50 psi	0.0008	0.0013	0.0011
100 psi	0.0020	0.0028	0.0027
200 psi	0.0085	0.0049	0.0116

\* Linearly adjusted for the difference in shear wall height covered by gaging.

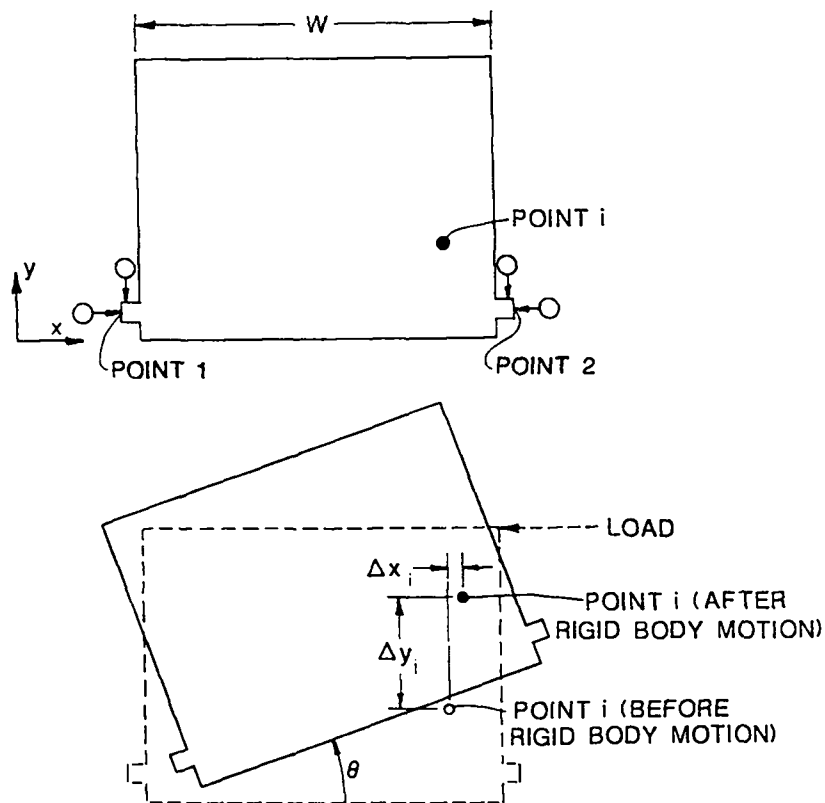
readings for the motion of the test assembly, referred to here as rigid body motion, in order to get the displacements caused by the deformation of the test item. Figure 62 shows the assumed rigid body motion of the test item and

defines the terms used in the equations given below. These equations were used for calculating the corrected displacement values.

$$\theta = \arctan \frac{R_{y2} - R_{y1}}{x_2 - x_1} ,$$

$$\Delta X_i = R_{x1} - x_i - x_1 (1 - \cos \theta) - y_i - y_1 \sin \theta .$$

$$\Delta Y_i = R_{y1} + x_i - x_1 \sin \theta - y_i - y_1 (1 - \cos \theta) .$$



$x_i, y_i$  = COORDINATES OF  $i^{\text{th}}$  POINT FROM FIXED REFERENCE, BEFORE MOTION

$R_{xi}, R_{yi}$  = READINGS OF THE  $x$  AND  $y$  GAGES FOR THE  $i^{\text{th}}$  POINT, AFTER MOTION

Fig. 62. Rigid body motion of model.

Here,  $\Delta X_i$  and  $\Delta Y_i$  are the rigid body motion of Point A caused by the change of angular position,  $\theta$ , and the motion of the reference Point 1. Now,

$$R_{x_i}(\text{correct}) = R_{x_i} - \Delta X_i \quad ,$$

$$R_{y_i}(\text{correct}) = R_{y_i} - \Delta Y_i \quad .$$

To demonstrate the effect of these calculations on the results, certain total deformation results were determined without the use of this data correction technique. Figures 63 and 64 show plots of these results, and they should be compared with Figs. 39 and 49. The maximum deformation when determined without the correction technique (Fig. 64) is about five times that with the correction. The fact that the deformation from the internal and external gages (as corrected for rigid body motion) agree within a few tenths of a mil (before fracture) is indicative of the validity of the data and results.

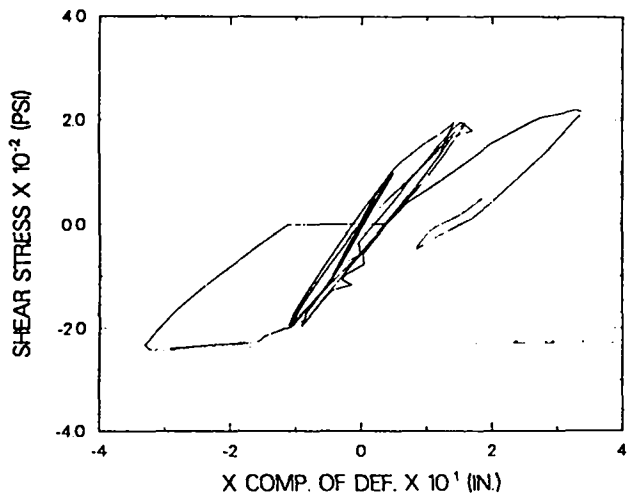


Fig. 63. Total deformation for all load cycles from uncorrected external gages.

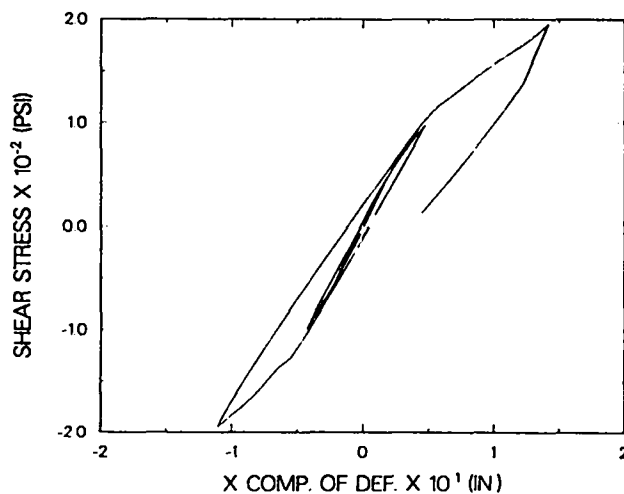


Fig. 64. Total deformation for the first cycle at each load increment from uncorrected external gages.

#### B. Ratios of Deformation Components

It is of interest to determine the ratio of shear deformation to total deformation for this test. This ratio was calculated using the results from both the internal and external gages. The deformation used in determining



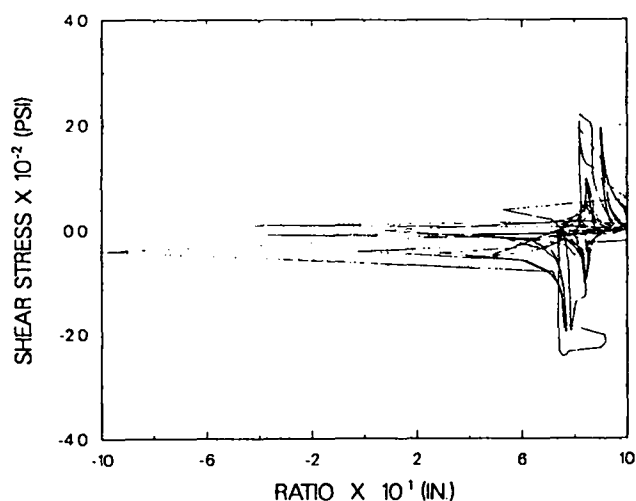


Fig. 65. Ratio of shear to total deformation from internal gages for all load cycles.

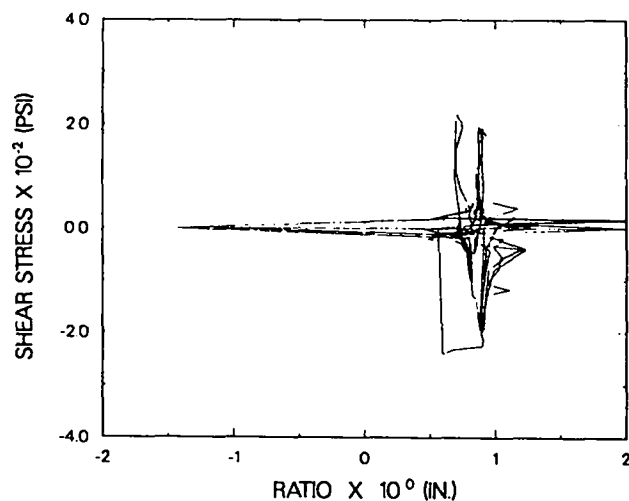


Fig. 66. Ratio of shear to total deformation from external gages for all load cycles.

these ratios was the X-component of the total deformation. The ratio was determined for each load increment, and the results were plotted versus the average base shear stress. Figures 65 and 66 are the plots for all of the load cycles. Near a stress level of zero, the ratio may become large, even greater than one. These values should be ignored because, as the load reverses, the total deformation, which is the denominator of the ratio, goes through zero. This singularity, coupled with the apparent zero shifts, causes the erratic behavior at low stress levels. The ratio values of significance in these graphs are the ones that converge at peak stress levels. Figures 67 and 68 are plots that show the first load cycle for each new maximum stress level. On these figures, the occurrence of the first crack during the 200-psi cycle can be easily identified as the point where the slope decreases sharply for increasing load magnitude. Figures 69 and 70 show the ratio variation during the failure load cycle.

Table X has been prepared for ease of comparison of numerical values from the plots. It may be concluded from this table that the ratio of shear to total deformation is 0.85 before initial cracking for a model having an aspect ratio of 1.0. It may also be concluded that after cracking first occurs the deformation ratio is still approximately 0.85, but there is more variation in the value. This variation is possibly caused by the types of crack patterns.

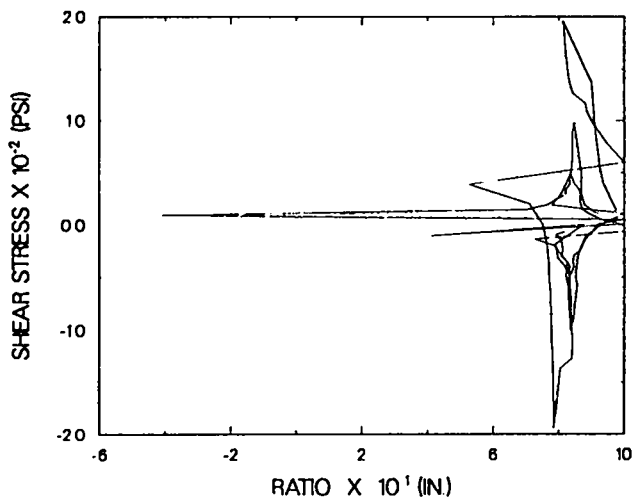


Fig. 67. Ratio of shear to total deformation for the first cycle at each load increment from internal gages.

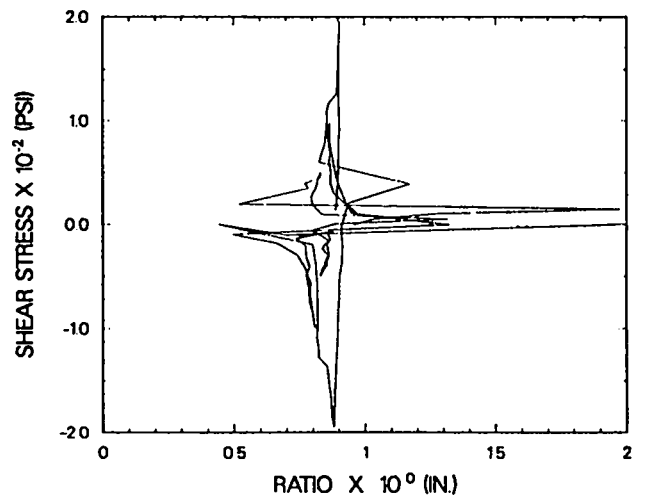


Fig. 68. Ratio of shear to total deformation for the first cycle at each load increment from external gages.

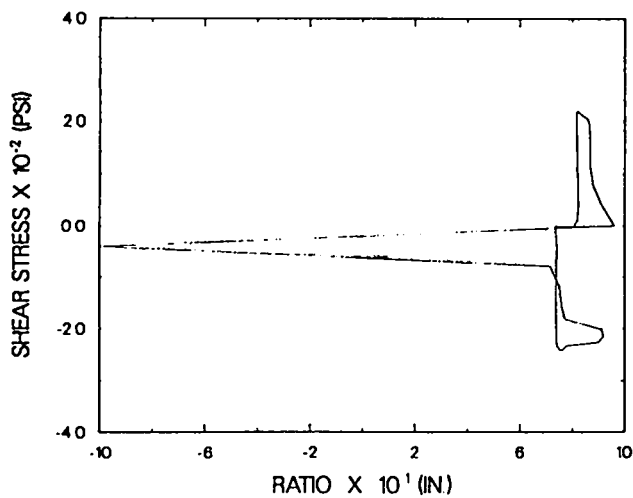


Fig. 69. Ratio of shear to total deformation for the failure load cycle from internal gages.

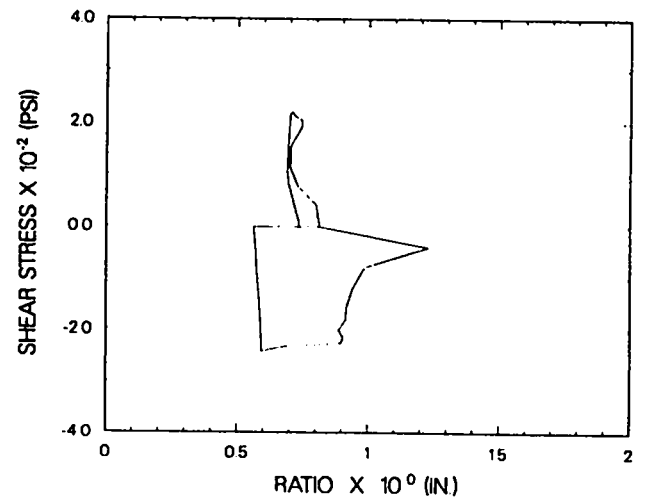


Fig. 70. Ratio of shear to total deformation for the failure load cycle from external gages.

TABLE X  
RATIO OF SHEAR TO TOTAL DEFORMATION

Stress Level	Ratio, Internal Gages	Ratio, External Gages
50 psi	0.84 (0.84)*	0.85 (0.85)*
100 psi	0.85 (0.85)	0.88 (0.82)
200 psi	0.82 (0.78)	0.90 (0.88)
Failure	0.78 (0.82)	0.70 (0.90)

\* The value in the parenthesis is the ratio for the negative load direction.

### C. Twisting Deformation

The point of application of the load on the model was selected so that under ideal conditions there would be no torsional deformation of the structure during testing, but achievement of the ideal condition could not be expected in the hardware. Outboard gages were placed within 1 in. of the outside edges at the top and bottom corners of the specimen to determine the amount of twisting of the model.

Data from these gages can be reduced and presented several ways to show how much twisting occurred during the test. Figures 71, 72, and 73 show the angle of twist at the "fixed" end or bottom of the model. Angular position is relatively linear with load for the 50-psi and 100-psi load cycles, but, once cracking occurs during the first 200-psi load cycle, the twist becomes highly nonlinear. Figures 74, 75, and 76 show the angular position at the top edge. The twist of the top edge at 200 psi is not as erratic as at the bottom edge, and the effect of the first crack at about 130 psi can be located in Fig. 76.

Another parameter that can be used to evaluate the degree of twisting is the torsional deformation of the model, i.e., the angular position of one end relative to the other. Figure 77 shows these results for the 200-psi load cycles and the failure cycle. Below 100 psi for the first load cycle, the function is essentially linear and of the order of  $10^{-5}$  radians ( $0.0006^\circ$ ).

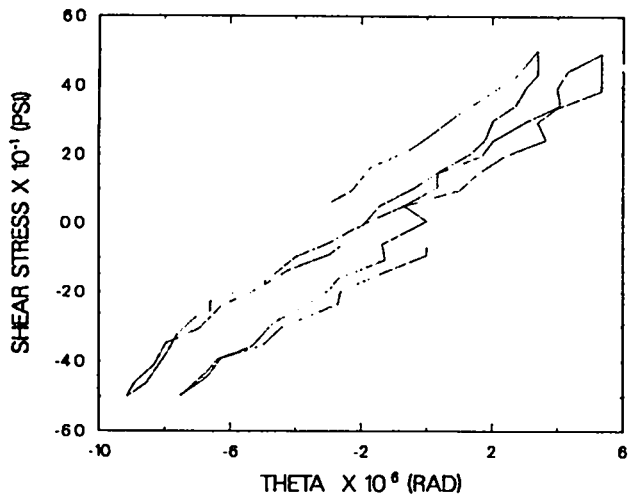


Fig. 71. Angle of twist of the bottom edge for the 50-psi load cycles.

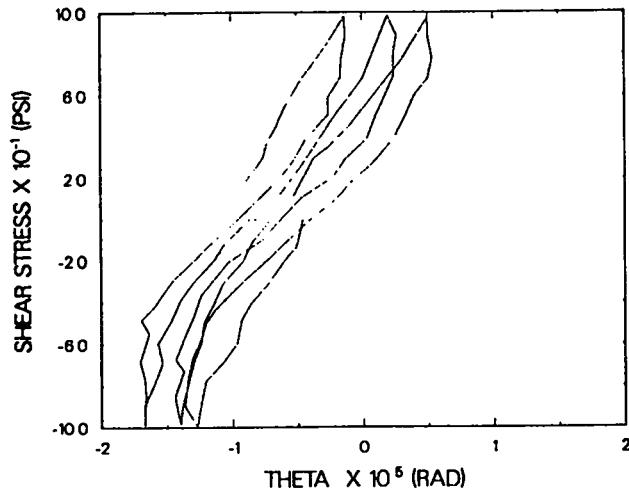


Fig. 72. Angle of twist of the bottom edge for the 100-psi load cycles.

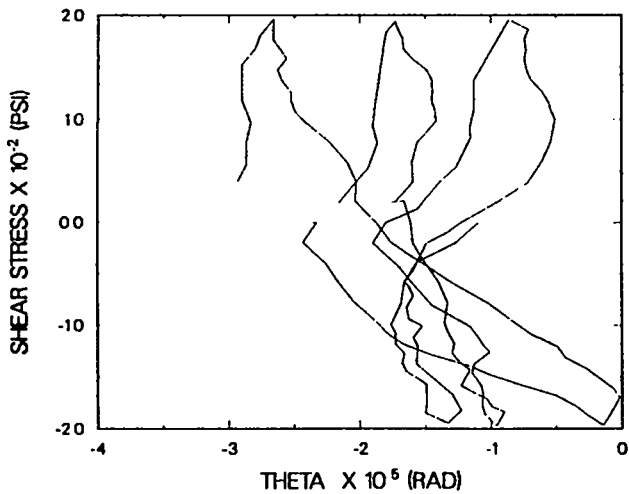


Fig. 73. Angle of twist of the bottom edge for the 200-psi load cycles.

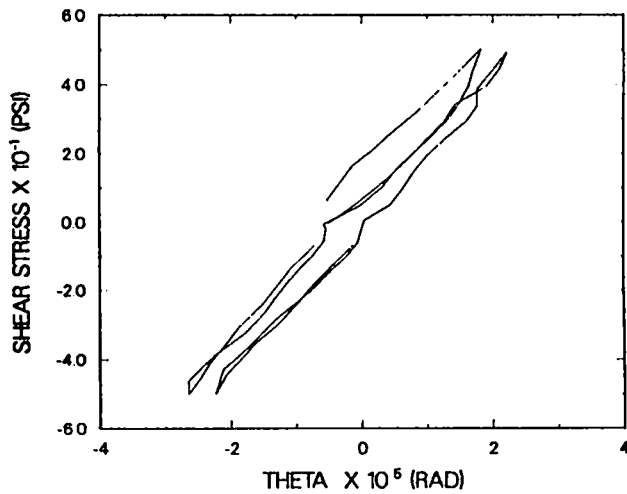


Fig. 74. Angle of twist of the top edge for the 50-psi load cycles.

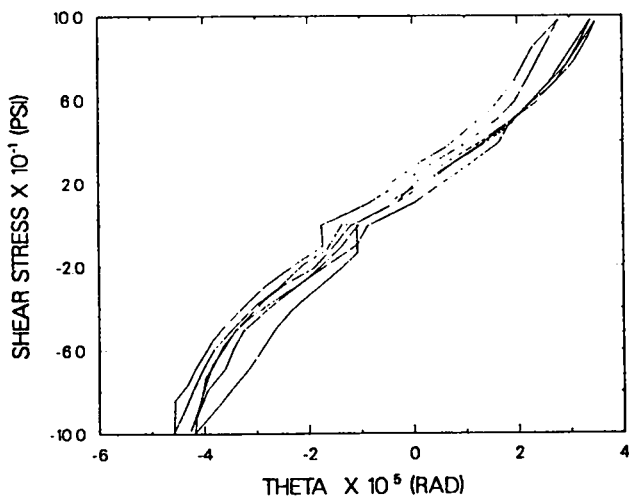


Fig. 75. Angle of twist of the top edge for the 100-psi load cycles.

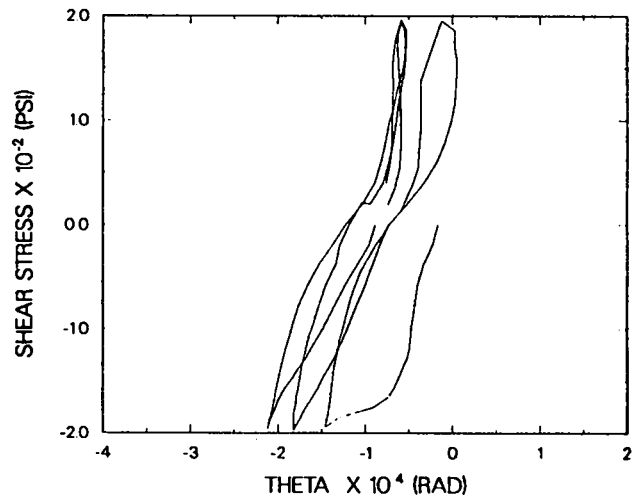


Fig. 76. Angle of twist of the top edge for the 200-psi load cycles.

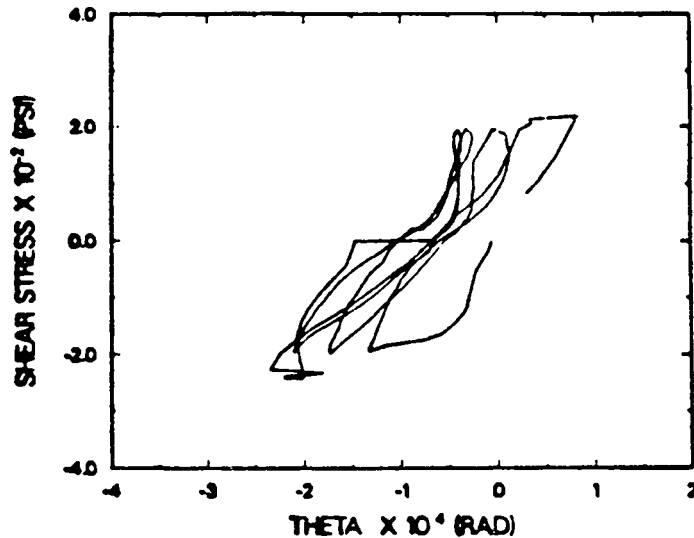


Fig. 77. Torsional deformation of the model for the 200-psi and failure load cycles.

The hysteresis occurring in the load cycles after cracking, including the failure cycle, results in substantially larger twisting deformation.

One last way of understanding the amount of twisting in the model is to look at a comparison of the readings of the outboard gages to the corresponding

center gage. This comparison has been made in the form of the ratio of the difference in the outboard gages divided by two to the center gage, and Figs. 78 and 79 show this ratio for the 100-psi load cycles for the bottom edge and top edge gages. In these graphs, the peak readings are the most meaningful because the hysteresis-type behavior of the model causes this ratio to be misleading for low loads. Consequently, the ratios of the low loads have been deleted from the graphs to show the ratio at peak readings. The ratios are in the range of 3 to 13%, as compared with an ideal value of zero.

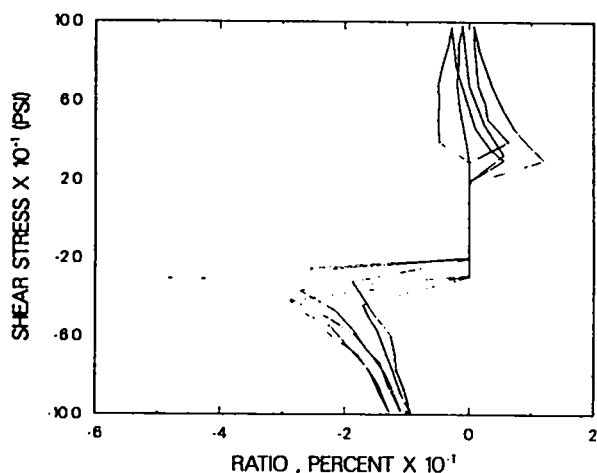


Fig. 78. Ratio of the twisting displacement to the center displacement, both at the bottom edge.

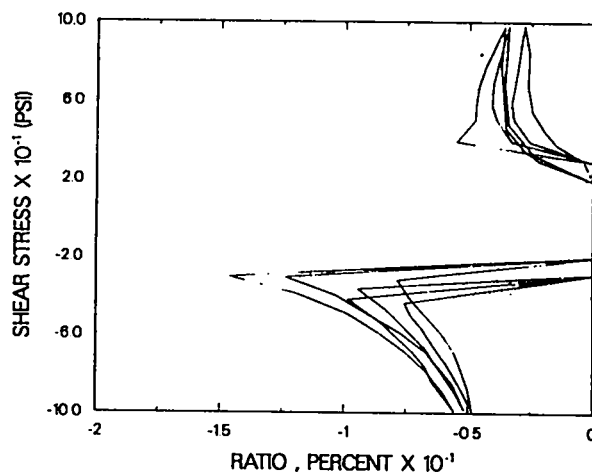


Fig. 79. Ratio of the twisting displacement to the center displacement, both at the top edge.

#### D. Motion of Shear Wall Relative to Floor and Ceiling

Two of the digital gages were located to show the motion of the floor and ceiling relative to the shear wall. Figure 14 shows all of the gage locations, and Figure 80 is included here to show only the gages used for the results presented here. Figures 81-84 show the difference in the readings of the two gages above and below the floor in these figures for the load cycles through the fracture cycle.

Because the gages are 8 in. apart, the shear deformation would cause the observed difference in readings before any cracking. The slopes for the 50-psi and 100-psi tests are essentially the same. For the first load cycle to 200 psi (Fig. 83), the same slope is seen to about 130 psi, at which point the slope decreases. This load corresponds to the appearance of the first cracks in

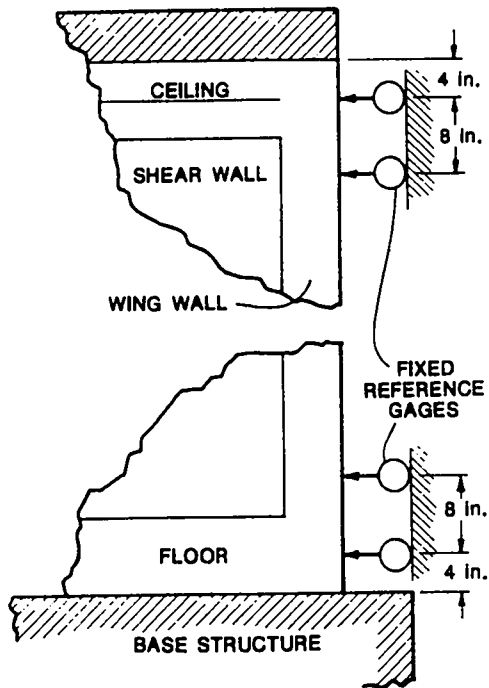


Fig. 80. Gage location for measurement of floor and ceiling motion relative to the shear wall.

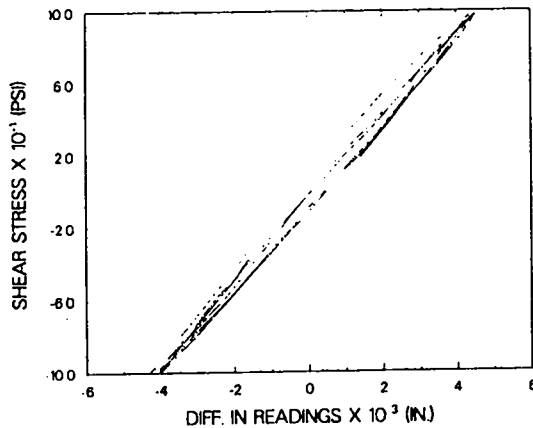


Fig. 81. Relative motion at the floor and shear wall interface for the 100-psi load cycle using uncorrected data.

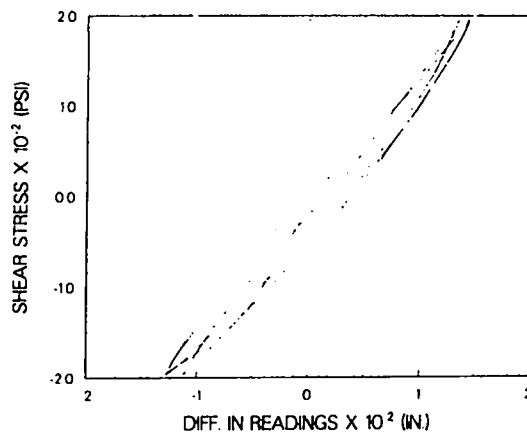


Fig. 83. Relative motion at the floor and shear wall interface for the 200-psi load cycle using uncorrected data.

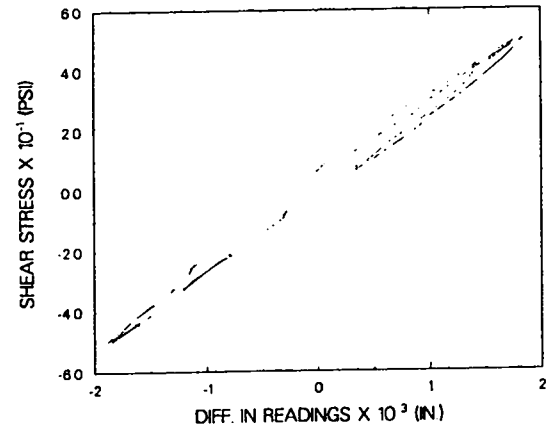


Fig. 82. Relative motion at the floor and shear wall interface for the 100-psi load cycle using uncorrected data.

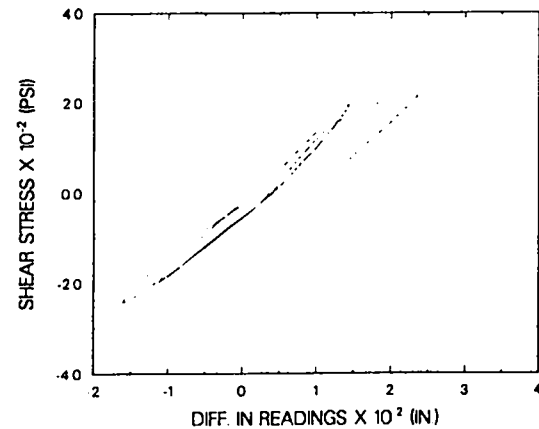


Fig. 84. Relative motion at the floor and shear wall interface for the last 200-psi load cycle and the failure cycle using uncorrected data.

the model. A corresponding change in slope appears in the first reverse load at about 120 psi, again in agreement with the cracking during that load cycle. Figure 84 shows the last 200-psi cycle and the fracture cycle. The first fracture cycle (negative load) did not cause additional cracking at the interface of the shear wall and floor, but the first positive load for this cycle produced additional relative motion below 200 psi.

Figures 81-84 show results from the gage reading, which were not corrected for the rigid body motion. The corresponding graphs for which the rigid body motion has been removed are shown in Figs. 85-88. In general, removing the rigid body motion reduced the magnitudes of the relative motion shown and

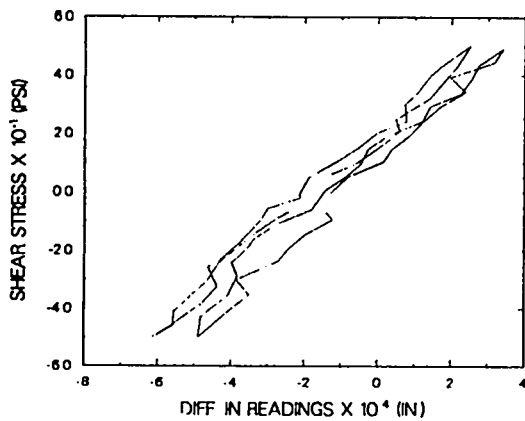


Fig. 85. Relative motion at the floor and shear wall interface for the 50-psi load cycle using corrected data.

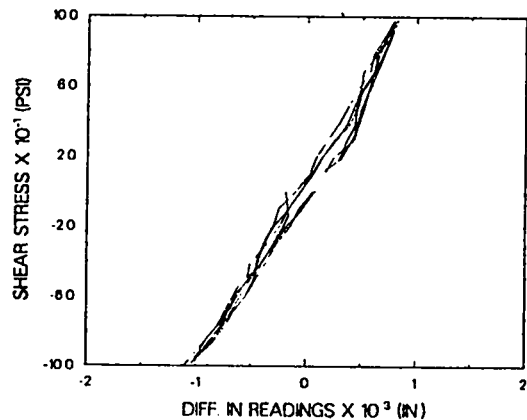


Fig. 86. Relative motion at the floor and shear wall interface for the 100-psi load cycle using corrected data.

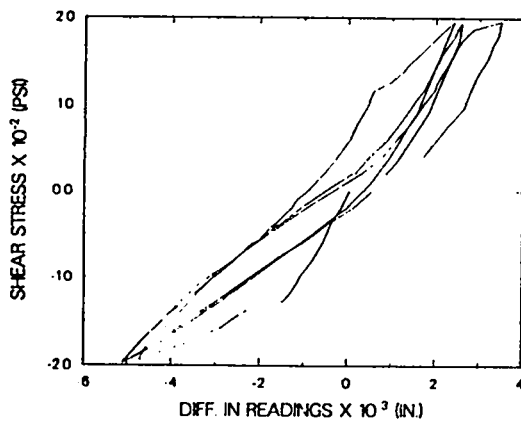


Fig. 87. Relative motion at the floor and shear wall interface for the 200-psi load cycle using corrected data.

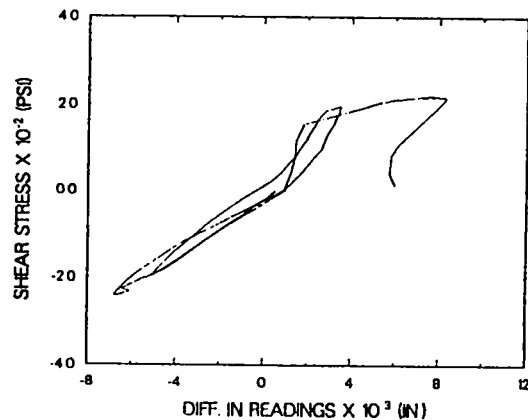


Fig. 88. Relative motion at the floor and shear wall interface for the last 200-psi load cycle and the failure cycle using corrected data.



accentuated the appearance of discontinuities in slope at loads where cracks occur. A comparison of Figs. 87 and 88, with Figs. 83 and 84 demonstrates this point. Figure 85 suggests that the removal of rigid body motion introduces noise into the results, but here consideration must be given to magnitudes, i.e., 0.0001 in., between divisions.

Similar figures have been prepared for the interface of the shear wall and ceiling. Results from the uncorrected data are shown in Figs. 89-92. These figures show the same characteristics as those of the floor and shear wall interface.

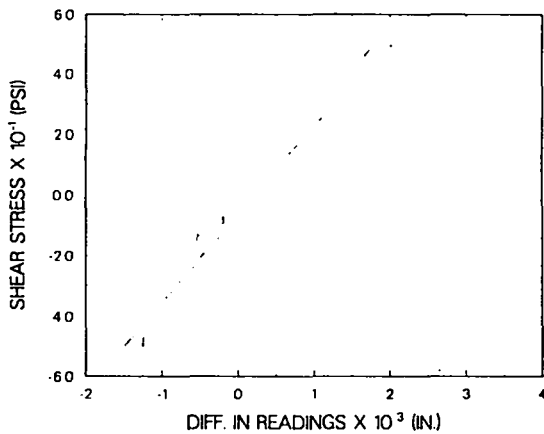


Fig. 89. Relative motion at the shear wall and ceiling interface for the 50-psi load cycles using uncorrected data.

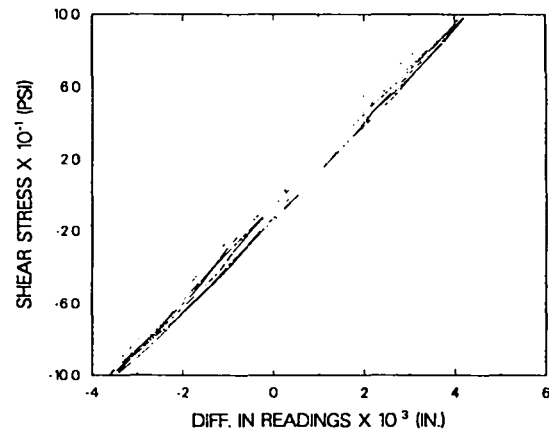


Fig. 90. Relative motion at the shear wall and ceiling interface for the 100-psi load cycles using uncorrected data.

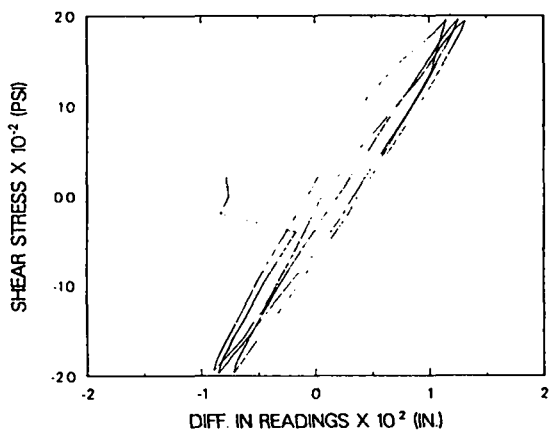


Fig. 91. Relative motion at the shear wall and ceiling interface for the 200-psi load cycles using uncorrected data.

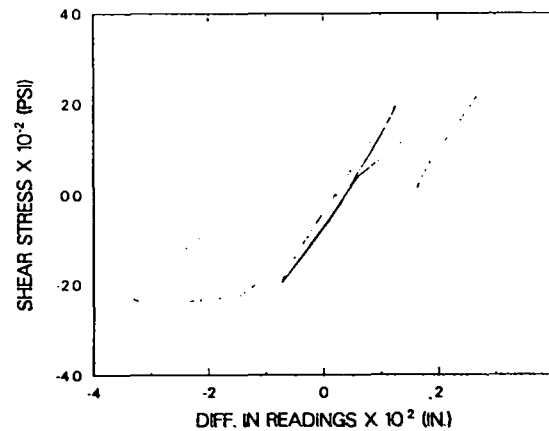


Fig. 92. Relative motion at the shear wall and ceiling interface for the last 200-psi load cycle and the failure load cycle using uncorrected data.

Figure 91 demonstrates that three bad data points were recorded. Also, the cracks that occurred around 130 psi at the shear wall/floor interface did not occur at the shear wall/ceiling interface. The results of the last 200-psi cycle and the fracture cycle presented in Fig. 92 show that a fracture at the interface occurred below 200 psi for the negative load. The results from the gage readings after correction for rigid body motion are given for purposes of comparison in Figs. 93-96.

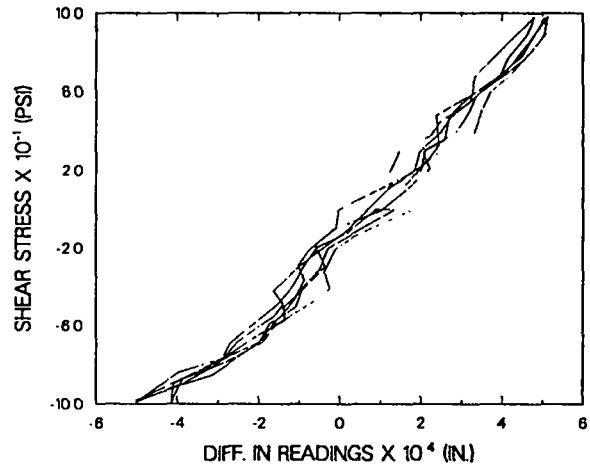
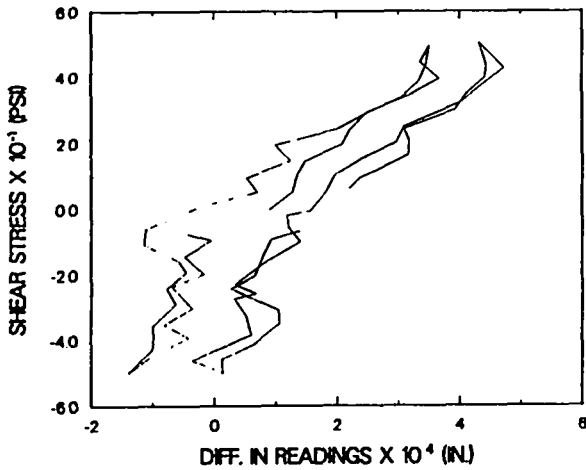


Fig. 93. Relative motion at the shear wall and ceiling interface for the 50-psi load cycles using corrected data.

Fig. 94. Relative motion at the shear wall and ceiling interface for the 100-psi load cycles using corrected data.

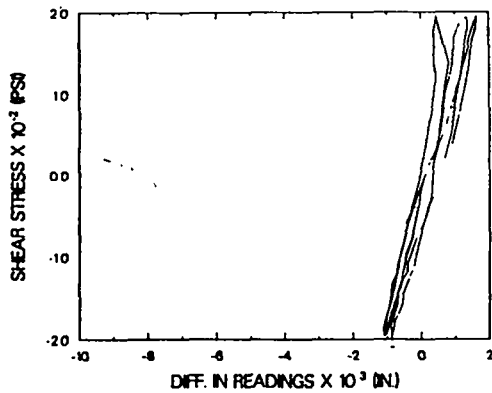


Fig. 95. Relative motion at the shear wall and ceiling interface for the 200-psi load cycle using corrected data.

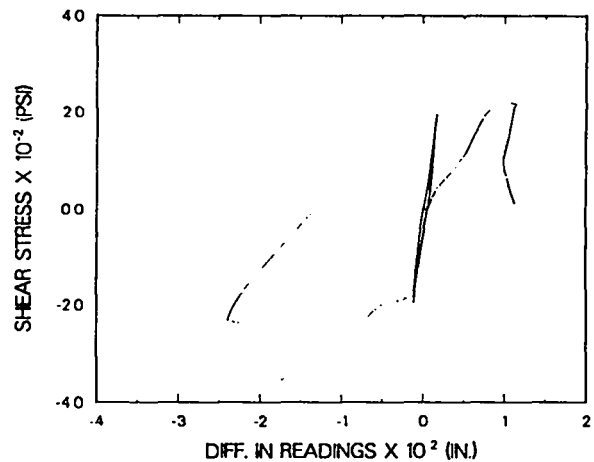


Fig. 96. Relative motion at the shear wall and ceiling interface for the last 200-psi load cycle and the failure load cycle using corrected data.

## IX. HYSTERETIC ENERGY LOSSES IN THE TRG-4 STRUCTURE

The hysteretic energy losses that occurred during each load cycle were deduced based on the displacement determined from the interior relative displacement gages. Data from the exterior gages were also examined, but the results were not as consistent, even with the corrections for rigid body motion. For all the load cycles, the hysteretic energy losses have been related to equivalent viscous damping coefficients.

Table XI summarizes the hysteretic energy losses measured during each load cycle. The hysteretic energy loss is defined as the area between the load deformation curve (Fig. 97) and was calculated numerically using a trapezoid integration rule. Several load cycles did not form a closed load deformation loop. When this occurred, the integration scheme connected the terminal point with a straight line to the initial point. Errors induced by this scheme were considered negligible.

To obtain an equivalent viscous damping coefficient, the energy dissipated by viscous damping,  $U_{VD}$ , in a linear single degree of freedom during

TABLE XI  
HYSTERETIC ENERGY LOSSES FOR TRG-4

Load Cycle	Peak Average Base Shear Stress (psi)	Peak Force (lb)	Hysteretic Energy Loss (in./lb)	Equivalent Viscous Damping (% of critical)
1	50	27,000	29	5.9
2	50	27,000	35	7.0
3	100	54,000	113	5.2
4	100	54,000	81	3.7
5	100	54,000	77	3.5
6	200	108,000	1,560	*
7	200	108,000	940	5.7
8	200	108,000	888	4.9
9	260	140,400	16,400	*
10	50	27,000	582	6.3

\*Cycles that exhibited nonlinear response. Stiffness was not well defined during these cycles.

FIRST 50 PSI LOAD CYCLE - TRG4

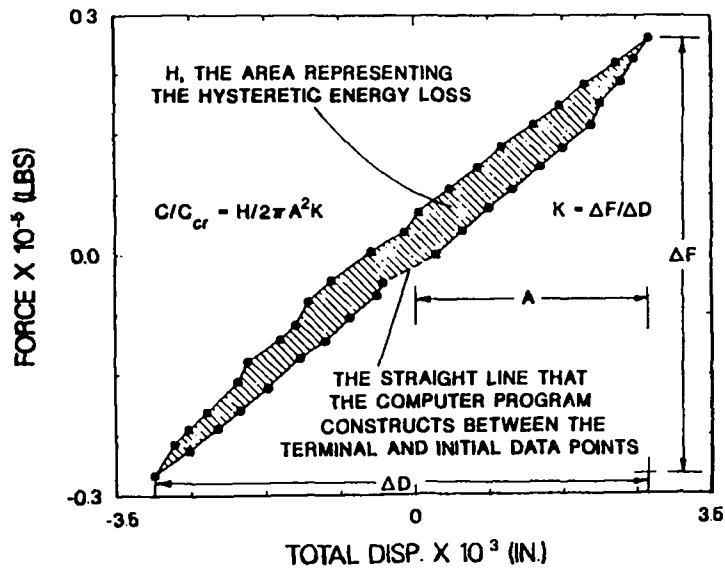


Fig. 97. Definitions of the quantities used to calculate the hysteretic energy loss per cycle.

steady-state response to one cycle of harmonic forced excitation is equated to the hysteretic energy loss,  $U_H$ , during one cycle of static loading. From Ref. 21, the energy lost because of viscous damping is

$$U_{VD} = \pi C A^2 \omega \quad , \quad (2)$$

where

- C = viscous damping coefficient,
- A = amplitude of steady-state vibration,
- $\omega$  = frequency of steady-state vibration,

and

$$U_H = H \quad , \quad (3)$$

where

H = area within the hysteresis loop.

Equating Eqs. (2) and (3) yields

$$C = \frac{H}{\pi A^2 \omega} \quad (4)$$

For a single-degree-of-freedom system, the critical damping coefficient,  $C_c$ , is defined as

$$C_c = 2\sqrt{km} \quad (5)$$

where

$k$  = the structure's stiffness,

$m$  = the structure's mass.

Dividing both sides of Eq. (4) by  $C_c$  yields

$$\frac{C}{C_c} = \frac{H}{2\pi A^2 \omega \sqrt{km}} \quad (6)$$

As stated in Ref. 21 the most significant influence of damping occurs around the resonant frequency, and, for a single-degree-of-freedom system, that frequency can be expressed as

$$\omega = \sqrt{\frac{k}{m}} \quad .$$

Substituting Eq. (5) into Eq. (6) yields the expression used to calculate the equivalent viscous damping values shown in Table XI.

$$\frac{C}{C_c} = \frac{H}{2\pi A^2 k} \quad .$$

This calculation gives the most accurate results during cycles where the response was linear and where the stiffness was thus well defined. The stiffness was calculated as shown in Fig. 97.

These equivalent viscous damping computations yielded values similar to those measured on the microconcrete isolated shear walls (Ref. 2). The values measured on TRG-4 are comparable to those reported by Housner,<sup>22</sup> et al., 5% of critical, and those allowed by NRC Regulatory Guide 1.61<sup>23</sup> for an operating basis earthquake or 1/2 safe shutdown earthquake, 4% of critical. The damping at low stress values suggested by Newmark and Hall<sup>24</sup> are much lower than those determined in this investigation. As an example, Newmark and Hall suggest values of 0.5-1.0% of critical before cracking, and values of 3.3-6.6% of critical were measured before cracking on TRG-4. The damping values measured on TRG-4 also compare favorably with the average measured data from nuclear power plant shear wall buildings reported in Ref. 25. The buildings were tested at stress levels below 25% of yield, and an average damping value of 5.2% of critical was determined from these data.

During the first 200-psi ABSS cycle, the structure cracked and the hysteresis area was considerably larger than that found during the previous load cycles. However, the subsequent load cycles at 200-psi ABSS had a hysteretic energy loss that was only on the average of 58% of the loss during the first cycle. This finding implies that the damping that occurs during the first nonlinear load cycle is significantly greater than that which occurs during subsequent cycles at a similar or lower load level. Also, this result implies that the damping in the nonlinear range is a function of the structure's prior load history. The largest energy loss occurred during the failure cycle (260 ABSS, Cycle 9), as expected.

Finally, it is of interest to compare the hysteretic energy loss before and after the structure failed. During the first two 50-psi ABSS cycles the energy loss averaged 32.5 in./lb while an energy loss of 582 in./lb was measured during the final 50-psi ABSS cycle. The equivalent viscous damping was measured at an average value of 6.2% of critical initially and was found to be 6.3% of critical during the final cycle. The damping value calculated during the final cycle is an example of where the assumption of a constant viscous damping mechanism and the assumptions regarding the structure's stiffness can give misleading values for a damping coefficient. It is clear that percent equivalent viscous damping can be wildly misinterpreted if care is not taken in analytical modeling of nonlinear structures.

## X. OTHER INVESTIGATORS' RESULTS

Figures 98-101 provide a summary of the available static test data for low-aspect-ratio reinforced concrete shear walls. These figures give a comparison between other investigators' results and the results obtained in the Seismic Category I Structures Program.

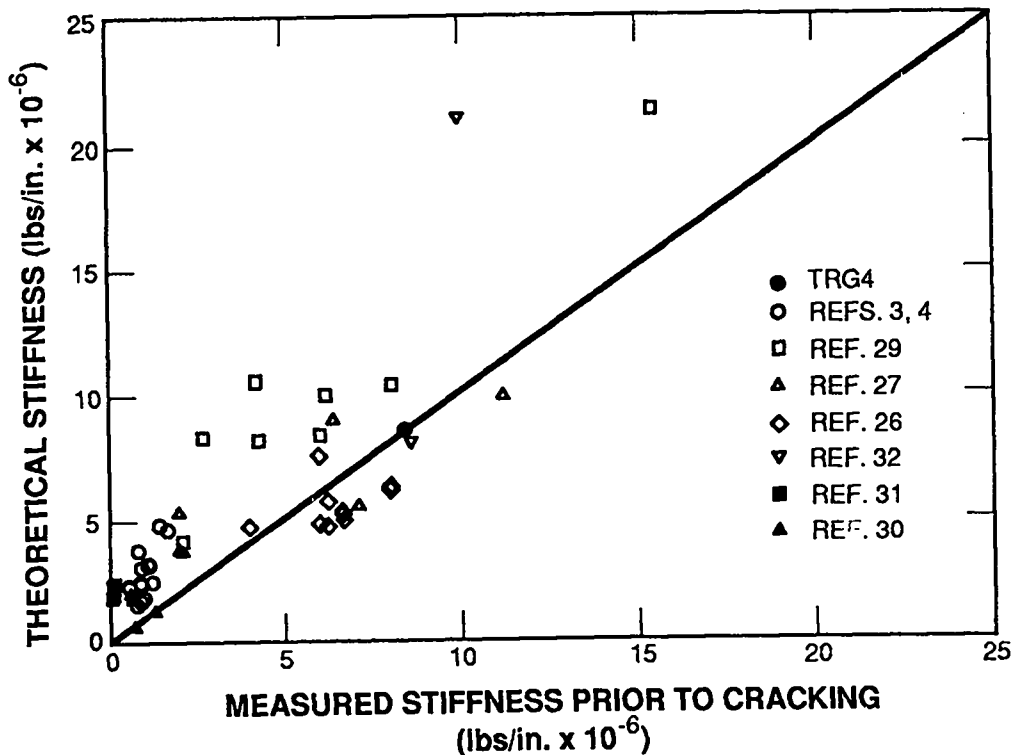


Fig. 98. Other investigators' results: theoretical versus measured stiffness.

At first cracking, the measured secant stiffness versus theoretical (SOM) stiffness is plotted in Fig. 98. The majority of test data on actual concrete test specimens, including the structure tested in this investigation, indicates that, before cracking, an SOM analysis gives an accurate prediction of the shear wall's stiffness. Microconcrete, however, seems to show a considerable reduction in stiffness before the first cracking load. Several investigations of actual concrete structures report similar reductions in stiffness before cracking such as those observed in LANL's microconcrete models.

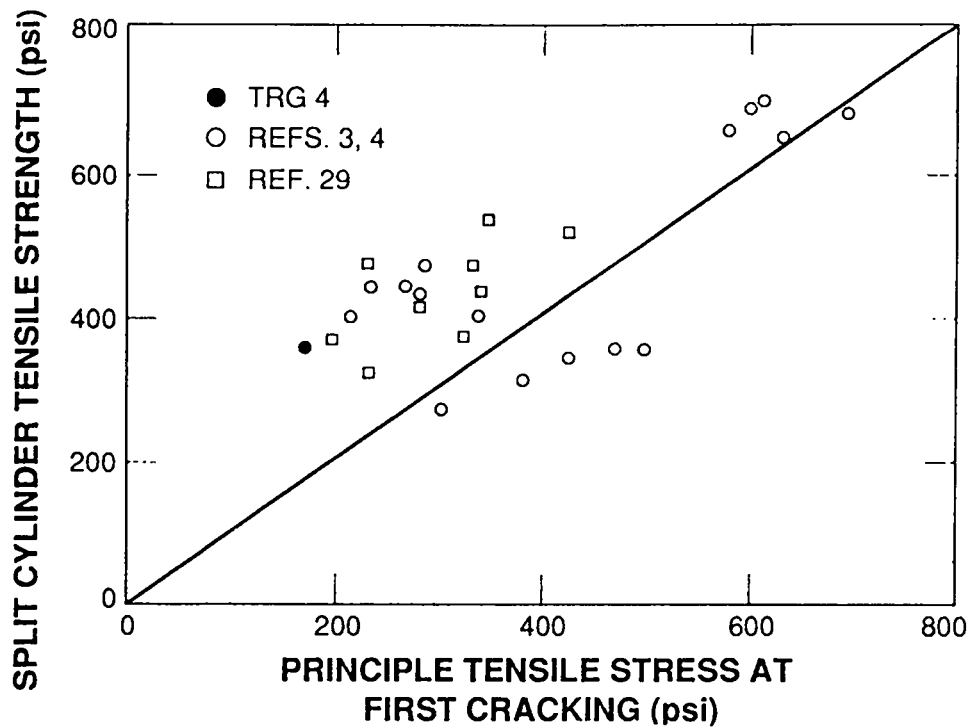


Fig. 99. Other investigators' results: split cylinder tensile strength versus principal stress at first cracking.

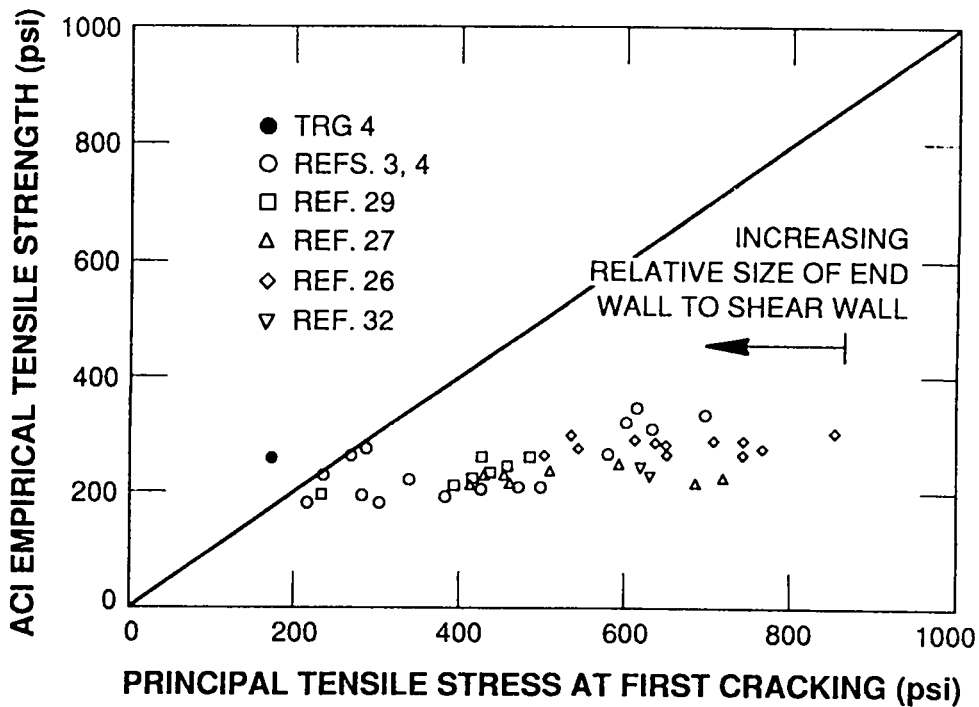


Fig. 100. Other investigators' results: ACI tensile strength versus principal stress at first cracking.



Figures 99 and 100 compare the principal tensile stress at first cracking with the measured split cylinder tensile strength and the empirical tensile strength value specified by ACI 349-85 as  $(4 \sqrt{f'_c})$ . From these plots, it is evident that the ACI value is conservative while the measured split cylinder tensile strength seems to overpredict the stress values that have been obtained at first cracking in actual testing. The larger the relative size of the end wall to the shear wall, the less conservative the ACI value becomes.

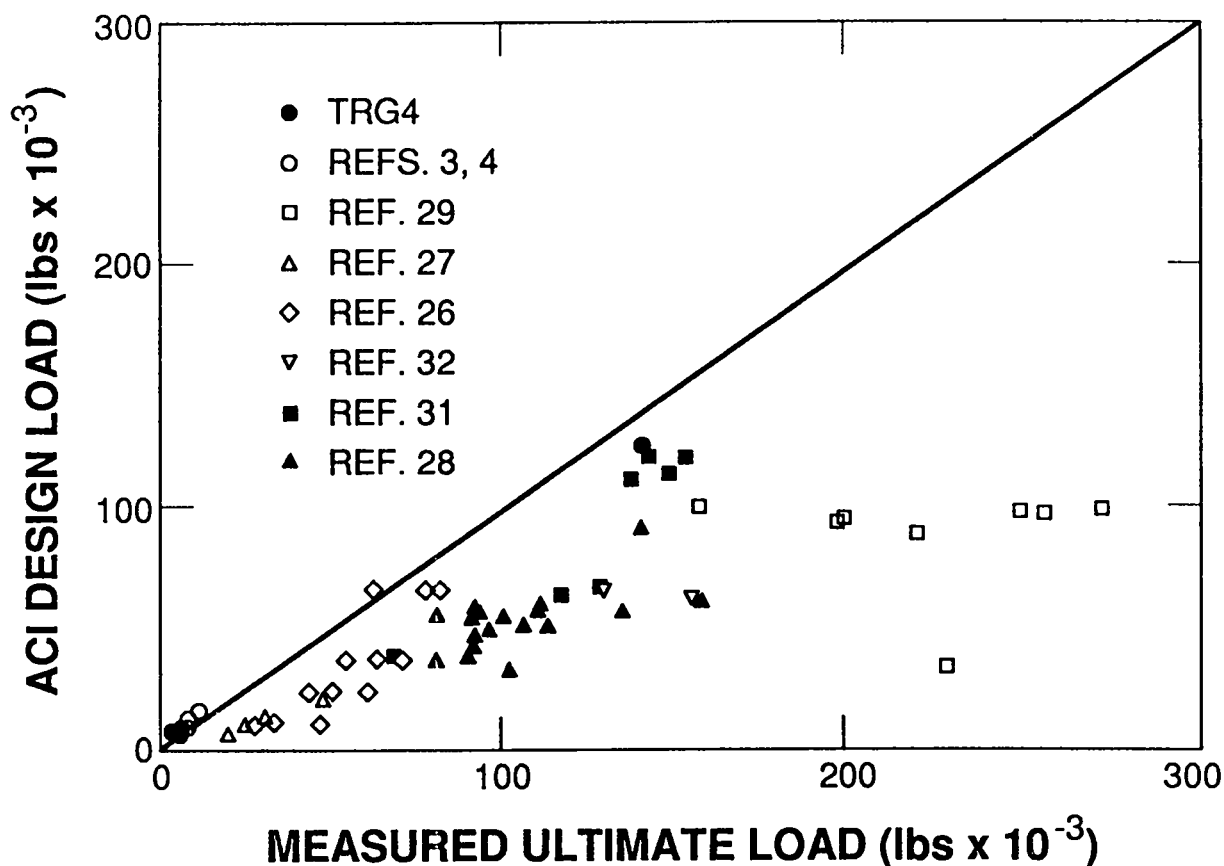


Fig. 101. Other investigators' results: ACI design load versus ultimate load.

Finally, Fig. 101 compares the ultimate strength of the shear walls with ACI 349-85's design strength. In almost all cases, the ACI value appears to be conservative. Data for Figs. 95-101 were obtained from Refs. 3, 4, 26-32.

## XI. CONCLUSIONS

One of the primary purposes of this test was to determine whether, during a carefully monitored static load cycle test, a stiffness reduction of four would occur at similar load levels as had been observed in dynamic tests. During the precracking load cycles and the low-level modal analysis, no stiffness reduction was observed, and the response of the structure was accurately predicted with currently used linear analysis techniques based on strength of materials. These same linear analysis techniques have not adequately predicted the dynamic response of structures previously tested in the program even though stress levels during the dynamic tests were well below those required to crack the structure.

Hence, several questions arise about previous tests conducted in this program and the dynamic behavior of actual Seismic Category I structures. In particular, the following possibilities must still be considered. (1) Does microconcrete adequately simulate actual concrete in both static and dynamic response? (2) Were previous models damaged before testing, either by handling or, in the case of smaller structures, shrinkage cracks? (3) Do dynamic effects cause the discrepancy between the reductions in stiffness observed statically and dynamically? (4) Have the boundary conditions been properly accounted for in all testing and analyses? These questions should be answered if possible from future tests.

This test was also instrumented to provide information on the effectiveness of the end walls, and, up until first cracking, they appear to be fully effective. However, the concrete and steel slabs at the top of the structure force the cross-section to remain plane, thus reducing the shear lag effect. After cracking, the extent of the slab's contribution is not clear.

The ability to separate shear and bending components of deformation was clearly demonstrated. Loss of stiffness was shown to occur equally in each component of deformation.

Another model is currently being constructed that is identical to the large model reported in Ref. 5. The previous structure of Ref. 5 was tested dynamically, and the structure being constructed will be tested statically and cyclically in a fashion similar to the one reported here. The direct comparison between static and dynamic tests will be used to further clarify the reduced stiffness issue.

## REFERENCES

1. U.S. Nuclear Regulatory Commission, Office of Nuclear Regulatory Research, "Seismic Safety Research Program Plan," NUREG-1147, Rev. 1, Appendix C, May 1987.
2. E. G. Endebrook, R. C. Dove, and C. A. Anderson, "Margins to Failure-Category I Structures Program: Background and Experimental Program Plan," Los Alamos National Laboratory report LA-9030-MS, NUREG/CR-2347, December 1981.
3. E. G. Endebrook, R. C. Dove, and W. E. Dunwoody, "Analysis and Tests on Small-Scale Shear Walls, FY-82 Final Report," Los Alamos National Laboratory report LA-10443-MS, NUREG/CR-4274, September 1985.
4. R. C. Dove, J. G. Bennett, C. R. Farrar, and C. A. Anderson, "Seismic Category I Structures Program: Final Report, FY 1983-84," Los Alamos National Laboratory report LA-11013-MS, NUREG/CR-4924, September 1987.
5. J. G. Bennett, et al., "Seismic Category I Structures Program: Results for FY 86 Report, Los Alamos National Laboratory report LA-11377-MS, NUREG/CR-5182, September 1988.
6. R. C. Dove and J. G. Bennett, "Scale Modeling of Reinforced Concrete Category I Structures Subjected to Seismic Loading," Los Alamos National Laboratory report LA-10624-MS, NUREG/CR-4474, January, 1986.
7. R. C. Dove, E. G. Endebrook, W. E. Dunwoody, and J. G. Bennett, "Seismic Tests on Models of Reinforced Concrete Category I Buildings," Proc. Int. Conf. Structural Mechanics in Reactor Technology, 8th, Brussels, Belgium, 1985.
8. J. G. Bennett, et al., "Seismic Category I Structures Program: Results for FY 85," Los Alamos National Laboratory report LA-11117-MS, NUREG/CR-4998, December 1987.
9. ACI Committee 349, Code Requirements for Nuclear Safety Related Concrete Structures and Commentary, American Concrete Institute, Detroit, Michigan, 1985.
10. ACI Committee 318, Building Code Requirements for Reinforced Concrete American Concrete Institute, Detroit, Michigan, 1983.
11. "Standard Test Method for Slump of Portland Cement Concrete," in Annual Book of ASTM Standards, Roberta A. Prieman-Storer, Ed. (American Society for Testing and Materials, Philadelphia, Pennsylvania, 1985), Vol. 4.02, C143-78, pp. 109-112
12. "Method of Sampling Freshly Mixed Concrete," in Annual Book of ASTM Standards, Roberta A. Prieman-Storer, Ed. (American Society for Testing and Materials, Philadelphia, Pennsylvania, 1985), Vol. 4.02, C172-82, pp. 133-135.

13. "Standard Method of Making and Curing Concrete Specimen in the Field," in Annual Book of ASTM Standards, Roberta A. Prieman-Storer, Ed. (American Society for Testing and Materials, Philadelphia, Pennsylvania, 1985), Vol. 4.02, C31-84, pp. 5-10
14. "Specification for Concrete Aggregates," in Annual Book of ASTM Standards, Roberta A. Prieman-Storer, Ed. (American Society for Testing and Materials, Philadelphia, Pennsylvania, 1985), Vol. 4.02, C33-85, pp. 11-20.
15. "Standard Test Method for Compressive Strength of Cylindrical Concrete Specimen," in Annual Book of ASTM Standards, Roberta A. Prieman-Storer, Ed. (American Society for Testing and Materials, Philadelphia, Pennsylvania, 1985), Vol. 4.02, C39-84, pp. 24-29.
16. "Standard Test Method for Static Modulus of Elasticity and Poisson's Ratio of Concrete in Compression," in Annual Book of ASTM Standards, Roberta A. Prieman-Storer, Ed. (American Society for Testing and Materials, Philadelphia, Pennsylvania, 1985), Vol. 4.02, C469-83, pp. 303-307.
17. "Standard Test Method for Splitting Tensile Strength of Cylindrical Concrete Specimens," in Annual Book of ASTM Standards, Roberta A. Prieman-Storer, Ed. (American Society for Testing and Materials, Philadelphia, Pennsylvania, 1985), Vol. 4.02, C496-85, pp. 335-339.
18. T. R. Naik, "Ultrasonic Testing of Concrete," in Experimental Methods In Concrete Structures for Practitioners, G. M. Sabnis and N. Fitz Simmons, Eds. (American Concrete Institute, Detroit, Michigan, 1979).
19. E. P. Popov, Introduction to Mechanics of Solids, Prentice-Hall, Englewood Cliffs, New Jersey, 1969.
20. A. E. Cardenas, J. M. Hanson, W. G. Corley, and E. Hognested, "Design Provisions for Shear Walls," J. American Concrete Institute, 70, No. 3, pp. 221-230, March 1973.
21. S. Timoshenko, D. Young, and W. Weaver, Vibration Problems in Engineering, 4th Ed., John Wiley & Sons, Inc., New York, New York, pp. 81-84, 1974.
22. G. W. Housner, R. R. Martel, and J. L. Alford, "Spectrum Analysis of Strong-Motion Earthquakes," Bull. Seismo. Soc. Am., 43, pp. 97-119, 1953.
23. Nuclear Regulatory Guide 1.61, "Damping Values for Seismic Design of Nuclear Power Plants," United States Nuclear Regulatory Commission, December, 1983.
24. H. Newmark and W. Hall, "Seismic Design Criteria for Nuclear Reactor Facilities," in Proc., 4th World Conference on Earthquake Engineering, B4, pp. 37-50, (Santiago, Chile, 1969).
25. J. D. Stevenson, "Structural Damping Values as a Function of Dynamic Response Stress and Deformation Levels," Nuclear Eng. and Design, 60, pp. 211-238.

26. G. D. Galletly, "An Experimental and Analytical Investigation of Reinforced Concrete Shear Panels," Ph.D. Thesis, Department of Civil and Sanitary Engineering, Massachusetts Institute of Technology, Cambridge, Massachusetts, 1952.
27. J. R. Benjamin and H. A. Williams, "The Behavior of One-Story Reinforced Concrete Shear Walls," J. Structural Division, ASCE, 83, No. ST3, Proc. Paper 1254, pp. 1254-1 to 1254-49, May, 1957.
28. J. Antebi, "Model Analysis of the Response of Shear Walls to Dynamic Loads," Ph.D. Thesis, Department of Civil and Sanitary Engineering, Massachusetts Institute of Technology, Cambridge, Massachusetts, 1961.
29. F. Barda, "Shear Strength of Low-Rise Walls with Boundary Elements," Ph.D. Thesis, Department of Civil Engineering, Lehigh University, Bethlehem, Pennsylvania, 1972.
30. V. Cervenka and K. H. Gerstle, "Inelastic Analysis of Reinforced Concrete Panels: Experimental Verification and Application," Publ. Int. Ass. Bridge and Structural Eng., 32-II, 25-40 (1972).
31. A. E. Cardenas, H. G. Russell, and W. G. Corley, "Strength of Low-Rise Structural Walls," in Reinforced Concrete Structures Subjected to Wind and Earthquake Forces, J. Schwaighofer and S. Otani, Eds., ACI SP-63, pp. 221-241, Detroit, Michigan, 1980.
32. S. Wiradinata, "Behavior of Squat Walls Subjected to Load Reversals," Masters Thesis, University of Toronto, Toronto, Canada, 1985.

## APPENDIX A

### STATISTICALLY PLANNED TEST MATRIX

Appendix A is an excerpt from an informal report to the Technical Review Group following a meeting on April 1, 1986. It is reproduced here to clarify the thoughts that went into model selection. The complete plan was never carried out in its entirety because of funding limitations.

STATISTICALLY PLANNED EXPERIMENTS FOR A  
MODEL TO DETERMINE SEISMIC WORKING  
LOAD STIFFNESS AS A FUNCTION OF  
ASPECT RATIO AND PERCENTAGE  
STEEL REINFORCING

by

Charles R. Farrar and Aaron Goldman

This paper summarizes the test plan developed by our statistician, Aaron Goldman, for the upcoming static load deflection tests. In review, at the Technical Review Group (TRG) meeting of April 1, 1986, it was decided to maintain the cross-sectional geometry of the TRG-3 model because it has both shear and bending elements typical of actual Seismic Category I buildings. It was decided to build these structures with different aspect ratios and reinforcement percentages so that variations in these variables that exist in the actual Category I structures could be taken into account in the experiments and so that sensitivity to these variables could be identified. The TRG suggested that aspect ratios vary from 0.25 to 1.0 and that reinforcement percentages range from 0.125% to 1.0% each face, each direction.

A matrix of tests with varying aspect ratios and reinforcement percentages, Fig. A-1, was set up to aid in the development of a test plan. At present, it is felt that the nine points identified as A, B, and C on the matrix, coupled with existing test results, will provide an adequate data base for determining reductions in stiffness as a function of aspect ratio and percentage reinforcing steel.

The test plan begins by sequentially analyzing the four extreme points in the matrix (marked A) with one model each. The value of the stiffness ratio,  $K_{\text{measured}}/K_{\text{theory}}$  will be plotted versus aspect ratio and percent reinforcement. A surface will be fitted through these four points and points from previous tests in this program. These four extreme points are optimal choices in the sense that variances in estimates of  $K_m/K_t$  will be minimized.<sup>(1)</sup>

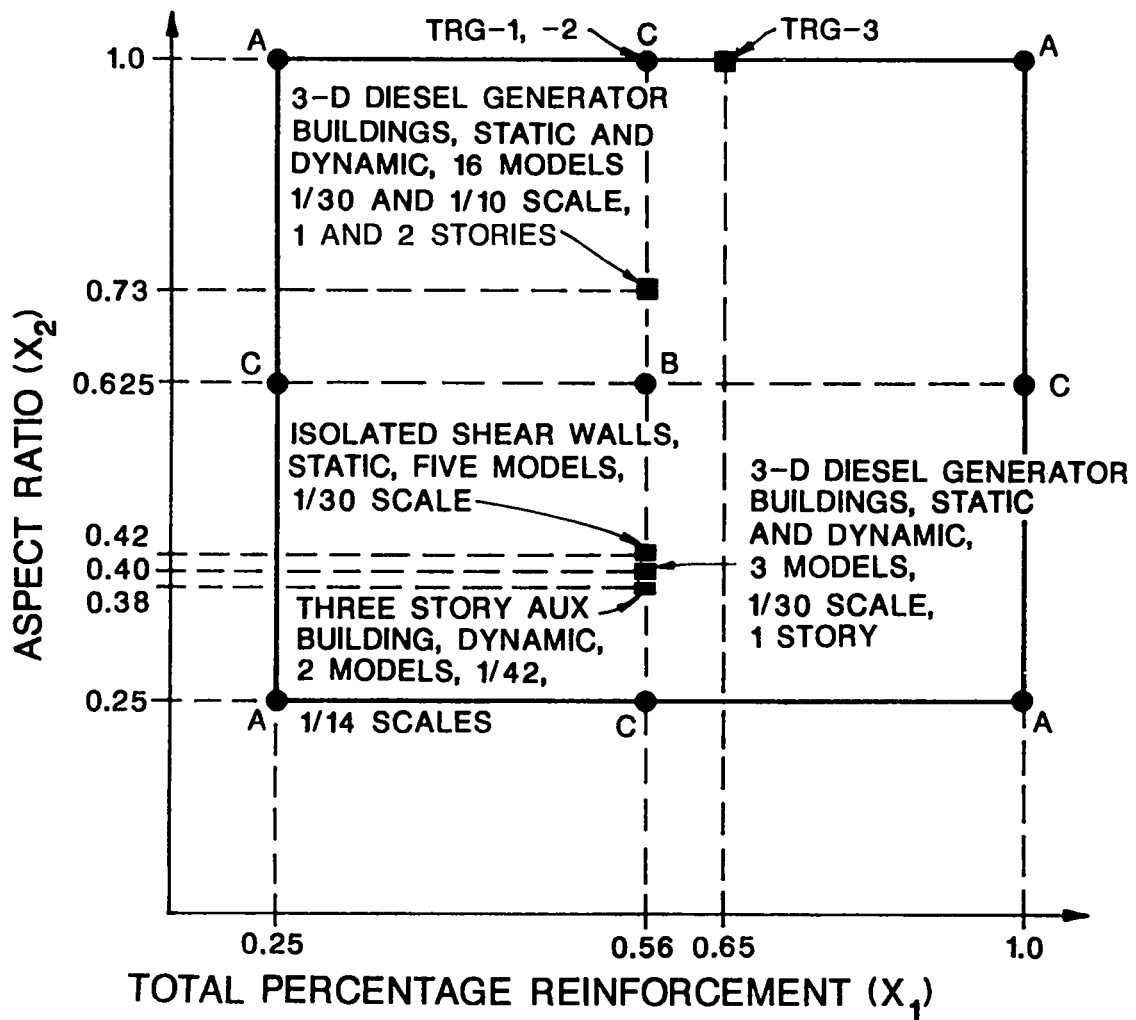


Fig. A-1. Test matrix.

The surface has the following analytical form

$$y = \beta_0 + \beta_1 x_1 + \beta_2 x_2 \quad , \quad (A-1)$$

where

$y = K_m / K_T$  ,  
 $\beta_0, \beta_1, \beta_2$  are parameters to be estimated by the surface fit,  
 $x_1$  = the variable representing reinforcement percentage, and  
 $x_2$  = the variable representing aspect ratio.



Next, an additional two tests will be performed at a percentage reinforcement of 0.56 and an aspect ratio of 0.625, Point B on the matrix. The first of these two tests is needed in order to perform a statistical analysis that includes testing for a lack of fit of Eq. (A-1). If there is a lack of fit, then the actual surface will be a higher-order surface (there is a "hump" in the surface), and the results from the test corresponding to Point B will not fall near the previously generated surface, that is, the one initially generated from Points A and all previous test data. The second test to be performed with the aspect ratio and percentage reinforcement of Point B will be used along with the first test at this point to measure the test-to-test variation of the stiffness. The two tests conducted at the center of the matrix, Point B, are included as part of the overall test matrix as recommended by Box and Draper.<sup>(2)</sup>

A check will be made to see how well the results corresponding to Point B fall on the surface generated with Points A and the previous data. If these points fit satisfactorily, they will be included with the first four, Points A, and the previous tests, and an updated version of the surface of the form of Eq. (A-1) will be generated.

If the two new points do not fall near the surface determined by the four Points A and the previous tests, then only the five points defined by Points A and B on the matrix will be used to generate the parameters in Eq. (A-1), i.e., previous data will not be used. In this case, the assumption being made about the previous test data taken in this program is that these data may have introduced sources of error, such as microconcrete effects and shipping damage. The effects of these types of error are reduced using models represented by Points A and B on the matrix because the models will be built, cured, and tested in as identical a fashion as possible using standard concrete and rebar. If Point B falls on the surface generated with Points A and the previous test data, there will be a good indication that the above-mentioned sources of error are insignificant in the determination of stiffness. In some sense, an estimate of the magnitude of these effects can be made by comparing surfaces generated by including the effects, by not including the effects, and by generating a plane using effects alone.

In either case, a statistical analysis will quantify how well the generated surface matches the data. If the generated surface is adequate, two additional tests will be made at optimal locations determined from the

analysis to further refine the surface. The location of these two additional tests on the matrix will be somewhat subjective and will be based on results from the previous tests and the tests corresponding to Points A and B. For example, if we find a large variance at Point B, we may wish to make the additional points correspond to B to further refine our estimate of the variance, or, if a data point is in question as the result of some error in fabrication or testing, we may wish to retest at the particular point on the matrix. Also, if, in the course of testing, a point not currently identified on the matrix becomes of interest, we could make it one of the additional test points. Obviously, the number of additional test points is somewhat arbitrary, but we hope two will be sufficient.

If the generated surface is not adequate, the additional points (marked C on the matrix) will be tested to develop a higher-order surface of the following form.

$$y = \beta_0 + \beta_1 x_1 + \beta_2 x_2 + \beta_3 x_1^2 + \beta_4 x_2^2 + \beta_5 x_1 x_2 \quad , \quad (A-2)$$

where

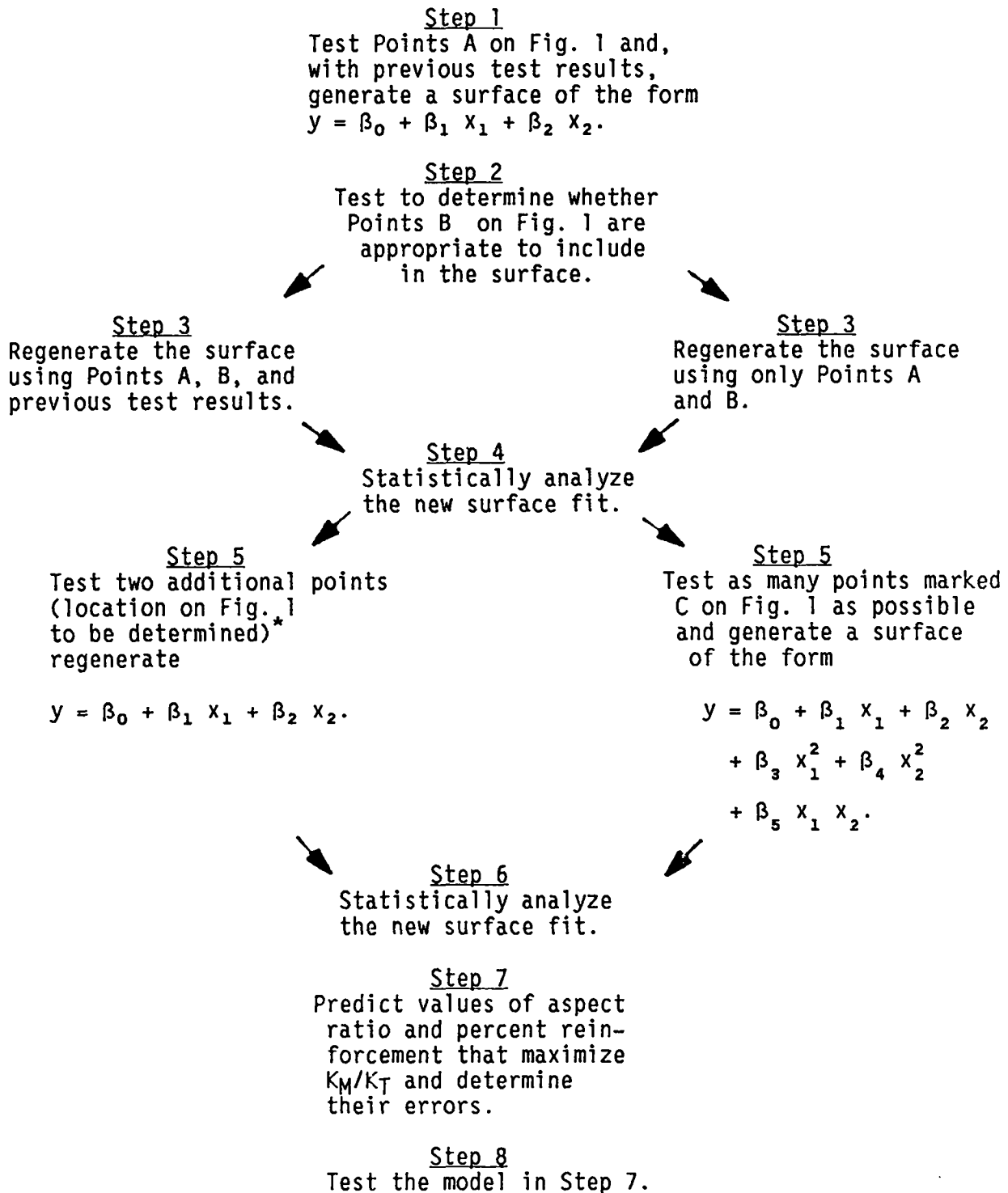
$\beta_i$   $i = 0, 1, 2 \dots 5$  are constants to be determined ,

$y, x_1, x_2$  are the same as Eq. (A-1).

Finally, a statistical analysis will provide percent reinforcement,  $x_1$ , and the aspect ratio,  $x_2$ , which maximizes  $K_m/K_T$ , and will also provide the appropriate error bounds on this maximum. This point,  $(x_1, x_2)$ , will then be used as a final test of the surface fit.

A flow chart summarizing the steps in this procedure is shown in Fig. A-2.

At this point, in addition to developing a test plan, a building in which the model can be constricted and tested in place has been secured, and plans for a load frame have been developed. The plans are currently being drawn up so that fabrication can begin. It is estimated that the load frame will cost less than \$15,000. A model with an aspect ratio of one and a reinforcement percentage of 0.125 will be the first structure tested because we can use the forms from the TRG-3 model.



\*Analysis of results up to this step will determine locations of these tests on Fig. 1.

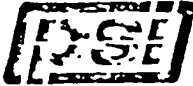
Fig. A-2. Testing flow chart.

## REFERENCES

1. G. E. P. Box, W. G. Hunter, and J. S. Hunter, Statistics for Experimenters, (John Wiley and Sons, Inc., New York, 1978), pp. 471-472.
2. G. E. P. Box and N. R. Draper, "A Basis for the Selection of a Response Surface Design," Journal of the American Statistical Association, 54, 652-654 (1959).

APPENDIX B

MATERIAL PROPERTIES TEST TRG-4



**Professional Service Industries, Inc.**  
 Albuquerque Testing Laboratory Division

**CLIENT:** Los Alamos National  
 Laboratory  
 MS J576  
 Los Alamos, New Mexico 87545

**PROJECT:** Mechanical Properties of  
 Concrete - Category I  
 Seismic TRC 6 Inch-Wall

FO Number: 2-LSH E086LI

Attn: Mr. Chuck Ferrar

**DATE:** March 18, 1987

**PSI REPORT NO.:** 534-70011 REVISED

As requested, Report No. 534-70011 has been reviewed. It was determined that the data obtained from the compressionometer was incorrectly interpreted. The deflection data from the compressionometer apparatus has been reduced by a factor of two (2) to obtain the actual deflection of the test cylinder. The modifications to the test data have been made in this report and the corresponding modulus of elasticities have been calculated.

**INTRODUCTION:**

Twenty-eight (28) concrete cylinders (6 in. diameter by 12 in. long) were delivered to our laboratory by LANL personnel. The specimens represented two batches of ready mixed concrete which have been identified as Mix 1 from Truck 1 and Mix 2 from Truck 2. The age at time of testing was more than 28 days. (Cast on December 9, 1986).

**PROCEDURE:**

Twenty (20) of the cylinders (10 from each mix) were tested in compression to determine the Modulus of Elasticity according to ASTM C 459-81 procedure. Eight (8) of the cylinders (4 from each mix) were tested using the splitting tensile procedure according to ASTM C 496-71, to determine the tensile strength.

The weight of twelve uncapped (12) test specimens was measured to the nearest 0.01 lb. The test set-up for the compression test is shown in Figure 1. A typical failed compression test specimen is shown in Figure 2 and the typical failure made is shown in Figure 3. The test set-up for the indirect tension test is shown in Figure 4, and a typical failed tensile test specimen is shown in Figure 5.

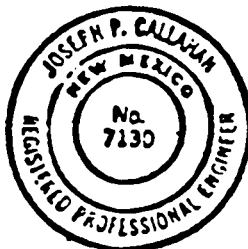
**RESULTS:**

The results are summarized on the following data sheets.

Respectfully submitted,

ALBUQUERQUE TESTING LABORATORY  
 DIVISION

*J. Patrick Callahan*  
 J. Patrick Callahan, P.E.  
 Vice President



JFC:rv

YOUNG'S MODULUS DATA

REFERENCE: ASTM Designation C469-B1;  
Standard Test Method for  
STATIC MODULUS OF ELASTICITY AND  
POISSON'S RATIO OF CONCRETE IN  
COMPRESSION

	SPECIMEN	YOUNG'S MODULUS (PSI)
MIX 1	1	3.11E+06
	2	3.11E+06
	3	3.09E+06
	4	3.07E+06
	5	3.02E+06
	6	3.19E+06
	7	3.10E+06
	8	3.08E+06
	9	3.16E+06
	10	2.96E+06
MIX 2	1	3.27E+06
	2	3.51E+06
	3	3.54E+06
	4	3.11E+06
	5	3.18E+06
	6	3.17E+06
	7	3.39E+06
	8	3.71E+06
	9	3.22E+06
	10	3.54E+06

CYLINDER WEIGHTS

	WEIGHT (LBS)
MIX 1	26.70
	26.80
	27.10
	26.85
	27.10
	27.00
27.00	
MIX 2	27.10
	27.30
	27.20
	27.60
	27.40

SPLITTING TENSILE TEST DATA

REFERENCE: ASTM Designation C496-71;  
Standard Test Method for  
SPLITTING TENSILE STRENGTH OF  
CYLINDRICAL CONCRETE SPECIMENS

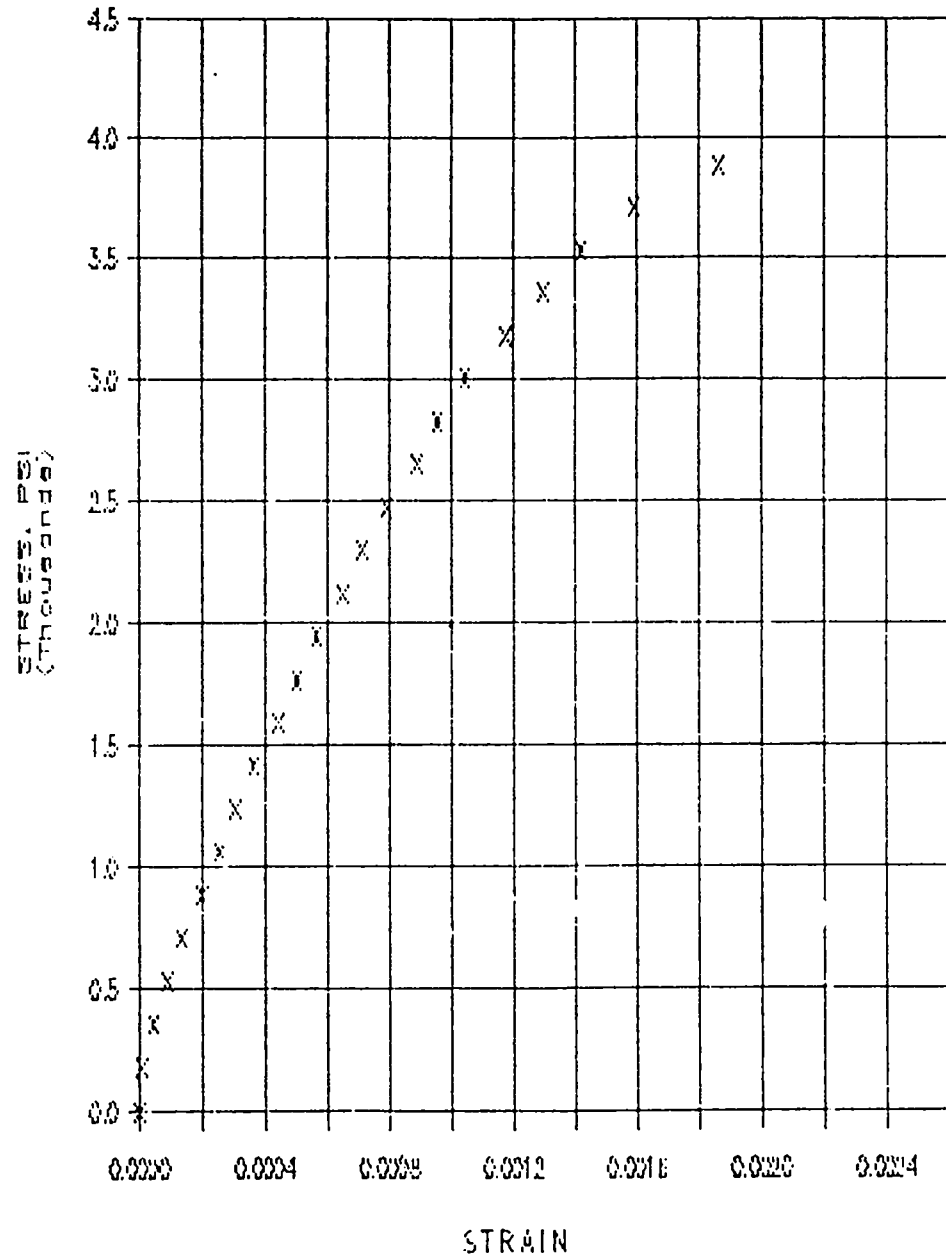
	FRACTURE LOAD (LBS) ÷1000	SPLITTING TENSILE STRENGTH (PSI)
MIX 1	34.2	302.4
	43.4	383.7
	41.0	362.5
	39.5	352.6
MIX 2	43.7	386.4
	42.1	372.2
	39.5	349.3
	39.4	348.4

## TEST DATA

MIX 1: SPECIMEN 1

DATE TESTED: 1/26/87

LOAD (LBS) *1000	STRESS (PSI)	READING (IN) *0.0001	DEFORM. (IN) *0.0001	STRAIN
0.0	0.00	0	0.0	0.00000
5.0	176.84	1	0.5	0.00001
10.0	353.68	7	3.5	0.00004
15.0	530.52	14	7.0	0.00009
20.0	707.36	22	11.0	0.00014
25.0	884.20	32	16.0	0.00020
30.0	1061.03	41	20.5	0.00026
35.0	1237.87	49	24.5	0.00031
40.0	1414.71	58	29.0	0.00036
45.0	1591.55	70	35.0	0.00044
50.0	1768.39	80	40.0	0.00050
55.0	1945.23	90	45.0	0.00056
60.0	2122.07	104	52.0	0.00065
65.0	2298.91	114	57.0	0.00071
70.0	2475.75	127	63.5	0.00079
75.0	2652.59	142	71.0	0.00089
80.0	2829.42	153	76.5	0.00096
85.0	3006.26	167	83.5	0.00104
90.0	3183.10	186	94.0	0.00118
95.0	3359.94	207	103.5	0.00129
100.0	3536.78	227	113.5	0.00142
105.0	3713.62	255	127.5	0.00159
110.0	3890.46	298	149.0	0.00186
110.5	3908.14	FRACTURE		

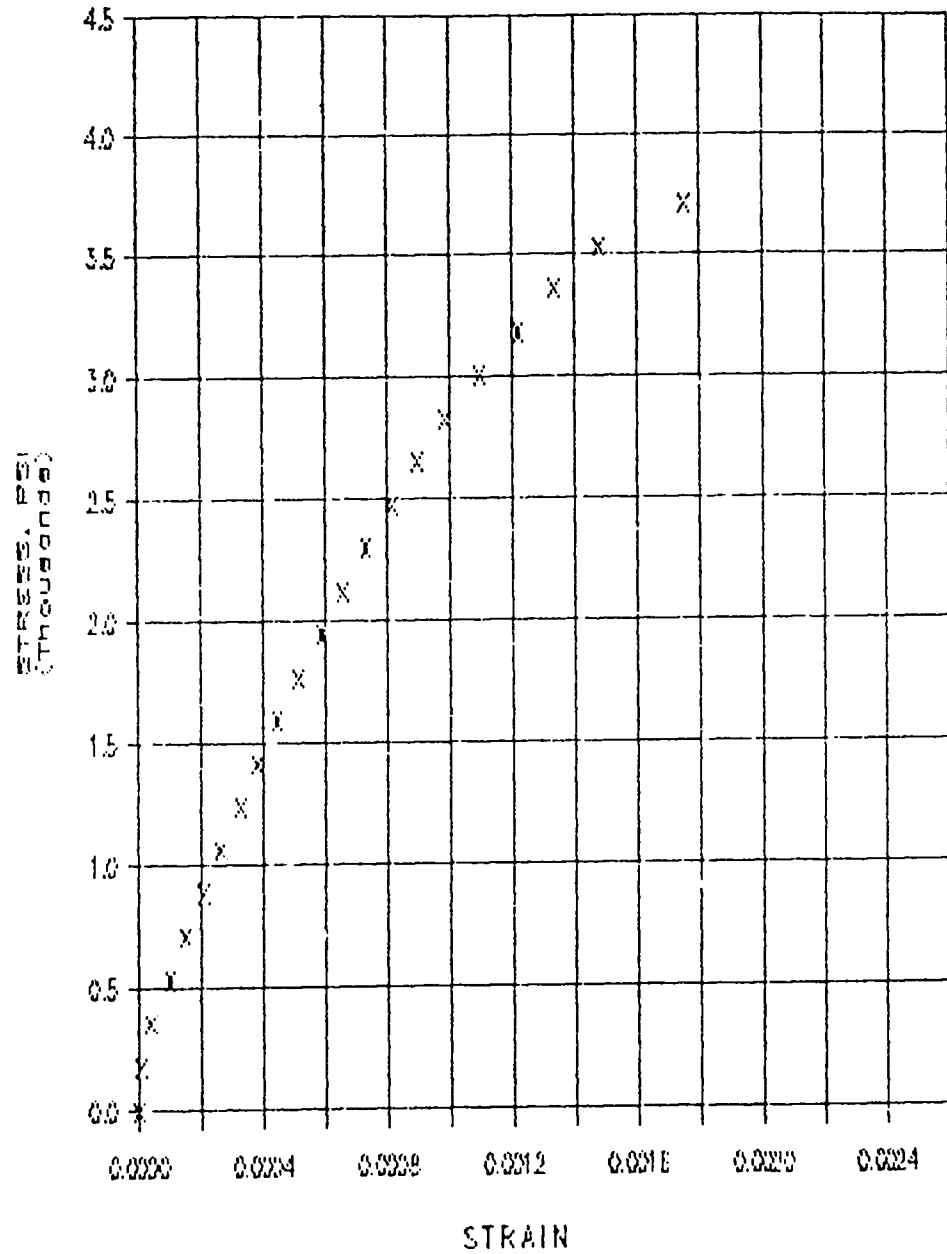




MIX 1: SPECIMEN 2

DATE TESTED: 1/26/87

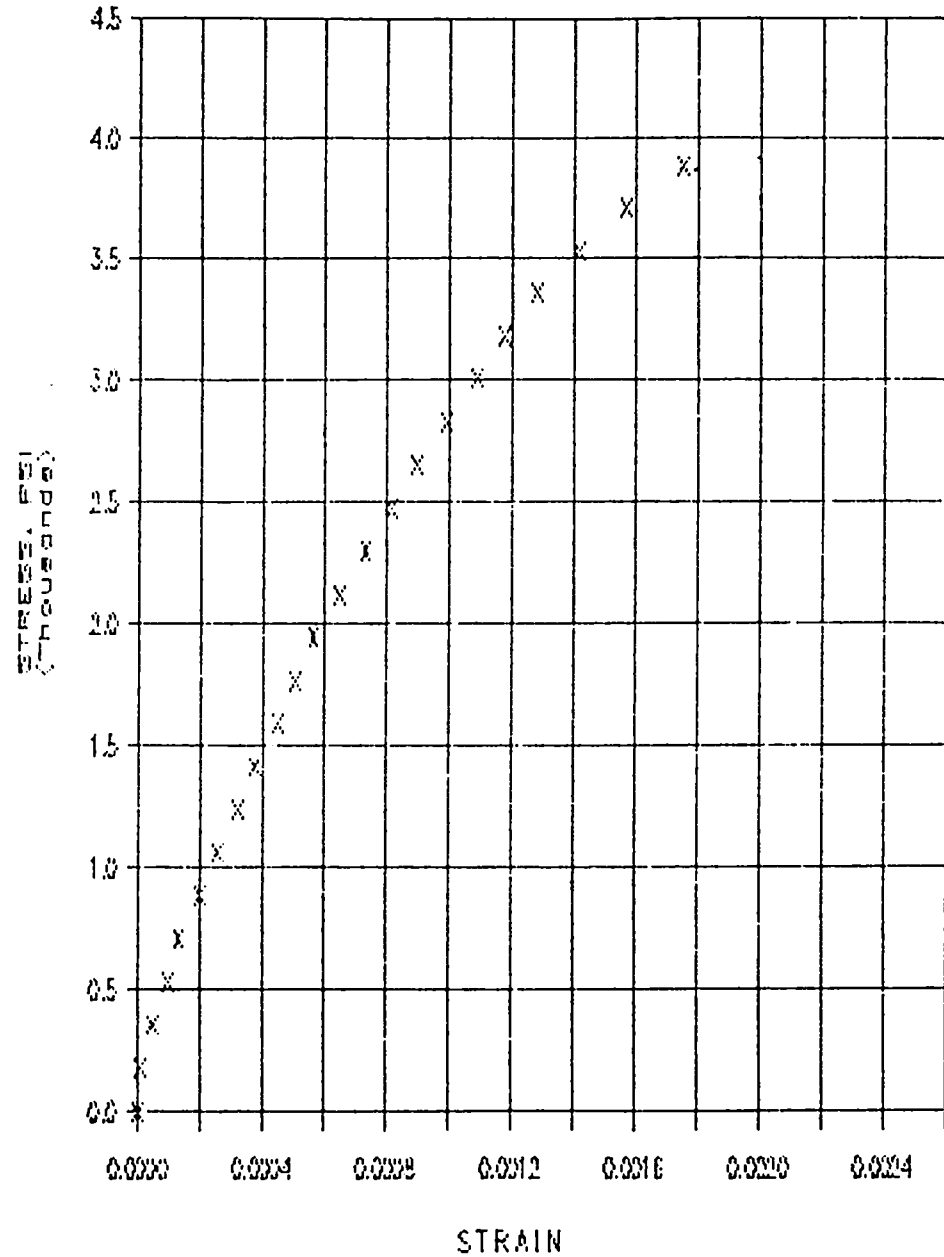
LOAD (LBS) *1000	STRESS (PSI)	READING (IN) *0.0001	DEFORM. (IN) *0.0001	STRAIN
0.0	0.00	0	0.0	0.00000
5.0	176.84	1	0.5	0.00001
10.0	353.68	6	3.0	0.00004
15.0	530.52	16	8.0	0.00010
20.0	707.36	24	12.0	0.00015
25.0	884.20	33	16.5	0.00021
30.0	1061.03	42	21.0	0.00026
35.0	1237.87	52	26.0	0.00033
40.0	1414.71	61	30.5	0.00038
45.0	1591.55	71	35.5	0.00044
50.0	1768.39	82	41.0	0.00051
55.0	1945.23	94	47.0	0.00059
60.0	2122.07	105	52.5	0.00066
65.0	2298.91	117	58.5	0.00073
70.0	2475.75	130	65.0	0.00081
75.0	2652.59	143	71.5	0.00089
80.0	2829.42	157	78.5	0.00098
85.0	3006.26	175	87.5	0.00109
90.0	3183.10	195	97.5	0.00122
95.0	3359.94	214	107.0	0.00134
100.0	3536.78	237	118.5	0.00148
105.0	3713.62	280	140.0	0.00175
107.0	3784.36	FRACTURE		



MIX 1: SPECIMEN 3

DATE TESTED: 1/26/87

LOAD (LBS) *1000	STRESS (PSI)	READING (IN) *0.0001	DEFORM. (IN) *0.0001	STRAIN
0.0	0.00	0	0.0	0.00000
5.0	176.84	1	0.5	0.00001
10.0	353.68	8	4.0	0.00005
15.0	530.52	15	7.5	0.00009
20.0	707.36	21	10.5	0.00013
25.0	884.20	32	16.0	0.00020
30.0	1061.03	41	20.5	0.00026
35.0	1237.87	51	25.5	0.00032
40.0	1414.71	60	30.0	0.00036
45.0	1591.55	72	36.0	0.00045
50.0	1768.39	81	40.5	0.00051
55.0	1945.23	90	45.0	0.00056
60.0	2122.07	104	52.0	0.00065
65.0	2298.91	117	58.5	0.00073
70.0	2475.75	130	65.0	0.00081
75.0	2652.59	143	71.5	0.00089
80.0	2829.42	159	79.5	0.00096
85.0	3006.26	174	87.0	0.00109
90.0	3183.10	188	94.0	0.00116
95.0	3359.94	205	102.5	0.00126
100.0	3536.78	226	113.0	0.00141
105.0	3713.62	251	125.5	0.00157
110.0	3890.46	280	140.0	0.00175
114.0	4031.93	FRACTURE		

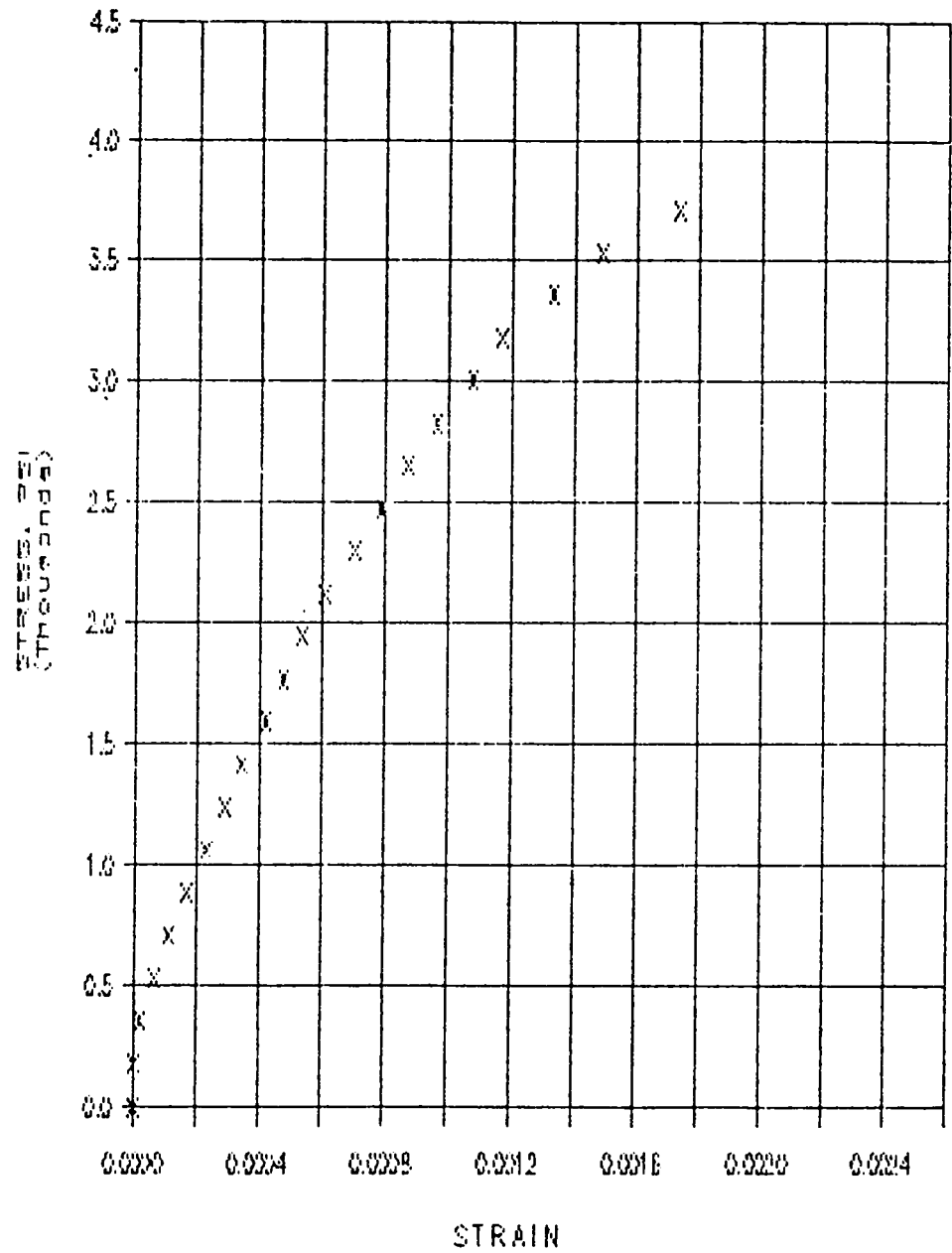


TEST DATA

MIX 1: SPECIMEN 4

DATE TESTED: 1/26/87

LOAD (LBS) *1000	STRESS (PSI)	READING (IN) *0.0001	DEFORM. (IN) *0.0001	STRAIN
0.0	0.00	0	0.0	0.00000
5.0	176.84	0	0.0	0.00000
10.0	353.68	3	1.5	0.00002
15.0	530.52	10	5.0	0.00006
20.0	707.36	18	9.0	0.00011
25.0	884.20	27	13.5	0.00017
30.0	1061.03	37	18.5	0.00023
35.0	1237.87	46	23.0	0.00029
40.0	1414.71	55	27.5	0.00034
45.0	1591.55	67	33.5	0.00042
50.0	1768.39	76	38.0	0.00048
55.0	1945.23	86	43.0	0.00054
60.0	2122.07	97	48.5	0.00061
65.0	2298.91	113	56.5	0.00071
70.0	2475.75	126	63.0	0.00079
75.0	2652.59	139	69.5	0.00087
80.0	2829.42	154	77.0	0.00096
85.0	3006.26	172	86.0	0.00108
90.0	3183.10	187	93.5	0.00117
95.0	3359.94	213	106.5	0.00133
100.0	3536.78	238	119.0	0.00149
105.0	3713.62	278	139.0	0.00174
106.5	3766.67	FRACTURE		

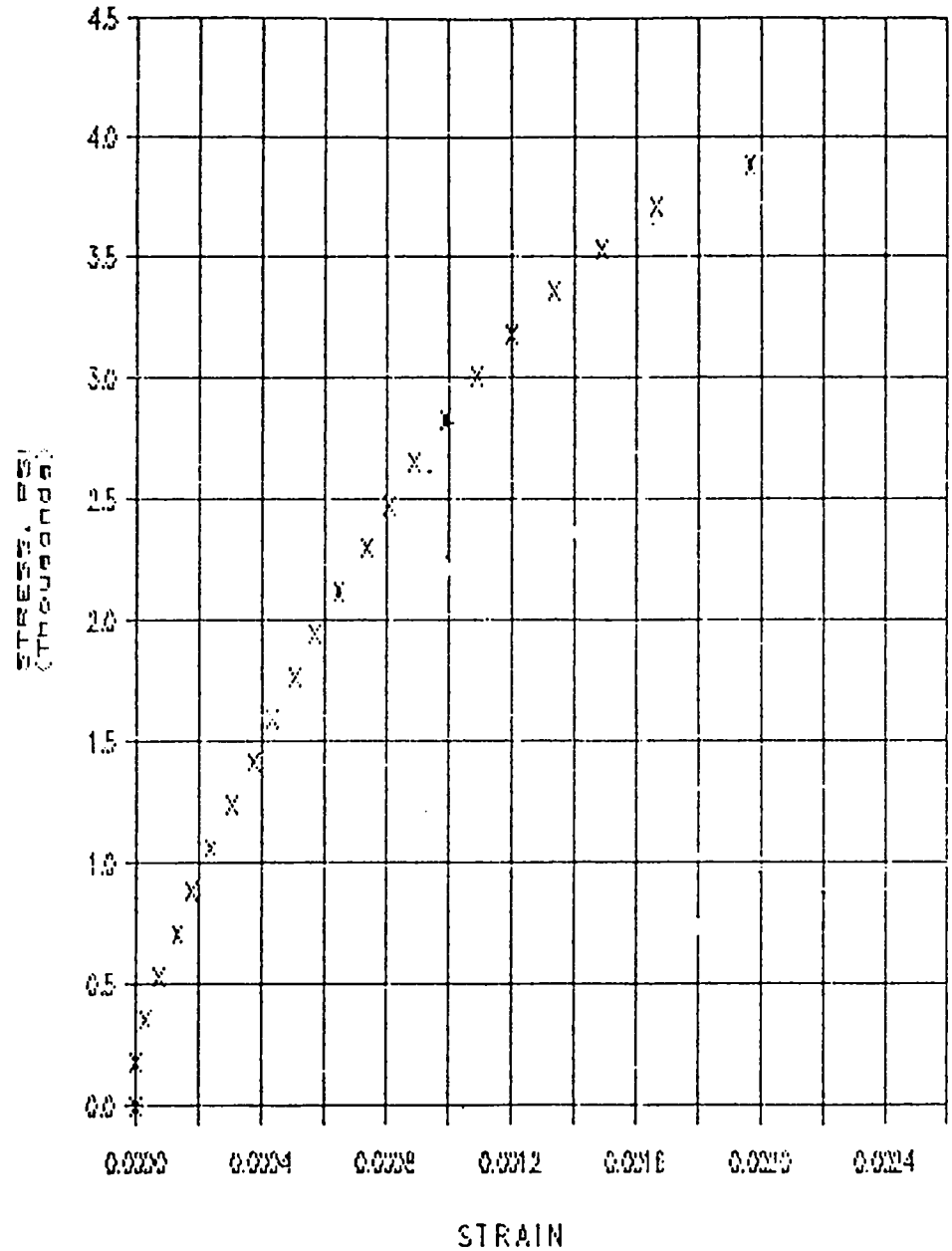


## TEST DATA

MIX 1: SPECIMEN 5

DATE TESTED: 1/26/87

LOAD (LBS) *1000	STRESS (PSI)	READING (IN) *0.0001	DEFORM. (IN) *0.0001	STRAIN
0.0	0.00	0	0.0	0.00000
5.0	176.84	0	0.0	0.00000
10.0	353.65	5	2.5	0.00003
15.0	530.52	11	5.5	0.00007
20.0	707.36	21	10.5	0.00013
25.0	884.20	28	14.0	0.00018
30.0	1061.03	38	19.0	0.00024
35.0	1237.87	49	24.5	0.00031
40.0	1414.71	60	30.0	0.00036
45.0	1591.55	69	34.5	0.00043
50.0	1768.39	81	40.5	0.00051
55.0	1945.23	91	45.5	0.00057
60.0	2122.07	103	51.5	0.00064
65.0	2298.91	118	59.0	0.00074
70.0	2475.75	129	64.5	0.00081
75.0	2652.59	142	71.0	0.00089
80.0	2829.42	158	79.0	0.00099
85.0	3006.26	174	87.0	0.00107
90.0	3183.10	192	96.0	0.00120
95.0	3359.94	214	107.0	0.00134
100.0	3536.78	238	119.0	0.00149
105.0	3713.62	263	133.0	0.00166
110.0	3890.46	314	157.0	0.00196
111.5	3943.51	FRACTURE		

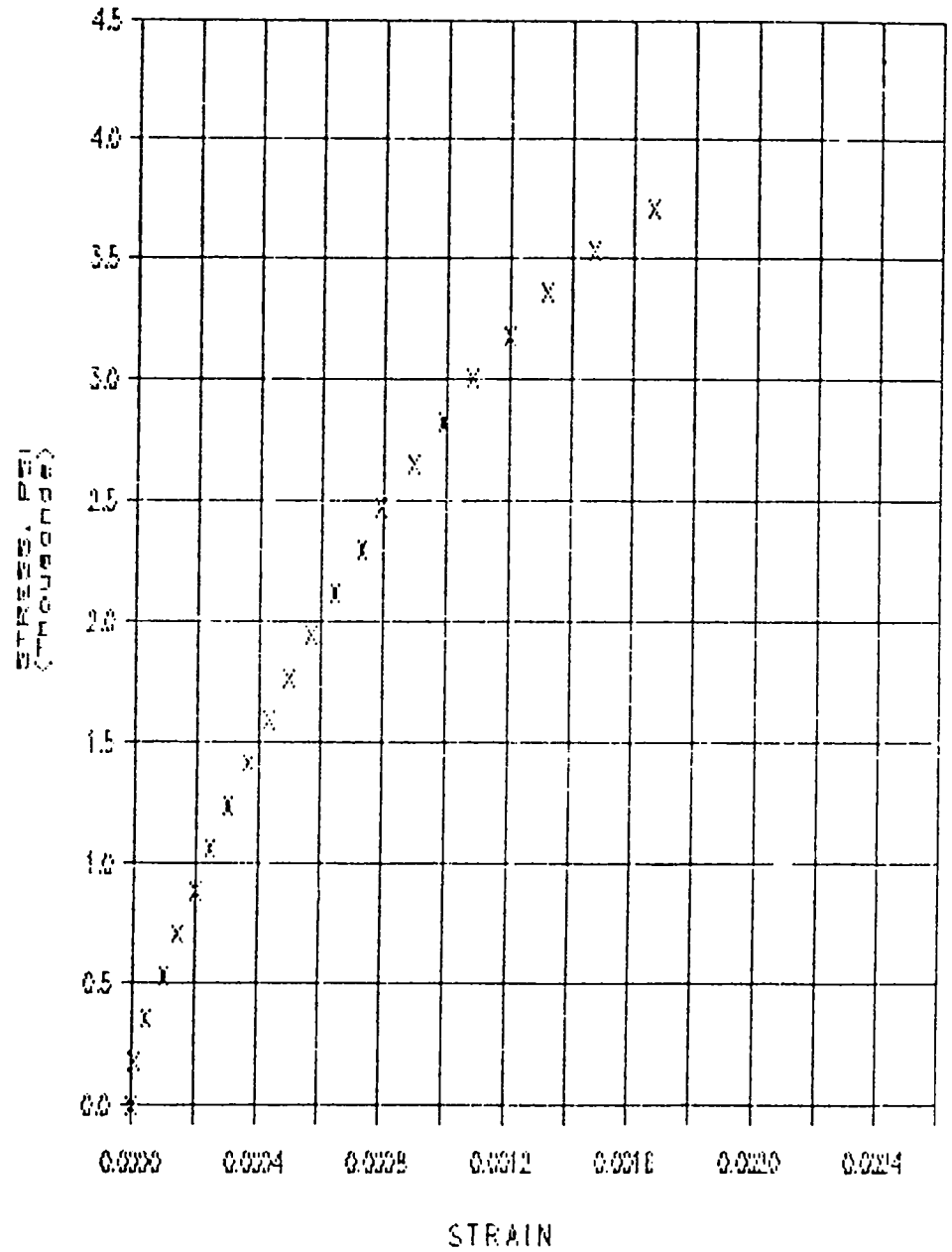


TEST DATA

MIX 1: SPECIMEN 6

DATE TESTED: 1/26/87

LOAD (LBS) *1000	STRESS (PSI)	READING (IN) *0.0001	DEFORM. (IN) *0.0001	STRAIN
0.0	0.00	0	0.0	0.00000
5.0	176.84	1	0.5	0.00001
10.0	353.68	7	3.5	0.00004
15.0	530.52	16	8.0	0.00010
20.0	707.36	23	11.5	0.00014
25.0	884.20	32	16.0	0.00020
30.0	1061.03	39	19.5	0.00024
35.0	1237.87	48	24.0	0.00030
40.0	1414.71	59	29.5	0.00037
45.0	1591.55	69	34.5	0.00043
50.0	1768.39	79	39.5	0.00049
55.0	1945.23	91	45.5	0.00057
60.0	2122.07	103	51.5	0.00064
65.0	2298.91	117	58.5	0.00073
70.0	2475.75	127	63.5	0.00079
75.0	2652.59	143	71.5	0.00089
80.0	2829.42	158	79.0	0.00099
85.0	3006.26	173	86.5	0.00108
90.0	3183.10	192	96.0	0.00120
95.0	3359.94	211	105.5	0.00132
100.0	3536.78	235	117.5	0.00147
105.0	3713.62	266	133.0	0.00166
109.5	3672.77	FRACTURE		



06 TEST DATA

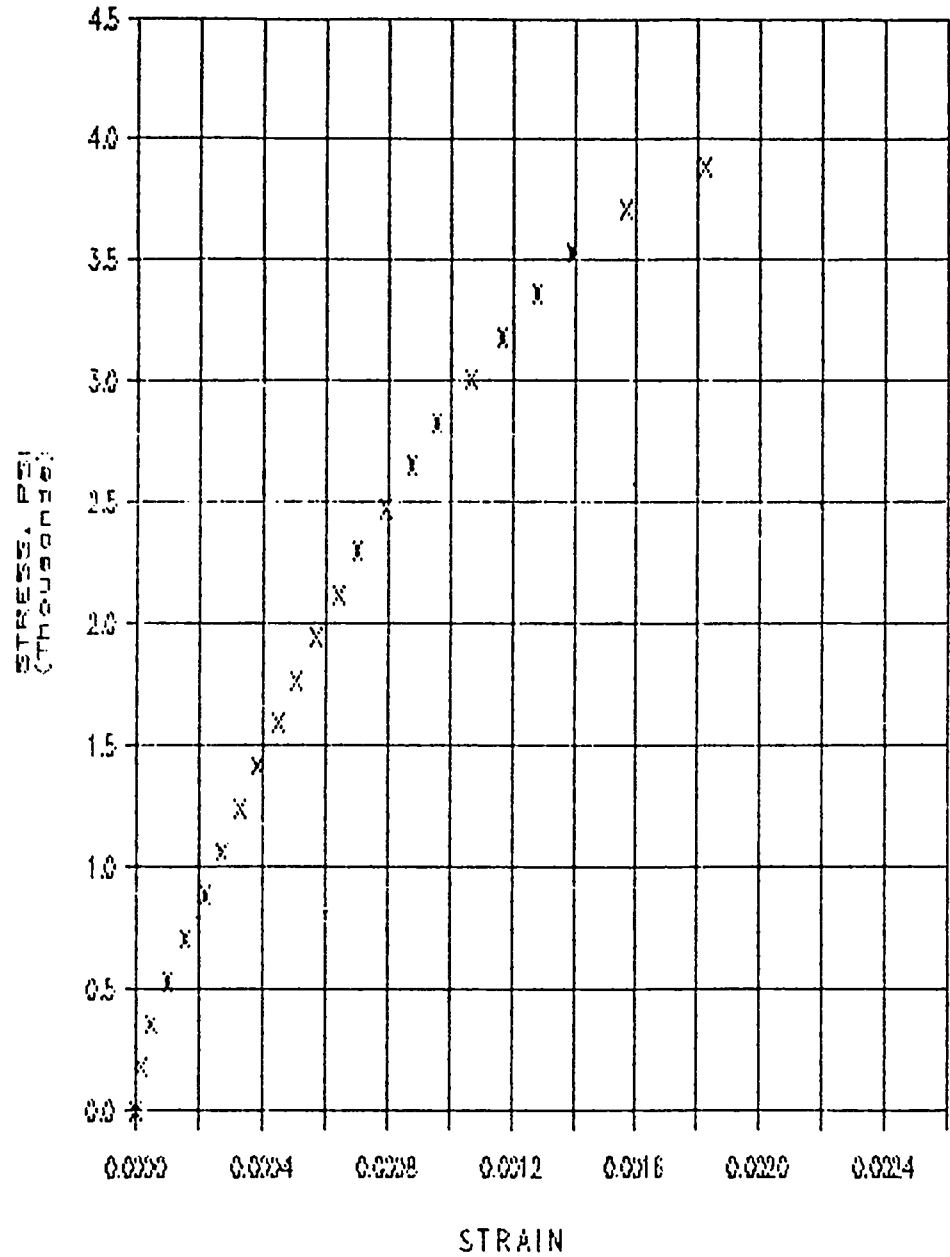
MIX 1; SPECIMEN 7

DATE TESTED: 1/26/87

LOAD (LBS) *1000	STRESS (PSI)	READING (IN) *0.0001	DEFORM. (IN) *0.0001	STRAIN
0.0	0.00	0	0.0	0.00000
5.0	176.84	2	1.0	0.00001
10.0	353.68	8	4.0	0.00005
15.0	530.52	16	8.0	0.00010
20.0	707.36	25	12.5	0.00016
25.0	884.20	35	17.5	0.00022
30.0	1061.03	43	21.5	0.00027
35.0	1237.87	52	26.0	0.00033
40.0	1414.71	61	30.5	0.00038
45.0	1591.55	72	36.0	0.00045
50.0	1768.39	81	40.5	0.00051
55.0	1945.23	91	45.5	0.00057
60.0	2122.07	102	51.0	0.00064
65.0	2298.91	112	56.0	0.00070
70.0	2475.75	127	63.5	0.00079
75.0	2652.59	140	70.0	0.00088
80.0	2829.42	153	76.5	0.00096
85.0	3006.26	170	85.0	0.00106
90.0	3183.10	186	93.0	0.00116
95.0	3359.94	204	102.0	0.00128
100.0	3536.78	222	111.0	0.00139
105.0	3713.62	251	125.5	0.00157
110.0	3890.46	292	146.0	0.00183
112.0	3961.19			

FRACTURE

4

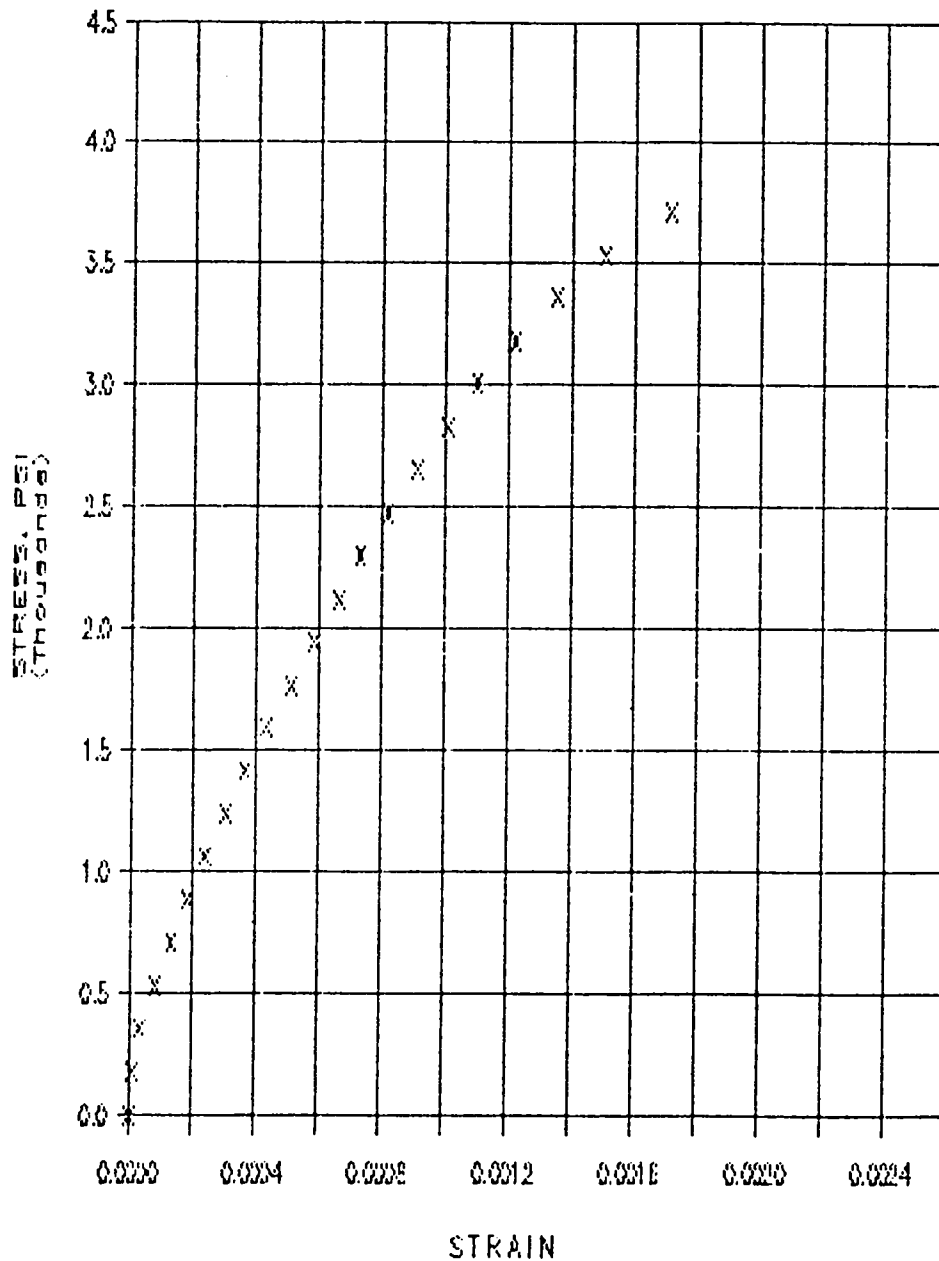


TEST DATA

MIX 1; SPECIMEN B

DATE TESTED: 1/26/87

LOAD (LBS) *1000	STRESS (PSI)	READING (IN) *0.0001	DEFORM. (IN) *0.0001	STRAIN
0.0	0.00	0	0.0	0.00000
5.0	176.84	1	0.5	0.00001
10.0	353.68	5	2.5	0.00003
15.0	530.52	13	6.5	0.00008
20.0	707.36	21	10.5	0.00013
25.0	884.20	29	14.5	0.00018
30.0	1061.03	38	19.0	0.00024
35.0	1237.87	49	24.5	0.00031
40.0	1414.71	59	29.5	0.00037
45.0	1591.55	69	34.5	0.00043
50.0	1768.39	82	41.0	0.00051
55.0	1945.23	93	46.5	0.00058
60.0	2122.07	106	53.0	0.00066
65.0	2298.91	117	58.5	0.00073
70.0	2475.75	131	65.5	0.00082
75.0	2652.59	146	73.0	0.00091
80.0	2829.42	161	80.5	0.00101
85.0	3006.26	176	88.0	0.00110
90.0	3183.10	195	97.5	0.00122
95.0	3359.94	216	108.0	0.00135
100.0	3536.78	241	120.5	0.00151
105.0	3713.62	274	137.0	0.00171
109.5	3872.77	FRACTURE		

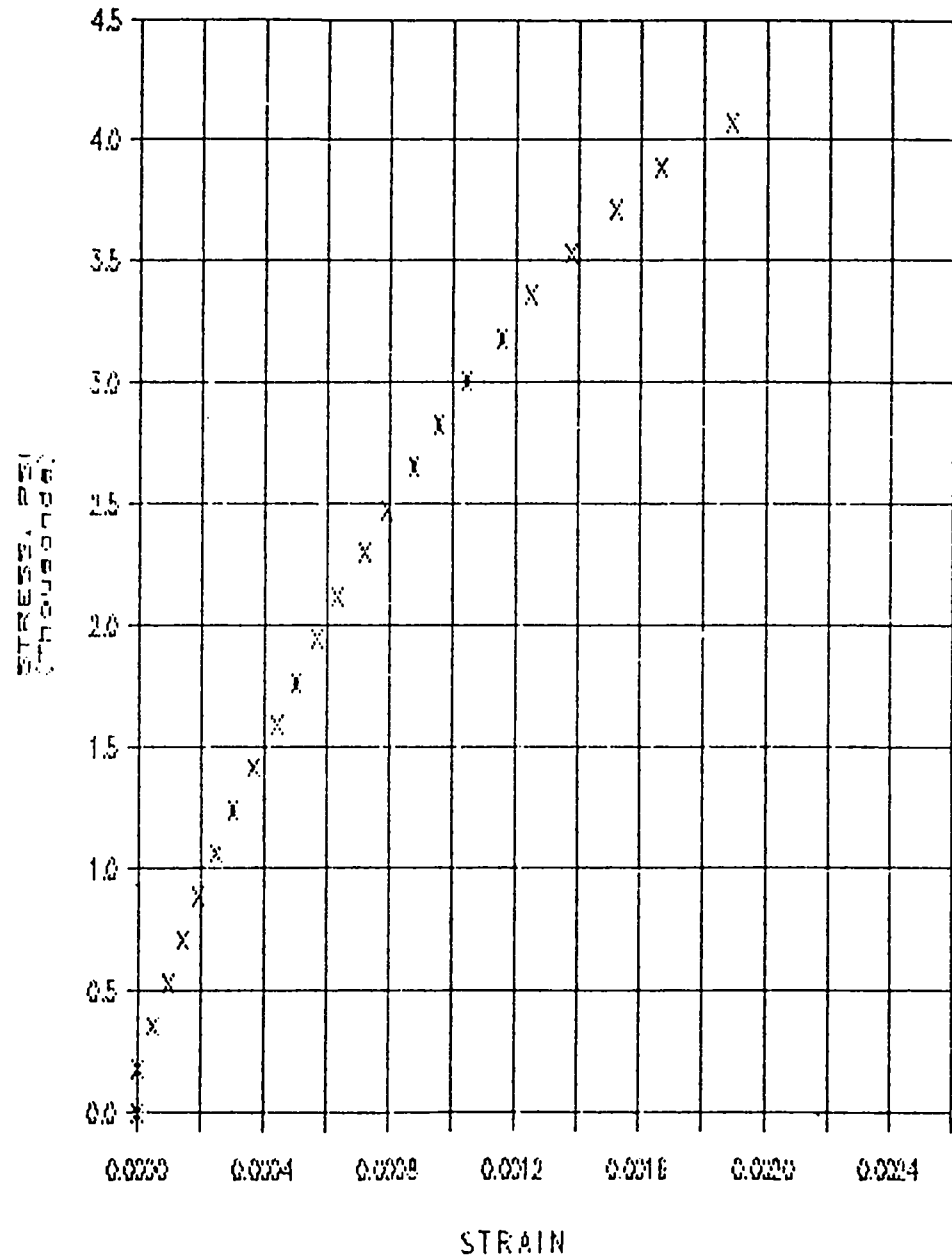


## TEST DATA

MIX 1; SPECIMEN 9

DATE TESTED: 1/26/87

LOAD (LBS) *1000	STRESS (PSI)	READING (IN) *0.0001	DEFORM. (IN) *0.0001	STRAIN
0.0	0.00	0	0.0	0.00000
5.0	176.84	0	0.0	0.00000
10.0	353.68	8	4.0	0.00005
15.0	530.52	15	7.5	0.00009
20.0	707.36	23	11.5	0.00014
25.0	884.20	31	15.5	0.00019
30.0	1061.03	40	20.0	0.00025
35.0	1237.87	48	24.0	0.00030
40.0	1414.71	59	29.5	0.00037
45.0	1591.55	70	35.0	0.00044
50.0	1768.39	80	40.0	0.00050
55.0	1945.23	91	45.5	0.00057
60.0	2122.07	101	50.5	0.00063
65.0	2298.91	115	57.5	0.00072
70.0	2475.75	127	63.5	0.00079
75.0	2652.59	140	70.0	0.00088
80.0	2829.42	153	76.5	0.00096
85.0	3006.26	167	83.5	0.00104
90.0	3183.10	185	92.5	0.00114
95.0	3359.94	200	100.0	0.00125
100.0	3536.78	220	110.0	0.00138
105.0	3713.62	243	121.5	0.00152
110.0	3890.46	266	133.0	0.00166
115.0	4067.30	302	151.0	0.00189
118.0	4173.40	FRACTURE		



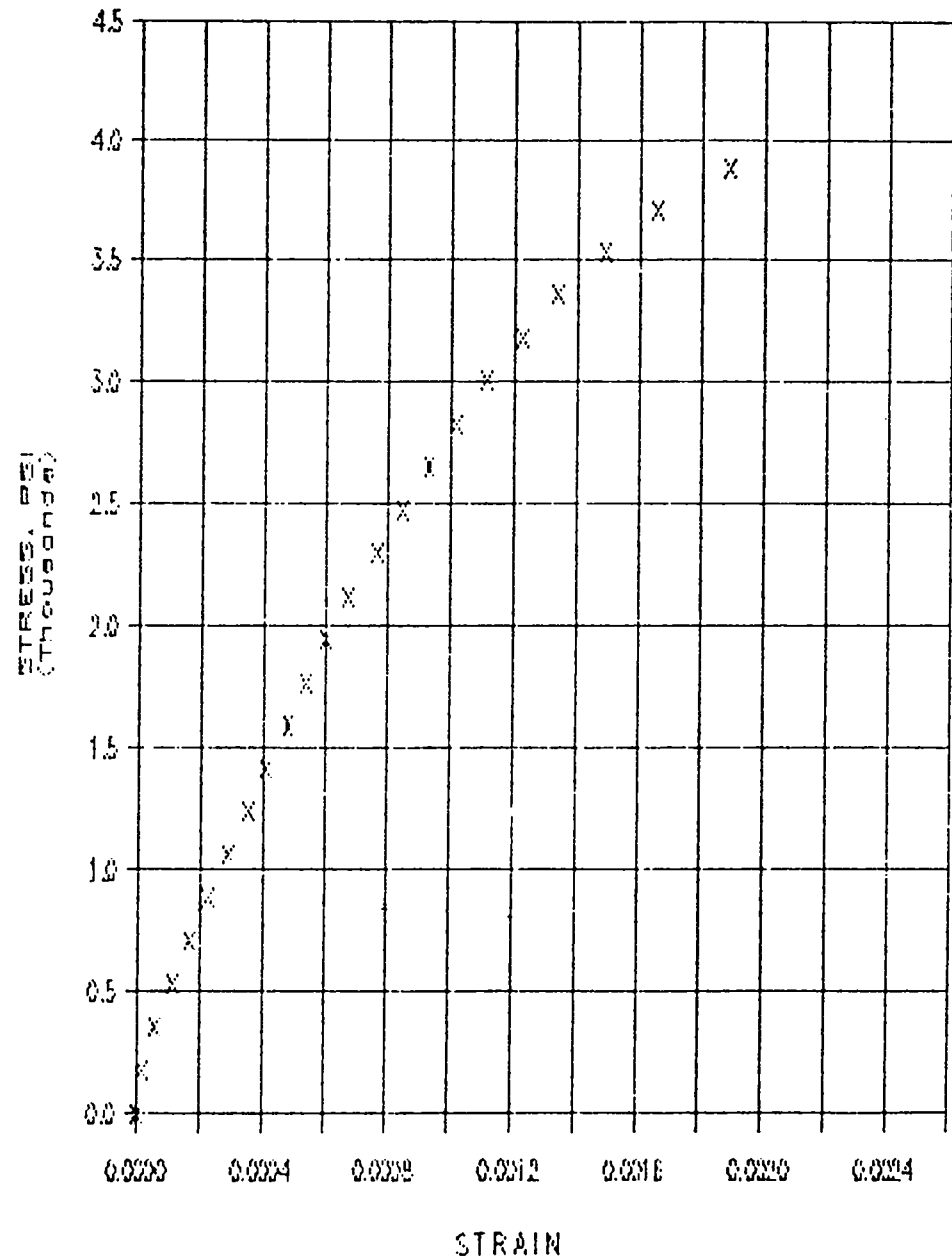


TEST DATA

MIX 1; SPECIMEN 10

DATE TESTED: 1/26/87

LOAD (LBS) *1000	STRESS (PSI)	READING (IN) *0.0001	DEFORM. (IN) *0.0001	STRAIN
0.0	0.00	0	0.0	0.00000
5.0	176.84	2	1.0	0.00001
10.0	353.68	9	4.5	0.00006
15.0	530.52	18	9.0	0.00011
20.0	707.36	27	13.5	0.00017
25.0	884.20	36	18.0	0.00023
30.0	1061.03	46	23.0	0.00029
35.0	1237.87	56	28.0	0.00035
40.0	1414.71	65	32.5	0.00041
45.0	1591.55	76	38.0	0.00048
50.0	1768.39	86	43.0	0.00054
55.0	1945.23	96	48.0	0.00060
60.0	2122.07	107	53.5	0.00067
65.0	2298.91	123	61.5	0.00077
70.0	2475.75	136	68.0	0.00085
75.0	2652.59	149	74.5	0.00093
80.0	2829.42	162	81.0	0.00101
85.0	3006.26	178	89.0	0.00111
90.0	3183.10	196	98.0	0.00123
95.0	3359.94	214	107.0	0.00134
100.0	3536.78	236	119.0	0.00149
105.0	3713.62	265	132.5	0.00166
110.0	3890.46	302	151.0	0.00189
114.5	4049.61	FRACTURE		



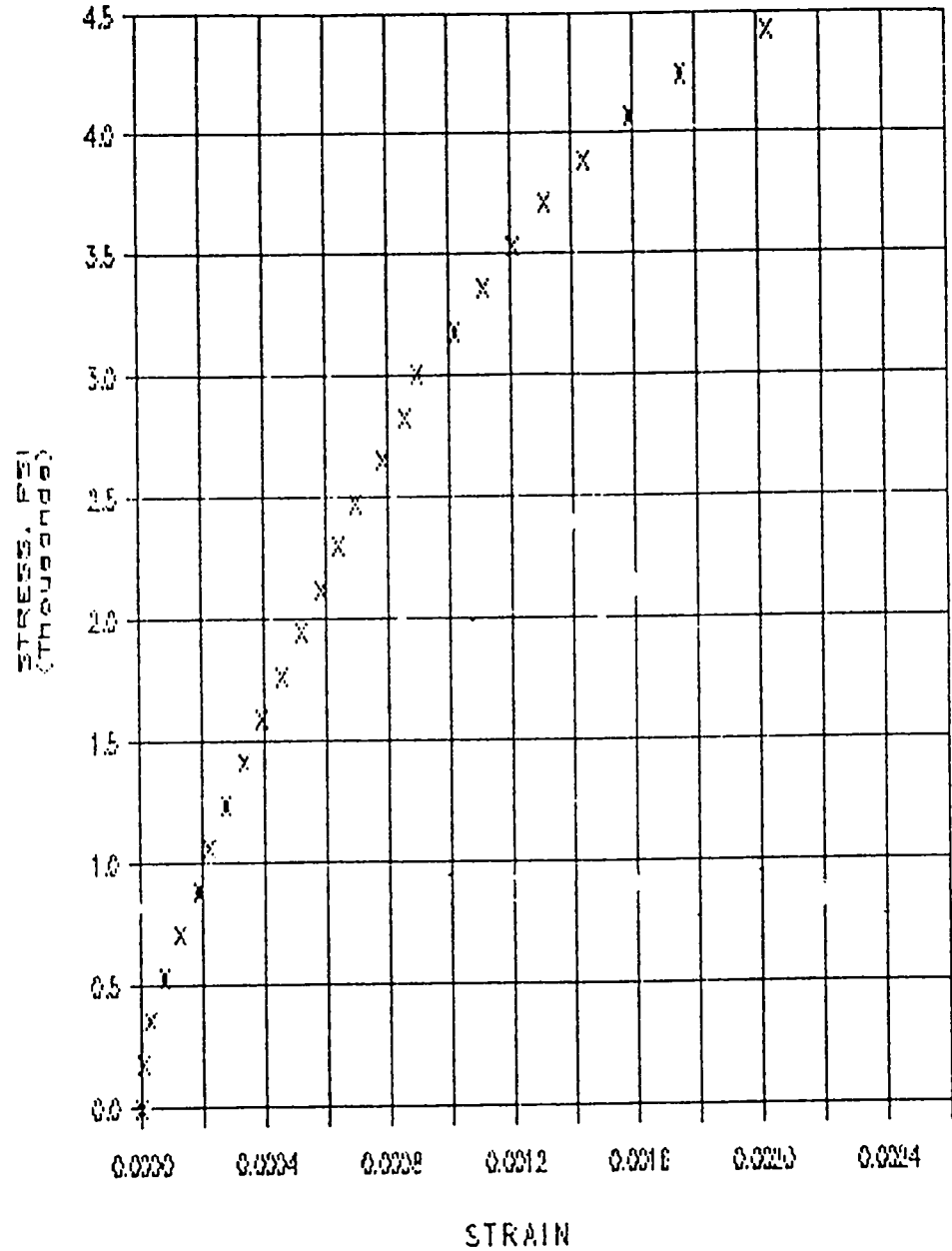
## TEST DATA

MIX 2; SPECIMEN 1

DATE TESTED: 1/23/87

LOAD (LBS) *1000	STRESS (PSI)	READING (IN) *0.0001	DEFORM. (IN) *0.0001	STRAIN
0.0	0.00	0	0.0	0.00000
5.0	176.84	1	0.5	0.00001
10.0	353.68	5	2.5	0.00003
15.0	530.52	12	6.0	0.00008
20.0	707.36	20	10.0	0.00013
25.0	884.20	30	15.0	0.00019
30.0	1061.03	36	18.0	0.00023
35.0	1237.87	44	22.0	0.00028
40.0	1414.71	54	27.0	0.00034
45.0	1591.55	63	31.5	0.00039
50.0	1768.39	73	36.5	0.00046
55.0	1945.23	83	41.5	0.00052
60.0	2122.07	93	46.5	0.00058
65.0	2298.91	102	51.0	0.00064
70.0	2475.75	111	55.5	0.00069
75.0	2652.59	125	62.5	0.00078
80.0	2829.42	137	68.0	0.00086
85.0	3006.26	143	71.5	0.00089
90.0	3183.10	163	81.5	0.00102
95.0	3359.94	178	89.0	0.00111
100.0	3536.78	193	96.5	0.00121
105.0	3713.62	210	105.0	0.00131
110.0	3890.46	230	115.0	0.00144
115.0	4067.30	254	127.0	0.00159
120.0	4244.14	281	140.5	0.00176
125.0	4420.98	325	162.5	0.00203
127.0	4491.71			

FRACTURE



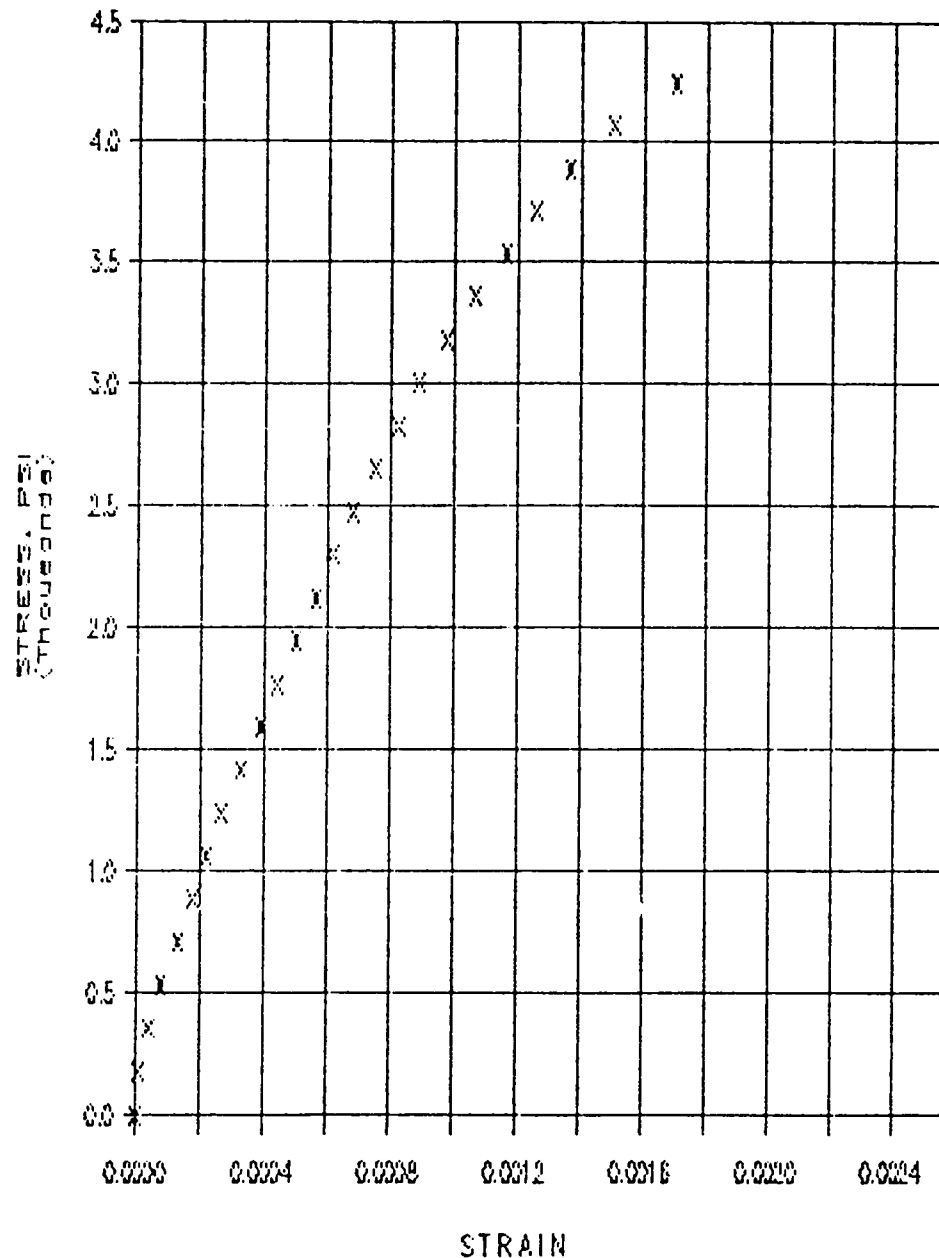
TEST DATA

MIX 2; SPECIMEN 2

DATE TESTED: 1/23/87

LOAD (LBS) *1000	STRESS (PSI)	READING (IN) *0.0001	DEFORM. (IN) *0.0001	STRAIN
0.0	0.00	0	0.0	0.00000
5.0	176.84	1	0.5	0.00001
10.0	353.68	6	3.0	0.00004
15.0	530.52	12	6.0	0.00008
20.0	707.36	21	10.5	0.00013
25.0	884.20	28	14.0	0.00018
30.0	1061.03	35	17.5	0.00022
35.0	1237.87	42	21.0	0.00026
40.0	1414.71	52	28.0	0.00033
45.0	1591.55	62	31.0	0.00039
50.0	1768.39	70	35.0	0.00044
55.0	1945.23	80	40.0	0.00050
60.0	2122.07	90	45.0	0.00056
65.0	2298.91	98	49.0	0.00061
70.0	2475.75	109	54.5	0.00068
75.0	2652.59	120	60.0	0.00075
80.0	2829.42	132	66.0	0.00083
85.0	3006.26	142	71.0	0.00089
90.0	3183.10	156	78.0	0.00098
95.0	3359.94	170	85.0	0.00106
100.0	3536.78	186	93.0	0.00116
105.0	3713.62	201	100.5	0.00126
110.0	3890.46	218	109.0	0.00136
115.0	4067.30	241	120.5	0.00151
120.0	4244.14	272	136.0	0.00170
122.5	4332.56			

FRACTURE

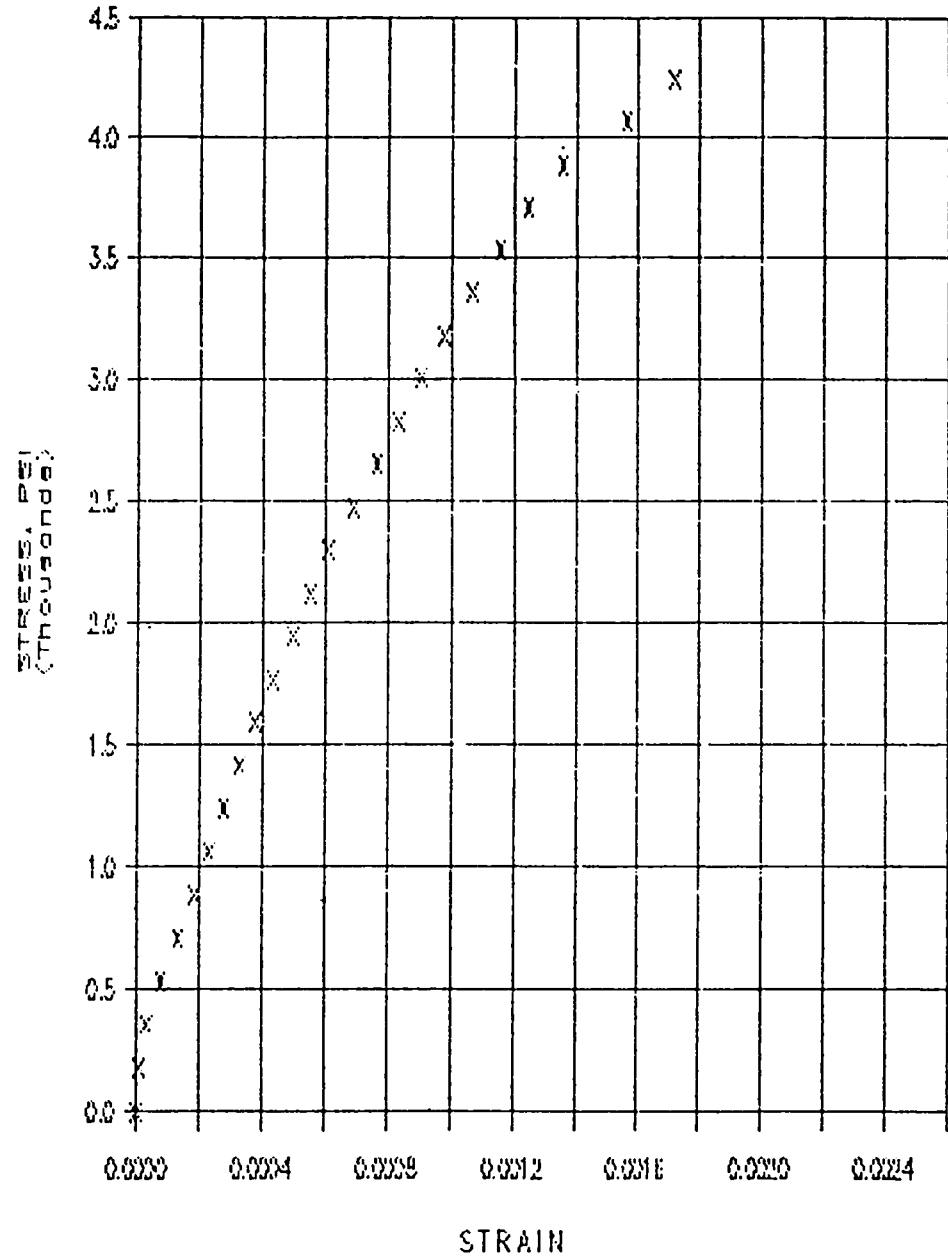


## TEST DATA

MIX 2: SPECIMEN 3

DATE TESTED: 1/23/87

LOAD (LBS) *1000	STRESS (PSI)	READING (IN) *0.0001	DEFORM. (IN) *0.0001	STRAIN
0.0	0.00	0	0.0	0.00000
5.0	176.84	1	0.5	0.00001
10.0	353.68	5	2.5	0.00003
15.0	530.52	12	6.0	0.00006
20.0	707.36	21	10.5	0.00013
25.0	884.20	29	14.5	0.00018
30.0	1061.03	37	18.5	0.00023
35.0	1237.87	44	22.0	0.00028
40.0	1414.71	52	26.0	0.00033
45.0	1591.55	60	30.0	0.00038
50.0	1768.39	69	34.5	0.00043
55.0	1945.23	79	39.5	0.00049
60.0	2122.07	88	44.0	0.00055
65.0	2298.91	97	48.5	0.00061
70.0	2475.75	110	55.0	0.00069
75.0	2652.59	122	61.0	0.00076
80.0	2829.42	133	66.5	0.00083
85.0	3006.26	145	72.5	0.00091
90.0	3183.10	156	78.0	0.00098
95.0	3359.94	170	85.0	0.00106
100.0	3536.78	185	92.5	0.00116
105.0	3713.62	199	99.5	0.00124
110.0	3890.46	217	108.5	0.00136
115.0	4067.30	250	125.0	0.00156
120.0	4244.14	275	137.5	0.00172
121.5	4297.19	FRACTURE		

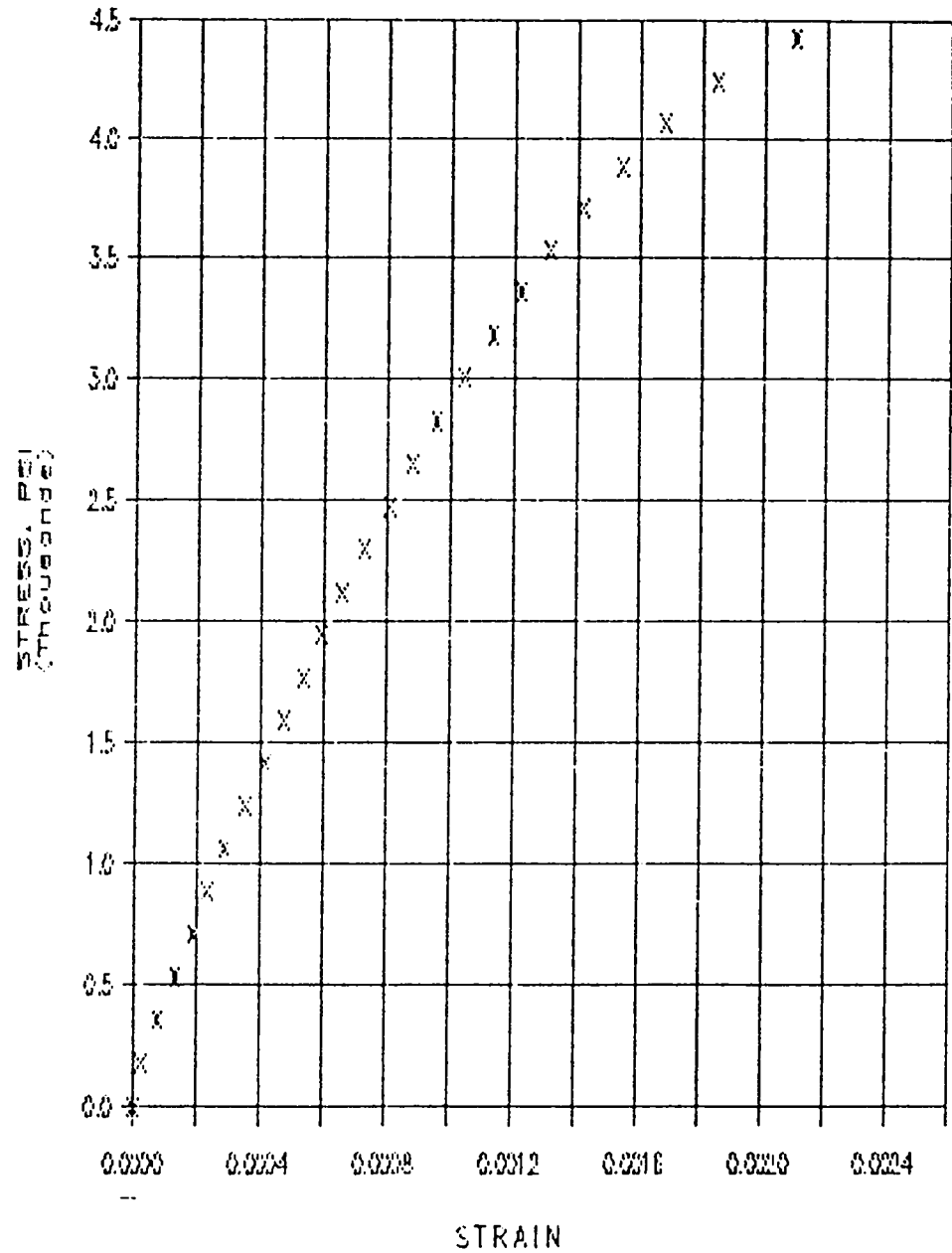


TEST DATA

MIX 2: SPECIMEN 4

DATE TESTED: 1/23/87

LOAD (LBS) *1000	STRESS (PSI)	READING (IN) *0.0001	DEFORM. (IN) *0.0001	STRAIN
0.0	0.00	0	0.0	0.00000
5.0	176.84	4	2.0	0.00003
10.0	353.68	12	6.0	0.00006
15.0	530.52	21	10.5	0.00013
20.0	707.36	30	15.0	0.00019
25.0	884.20	37	18.5	0.00023
30.0	1061.03	46	23.0	0.00029
35.0	1237.87	56	28.0	0.00035
40.0	1414.71	66	33.0	0.00041
45.0	1591.55	75	37.5	0.00047
50.0	1768.39	86	43.0	0.00054
55.0	1945.23	95	47.5	0.00059
60.0	2122.07	105	52.5	0.00066
65.0	2298.91	116	58.0	0.00073
70.0	2475.75	129	64.5	0.00081
75.0	2652.59	141	70.5	0.00088
80.0	2829.42	153	76.5	0.00096
85.0	3006.26	166	83.0	0.00104
90.0	3183.10	181	90.5	0.00113
95.0	3359.94	195	97.5	0.00122
100.0	3536.78	210	105.0	0.00131
105.0	3713.62	226	113.0	0.00141
110.0	3890.46	247	123.5	0.00154
115.0	4067.30	269	134.5	0.00168
120.0	4244.14	296	148.0	0.00185
125.0	4420.98	336	168.0	0.00210
127.5	4509.40	FRACTURE		



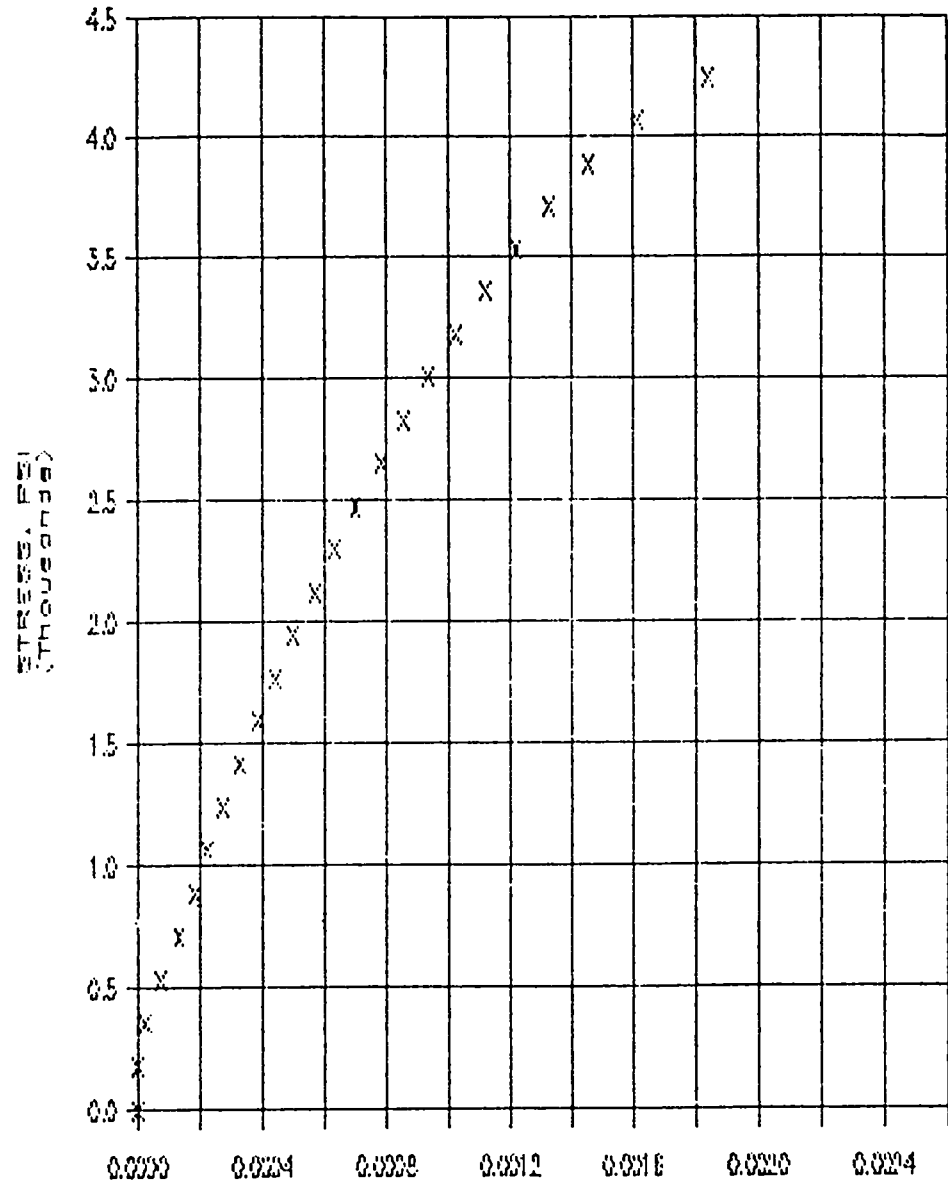
## TEST DATA

MIX 2: SPECIMEN 5

DATE TESTED: 1/23/87

LOAD (LBS) *1000	STRESS (PSI)	READING (IN) *0.0001	DEFORM. (IN) *0.0001	STRAIN
0.0	0.00	0	0.0	0.00000
5.0	176.84	0	0.0	0.00000
10.0	353.68	4	2.0	0.00003
15.0	530.52	11	5.5	0.00007
20.0	707.36	21	10.5	0.00010
25.0	884.20	29	14.5	0.00018
30.0	1061.03	36	18.0	0.00023
35.0	1237.87	43	21.5	0.00027
40.0	1414.71	52	26.0	0.00030
45.0	1591.55	61	30.5	0.00038
50.0	1768.39	70	35.0	0.00044
55.0	1945.23	79	39.5	0.00049
60.0	2122.07	91	45.5	0.00057
65.0	2298.91	101	50.5	0.00063
70.0	2475.75	112	56.0	0.00070
75.0	2652.59	125	62.5	0.00076
80.0	2829.42	137	68.5	0.00086
85.0	3006.26	150	75.0	0.00094
90.0	3183.10	164	82.0	0.00103
95.0	3359.94	179	89.5	0.00112
100.0	3536.78	195	97.5	0.00122
105.0	3713.62	212	106.0	0.00133
110.0	3890.46	233	116.5	0.00146
115.0	4067.30	258	129.0	0.00161
120.0	4244.14	294	147.0	0.00184
123.5	4367.92			

FRACTURE

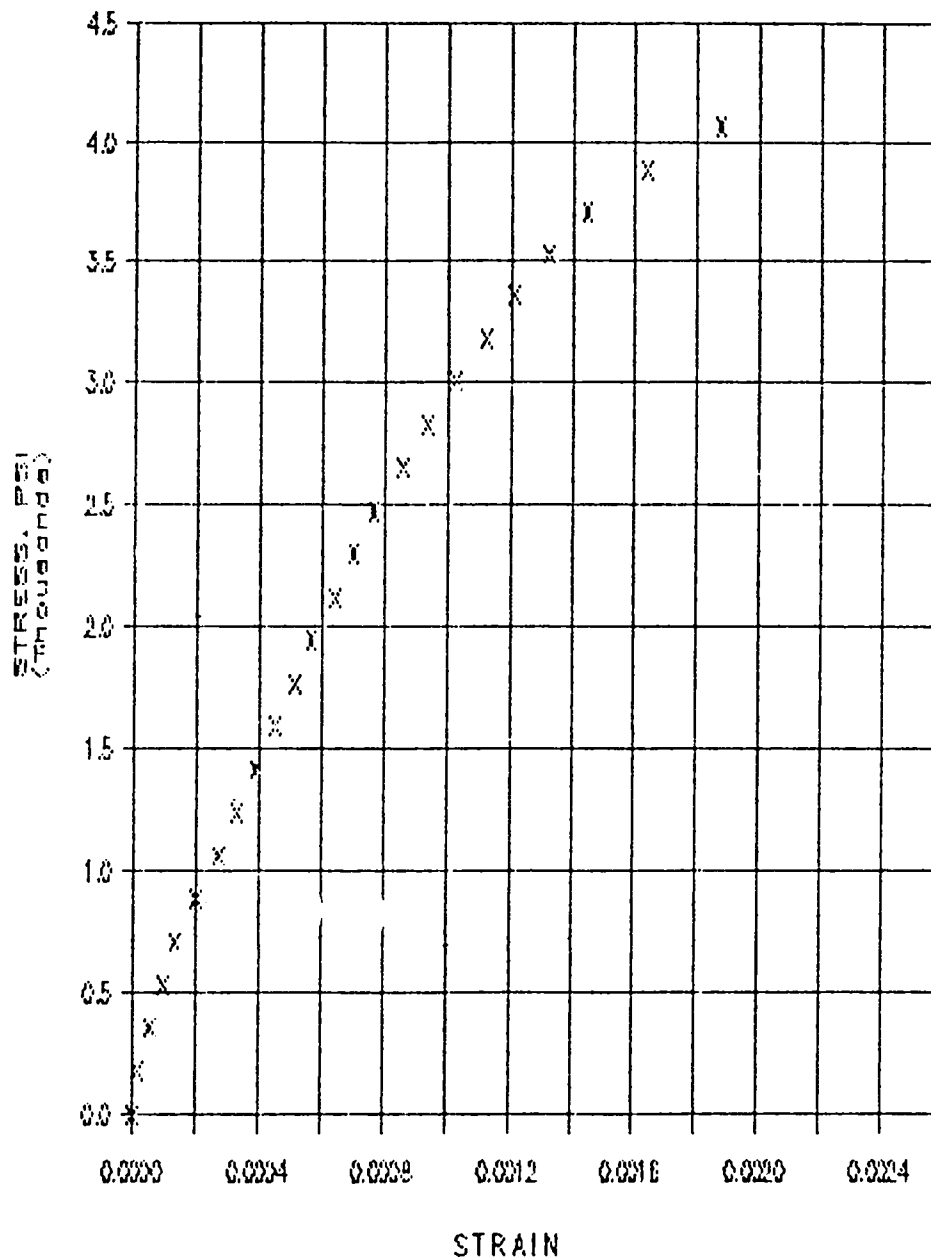


TEST DATA

MIX 2: SPECIMEN 6

DATE TESTED: 1/23/87

LOAD (LBS) *1000	STRESS (PSI)	READING (IN) *0.0001	DEFORM. (IN) *0.0001	STRAIN
0.0	0.00	0	0.0	0.00000
5.0	176.84	2	1.0	0.00001
10.0	353.68	9	4.5	0.00006
15.0	530.52	15	7.5	0.00009
20.0	707.36	22	11.0	0.00014
25.0	884.20	32	16.0	0.00020
30.0	1061.03	43	21.5	0.00027
35.0	1237.87	52	26.0	0.00033
40.0	1414.71	62	31.0	0.00039
45.0	1591.55	72	36.0	0.00045
50.0	1768.39	82	41.0	0.00051
55.0	1945.23	90	45.0	0.00056
60.0	2122.07	102	51.0	0.00064
65.0	2298.91	112	56.0	0.00070
70.0	2475.75	122	61.0	0.00076
75.0	2652.59	137	66.5	0.00086
80.0	2829.42	150	75.0	0.00094
85.0	3006.26	164	82.0	0.00103
90.0	3183.10	179	89.0	0.00112
95.0	3359.94	193	96.5	0.00121
100.0	3536.78	211	105.5	0.00132
105.0	3713.62	231	115.5	0.00144
110.0	3890.46	262	131.0	0.00164
115.0	4067.30	300	150.0	0.00188
117.0	4138.03	FRACTURE		



100

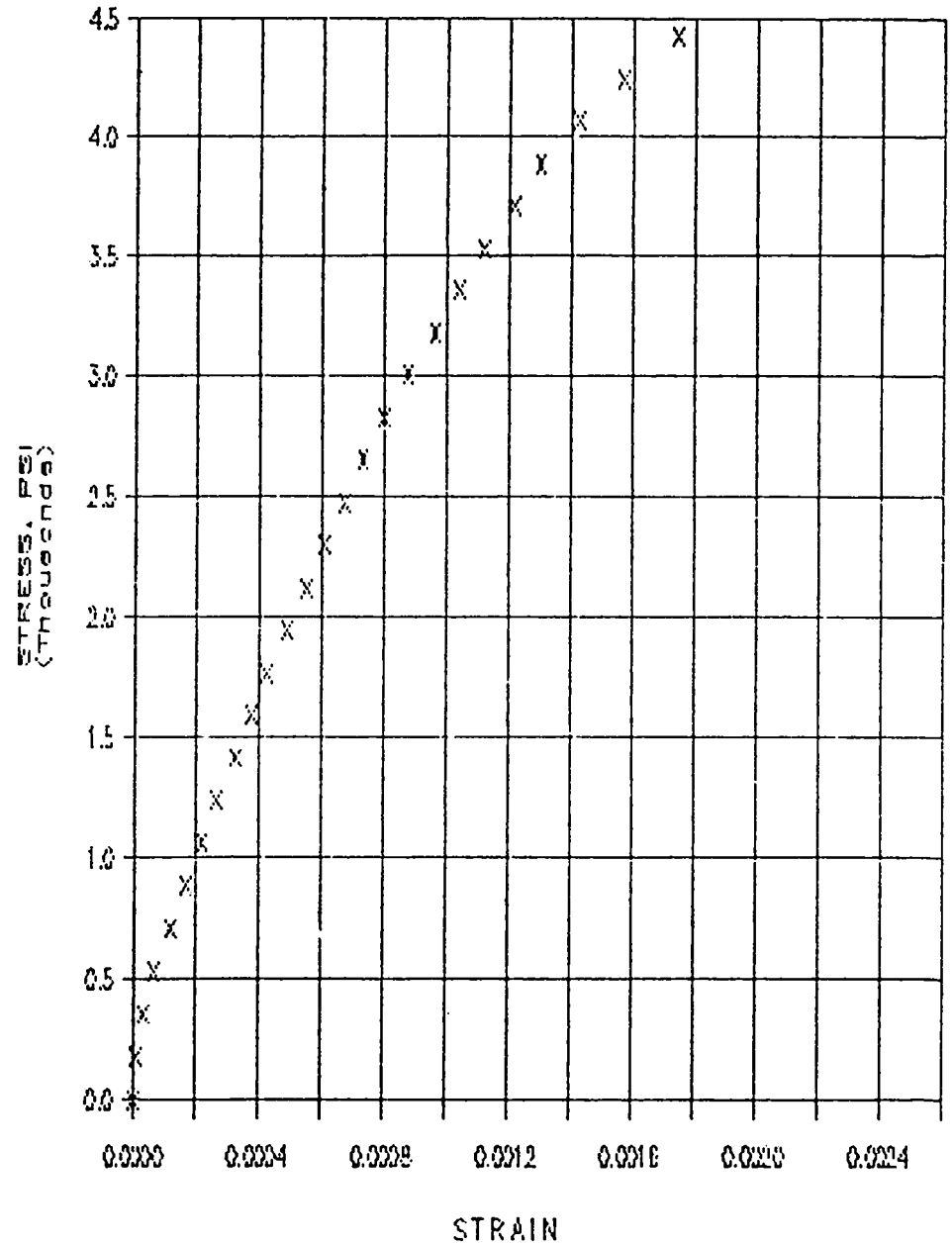
## TEST DATA

MIX 2; SPECIMEN 7

DATE TESTED: 1/23/87

LOAD (LBS) *1000	STRESS (PSI)	READING (IN) *0.0001	DEFORM. (IN) *0.0001	STRAIN
0.0	0.00	0	0.0	0.00000
5.0	176.84	1	0.5	0.00001
10.0	353.68	5	2.5	0.00003
15.0	530.52	10	5.0	0.00006
20.0	707.36	19	9.5	0.00012
25.0	884.20	27	13.5	0.00017
30.0	1061.03	35	17.5	0.00022
35.0	1237.87	42	21.0	0.00026
40.0	1414.71	52	26.0	0.00033
45.0	1591.55	60	30.0	0.00038
50.0	1768.39	68	34.0	0.00043
55.0	1945.23	78	39.0	0.00049
60.0	2122.07	88	44.0	0.00055
65.0	2298.91	97	48.5	0.00061
70.0	2475.75	107	53.5	0.00067
75.0	2652.59	117	58.5	0.00073
80.0	2829.42	128	64.0	0.00080
85.0	3006.26	140	70.0	0.00088
90.0	3183.10	154	77.0	0.00096
95.0	3359.94	166	83.0	0.00104
100.0	3536.78	179	89.5	0.00112
105.0	3713.62	194	97.0	0.00121
110.0	3890.46	208	104.0	0.00130
115.0	4067.30	228	114.0	0.00143
120.0	4244.14	251	125.5	0.00157
125.0	4420.98	279	139.5	0.00174
129.0	4562.45			

FRACTURE



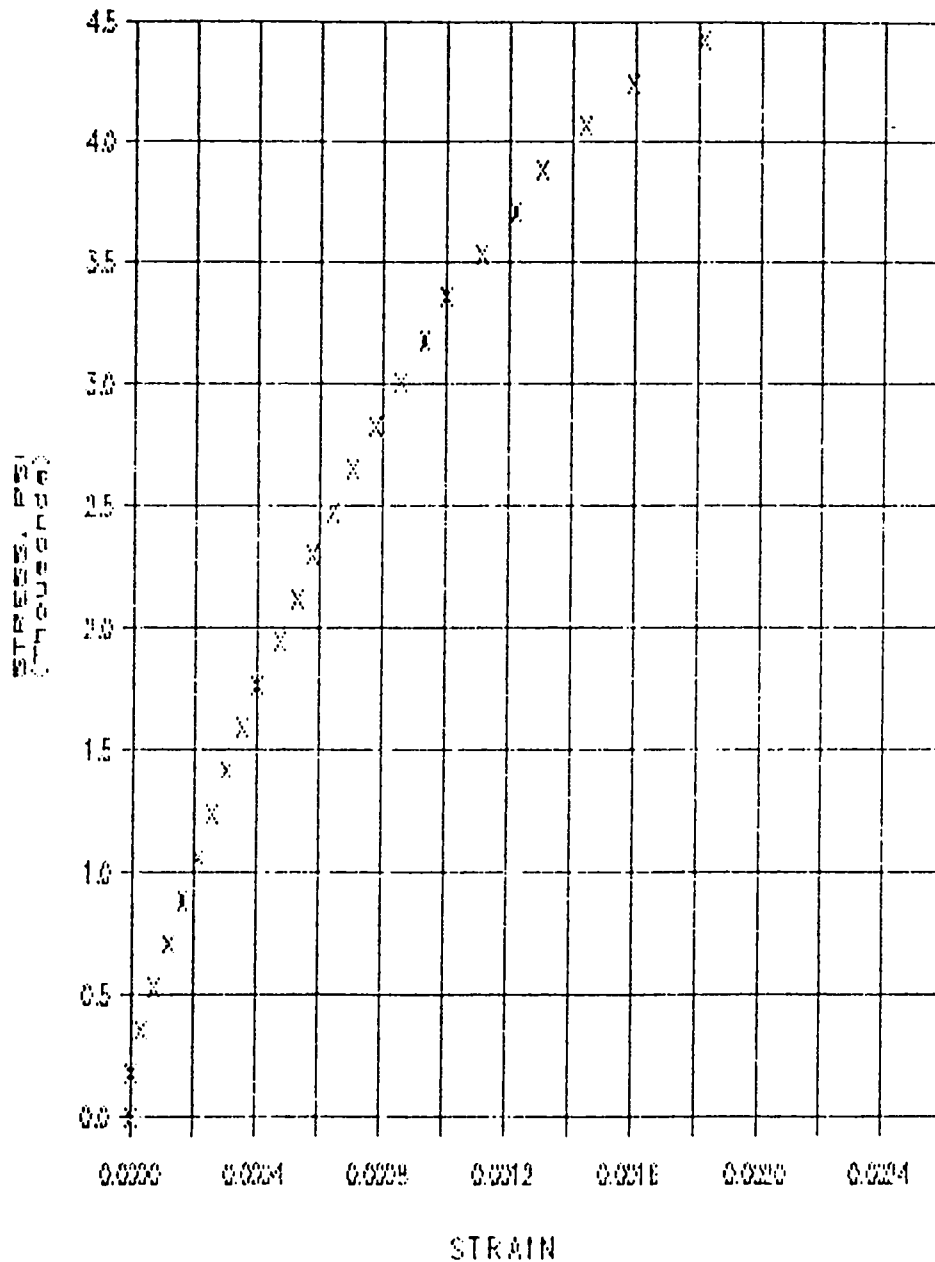


TEST DATA

MIX 2; SPECIMEN 8

DATE TESTED: 1/26/87

LOAD (LBS) *1000	STRESS (PSI)	READING (IN) *0.0001	DEFORM. (IN) *0.0001	STRAIN
0.0	0.00	0	0.0	0.00000
5.0	176.84	0	0.0	0.00000
10.0	353.68	5	2.5	0.00003
15.0	530.52	11	5.5	0.00007
20.0	707.36	19	9.5	0.00012
25.0	884.20	26	13.0	0.00016
30.0	1061.03	34	17.0	0.00021
35.0	1237.87	41	20.5	0.00026
40.0	1414.71	49	24.5	0.00031
45.0	1591.55	56	28.0	0.00035
50.0	1768.39	64	32.0	0.00040
55.0	1945.23	75	37.5	0.00047
60.0	2122.07	84	42.0	0.00053
65.0	2298.91	92	46.0	0.00058
70.0	2475.75	102	51.0	0.00064
75.0	2652.59	113	56.5	0.00071
80.0	2829.42	124	62.0	0.00078
85.0	3006.26	137	68.5	0.00086
90.0	3183.10	149	74.5	0.00093
95.0	3359.94	160	80.0	0.00100
100.0	3536.78	178	89.0	0.00111
105.0	3713.62	195	97.5	0.00122
110.0	3890.46	209	104.5	0.00131
115.0	4067.30	230	115.0	0.00144
120.0	4244.14	255	127.5	0.00159
125.0	4420.98	290	145.0	0.00181
129.0	4562.45	FRACTURE		



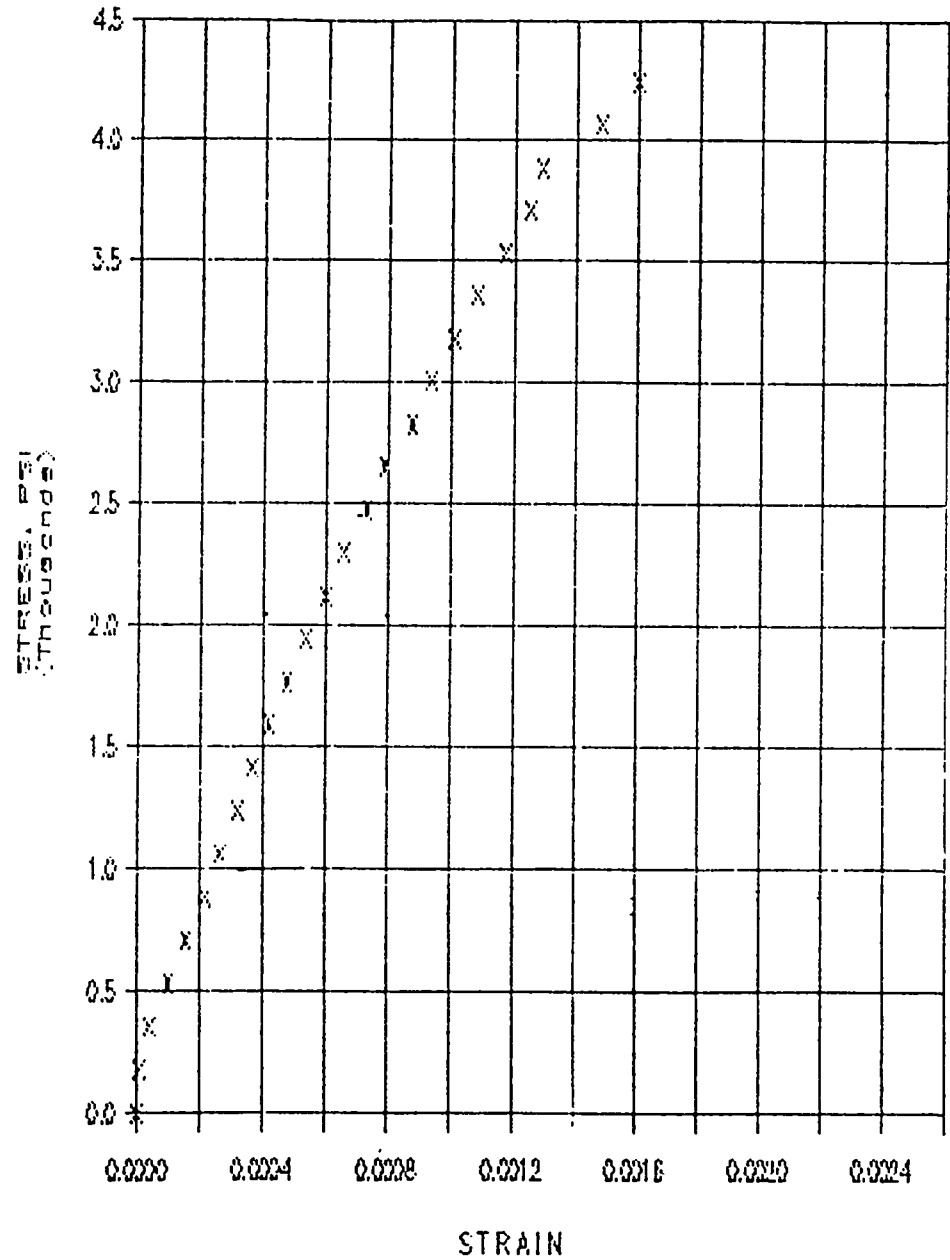
## TEST DATA

MIX 2: SPECIMEN 9

DATE TESTED: 1/26/67

LOAD (LBS) *1000	STRESS (PSI)	READING (IN) *0.0001	DEFORM. (IN) *0.0001	STRAIN
0.0	0.00	0	0.0	0.00000
5.0	176.84	1	0.5	0.00001
10.0	353.68	6	3.0	0.00004
15.0	530.52	16	8.0	0.00010
20.0	707.36	25	12.5	0.00016
25.0	884.20	34	17.0	0.00021
30.0	1061.00	42	21.0	0.00026
35.0	1237.87	51	25.5	0.00032
40.0	1414.71	59	29.5	0.00037
45.0	1591.55	67	33.5	0.00042
50.0	1768.39	76	38.0	0.00048
55.0	1945.23	86	43.0	0.00054
60.0	2122.07	96	48.0	0.00060
65.0	2298.91	105	52.5	0.00066
70.0	2475.75	117	58.5	0.00072
75.0	2652.59	126	63.0	0.00079
80.0	2829.42	140	70.0	0.00088
85.0	3006.26	150	75.0	0.00094
90.0	3183.10	161	80.5	0.00101
95.0	3359.94	173	86.5	0.00108
100.0	3536.78	187	93.5	0.00117
105.0	3713.62	200	100.0	0.00125
110.0	3890.48	206	103.0	0.00129
115.0	4067.30	237	118.5	0.00148
120.0	4244.14	256	128.0	0.00160
126.0	4456.34			

FRACTURE

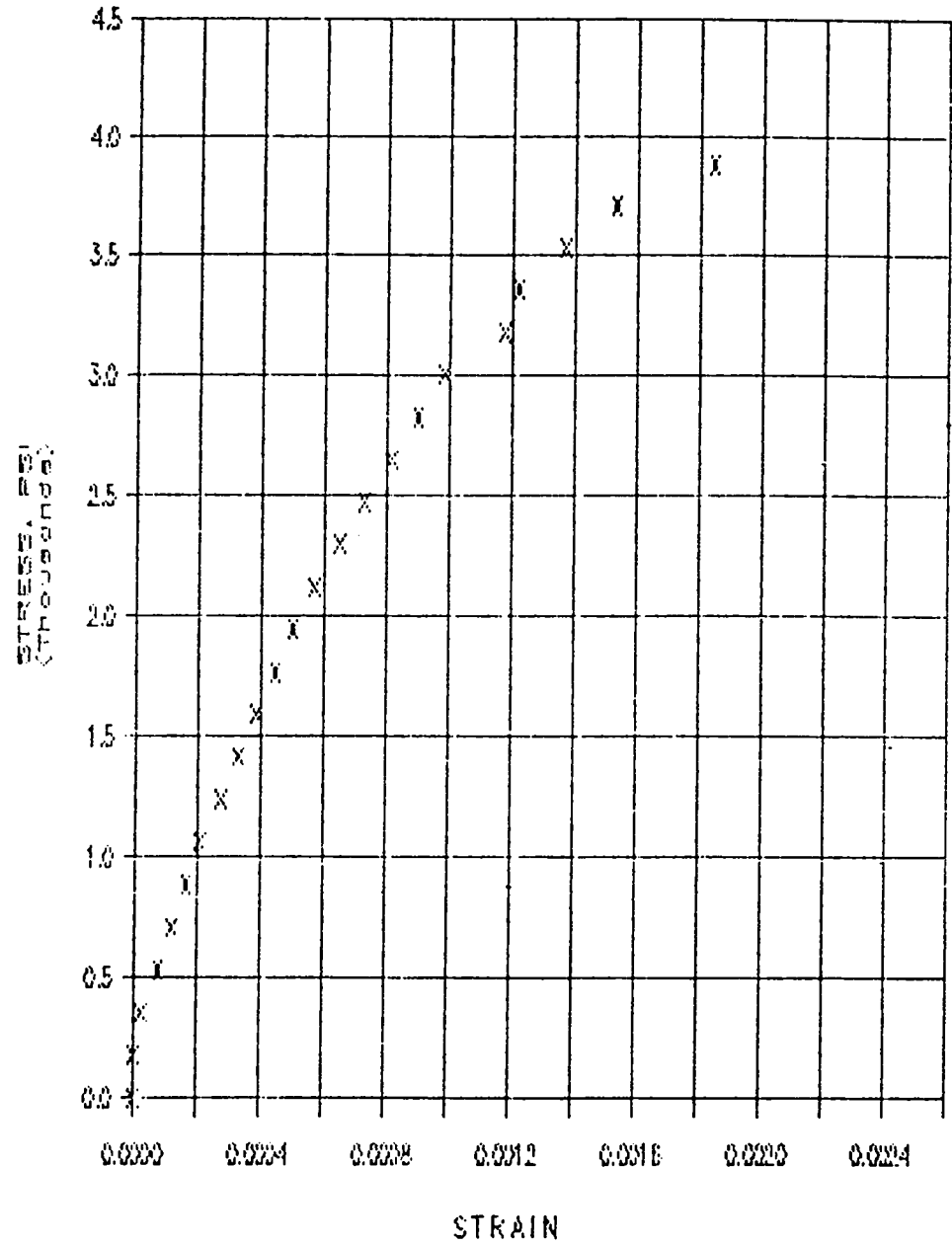


TEST DATA

MIX 2: SPECIMEN 10

DATE TESTED: 1/26/87

LOAD (LBS) *1000	STRESS (PSI)	READING (IN) *0.0001	DEFORM. (IN) *0.0001	STRAIN
0.0	0.00	0	0.0	0.00000
5.0	176.84	0	0.0	0.00000
10.0	353.68	4	2.0	0.00003
15.0	530.52	12	6.0	0.00008
20.0	707.36	19	9.5	0.00012
25.0	884.20	26	13.0	0.00016
30.0	1061.03	33	16.5	0.00021
35.0	1237.87	43	21.5	0.00027
40.0	1414.71	52	26.0	0.00033
45.0	1591.55	61	30.5	0.00038
50.0	1768.39	71	35.5	0.00044
55.0	1945.23	80	40.0	0.00050
60.0	2122.07	91	45.5	0.00057
65.0	2298.91	104	52.0	0.00065
70.0	2475.75	116	58.0	0.00073
75.0	2652.59	130	65.0	0.00081
80.0	2829.43	144	72.0	0.00090
85.0	3006.28	157	78.5	0.00098
90.0	3183.12	180	94.0	0.00118
95.0	3359.94	195	97.5	0.00127
100.0	3536.78	219	109.5	0.00137
105.0	3713.62	245	122.5	0.00157
110.0	3890.46	295	147.5	0.00184
112.0	3961.19	FRACTURE		



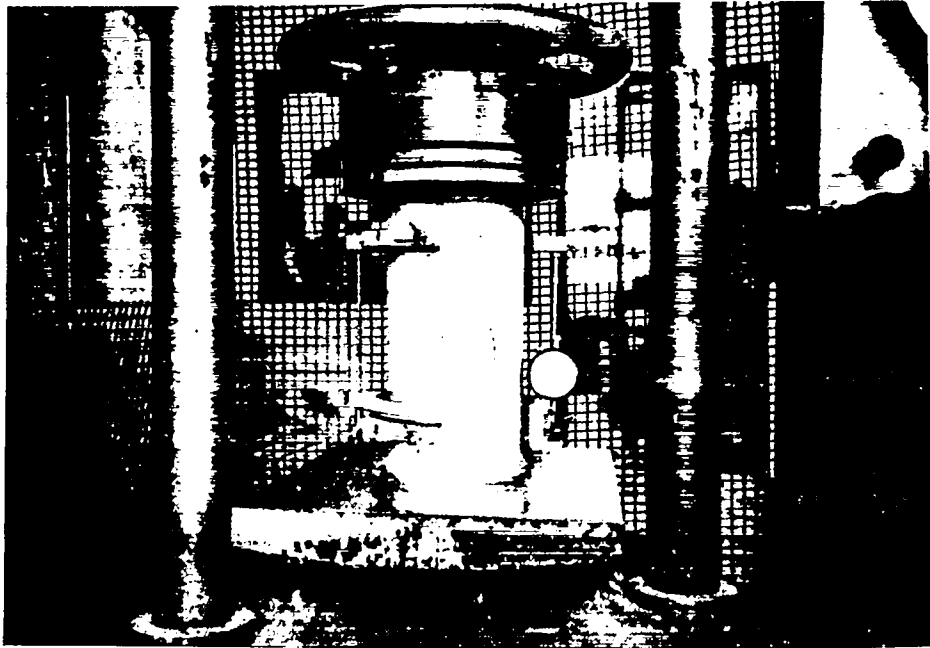


Fig. B-1. Compression test set-up.

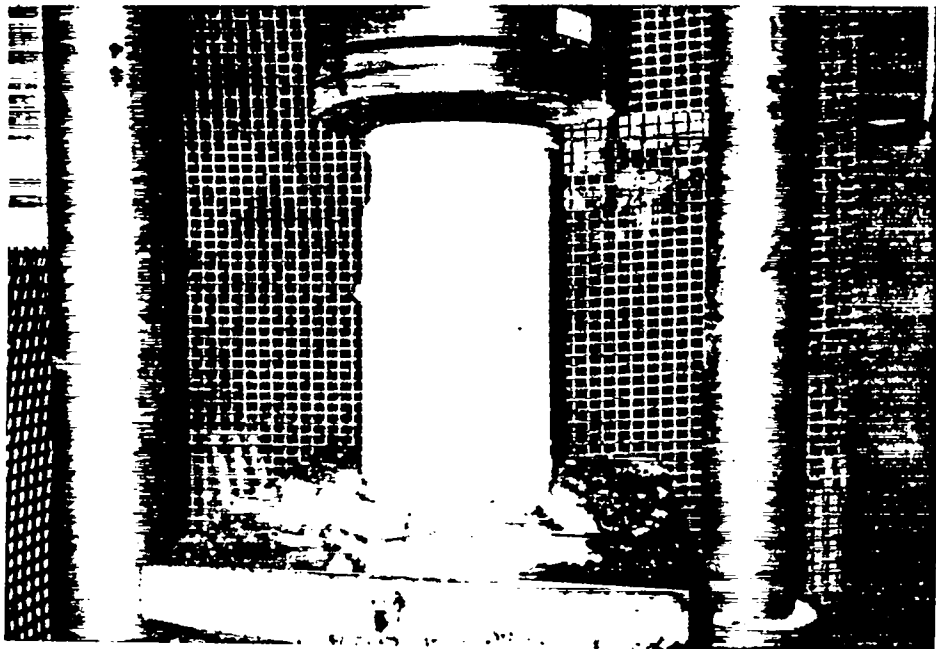


Fig. B-2. Failed compression test specimen.



Fig. B-3. Failure mode of compression test specimen.

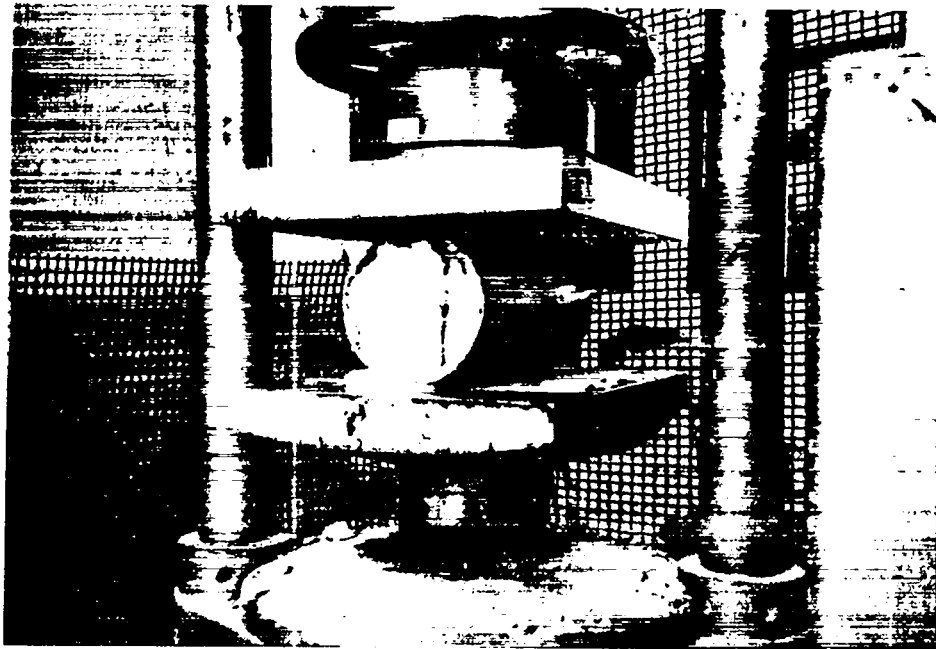


Fig. B-4. Indirect tension test set-up.

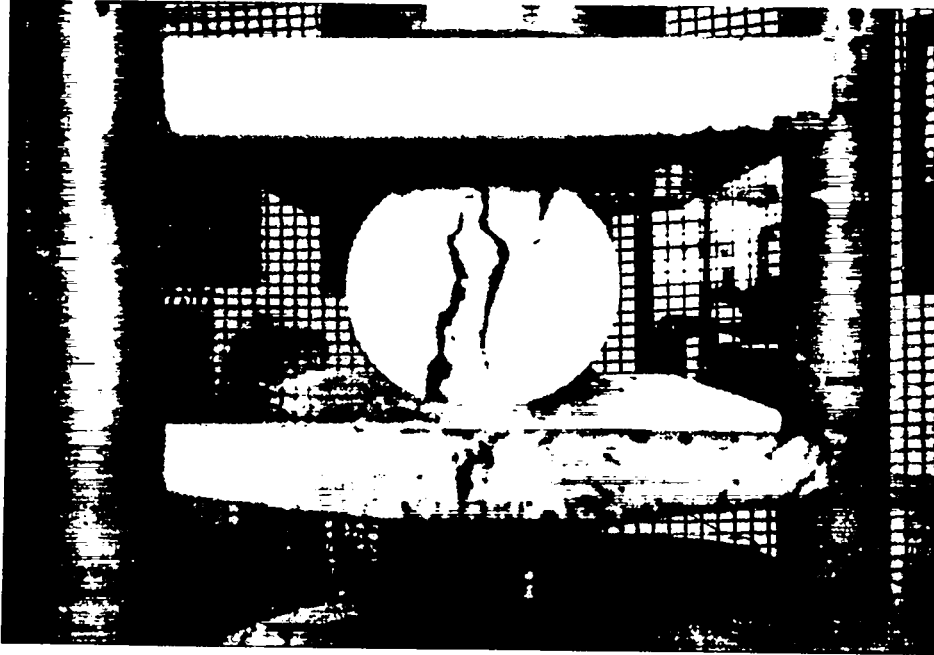


Fig. B-5. Failed tensile test specimen.

APPENDIX C

ULTRASONIC INSPECTION OF TRG-4

218 Fourth Avenue  
Edwardsville IL 62025

**LUKE M.  
SNELL, P.E.**  
CONSTRUCTION & MATERIALS CONSULTANT

Office: (618) 692-25  
Home: (618) 692-06

January 21, 1987

Joel Bennett  
Los Alamos National Laboratory  
MS J576  
Los Alamos, NM 87545

Subject: Inspection of TRG-4 Model  
Los Alamos National Laboratory  
Los Alamos, New Mexico  
Our Job No. LS88-341

Gentlemen

The writer has completed the inspection of the above referenced model. The purpose of this inspection was to determine the uniformity of the concrete and to determine if the concrete contained flaws. This report documents our findings.

On January 15, 1987, the writer examined the TRG-4 model. The examination consisted of two separate inspections. The first was a visual inspection using hand-held magnifying glasses. The second inspection was to determine the velocities of ultrasonic waves through the concrete.

The visual inspection indicated that the model did not appear to have external flaws.

The velocity of the ultrasonic wave was determined by measuring the wall thickness and measuring the time for the ultrasonic wave or a pulse to travel from a sending transducer, through the concrete to a receiving transducer; the velocity of the ultrasonic wave or the pulse velocity was then calculated by: pulse velocity = distance divided by time.

Past experience and research has shown that the pulse velocity value can be related to concrete strength and the static modulus of elasticity. Also if the pulse velocities are relatively uniform, then the concrete is of uniform quality and without flaws.

The equipment is generically called pulse velocity equipment. Our equipment is manufactured by James Electronic Company and is called the V-meter.



During our testing the following was determined:

1. Test Cylinders: Four 6 x 12 inch cylinders were examined to determine pulse velocities (2 from each load of concrete). These pulse velocities range from 13,160 to 13,510 feet per second with an average velocity of 13,290 feet per second.
2. Shearwall: 63 pulse velocities were determined for the shear wall. These pulse velocities ranged from 11,900 to 14,710 feet per second with an average of 13,260 feet per second. The wall was assumed to be uniformly 6 inches. The areas of the lowest pulse velocities appeared to be where the forms have moved during construction and where the walls may be greater than 6 inches thick. (NOTE: The variation in wall thickness appears to be less than 1/4 inch).
3. Base: 24 pulse velocities were determined on the base. The pulse velocities ranged from 14,150 to 15,300 feet per second with an average velocity of 14,770 feet per second.
4. Roof: 50 pulse velocities were determined on the roof. The pulse velocities ranged from 13,640 to 15,000 feet per second with an average velocity of 14,190 feet per second.
5. Northwest Wing Wall: 12 pulse velocities were determined on this wing wall. These pulse velocities ranged from 12,500 to 14,290 feet per second with an average velocity of 13,250 feet per second.
6. Northeast Wing Wall: 12 pulse velocities were determined on this wing wall. These pulse velocities ranged from 12,500 to 13,900 feet per second with an average velocity of 13,270 feet per second.
7. Southwest Wing Wall: 12 pulse velocities were determined on this wing wall. These pulse velocities ranged from 12,820 to 14,290 feet per second with an average velocity of 13,220 feet per second.
8. Southeast Wing Wall: 12 pulse velocities were determined on this wing wall. These pulse velocities ranged from 12,500 to 13,900 feet per second with an average velocity of 13,270 feet per second.

The pulse velocities of the four concrete cylinders were nearly identical. This indicates that the concrete strength and static modulus of elasticity for each load of concrete would be similar.

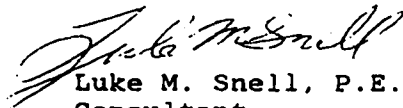
The pulse velocities in the model were fairly uniform and similar to the pulse velocities of the tested cylinders. This indicates that the concrete in the structure is of uniform quality and that the concrete strength and static modulus of elasticity of the model can be accurately determined from the concrete cylinders.

Since the pulse velocities were fairly uniform and the visual inspection did not indicate any external flaws, it is our opinion that the concrete model does not contain internal flaws.

The use of pulse velocities to estimate compressive strength and static modulus of elasticity is inexact and should be used only to indicate approximate values. Using the generalized data developed from past research, the compressive strength would be in excess of 3,000 psi and static modulus of elasticity would be in excess of 3,000,000 psi.

It has been a privilege working with you on this project. If you have any questions or if we can be of further service, please do not hesitate to call.

Very truly yours,

  
Luke M. Snell, P.E.  
Consultant

# FIELD MEASUREMENTS

## Cylinders - 6 x 12 inches

First Truck	Time x 10 <sup>-6</sup> seconds
Cylinder 1	76
Cylinder 2	76
Second Truck	
Cylinder 1	75
Cylinder 2	74

## SHEAR WALL - THICKNESS = 6 INCHES

Readings on approximately one foot intervals; measured from east wall.

Distance from base (inches)	Time x 10 <sup>-6</sup> seconds
3	36, 35, 34, 37, 35, 37, 37
17	35, 38, 35, 35, 37, 38, 37
25	38, 36, 34, 39, 36, 39, 38
37	40, 40, 38, 41, 39, 39, 40
49	38, 39, 37, 38, 39, 37, 37
61	39, 37, 37, 37, 39, 39, 36
73	38, 39, 40, 36, 37, 37, 37
82	39, 40, 38, 38, 38, 38, 38
88	38, 42, 38, 39, 38, 38, 38

BASE - THICKNESS = 8 INCHES

Readings on approximately one foot intervals.

North Base,	Time in $10^{-6}$ seconds
20 inches from East Wing Wall	50, 51, 51, 52, 51, 49
20 inches from West Wing Wall	51, 50, 52, 52, 53, 53

South Base,	
20 inches from East Wing Wall	50, 49, 51, 50, 49, 50
20 inches from West Wing Wall	49, 50, 51, 52, 52, 51

ROOF - THICKNESS = 8 INCHES

Readings on approximately one foot intervals.

North Roof	Time in $10^{-6}$ seconds
3 inches from East Wing Wall	54, 54, 54, 54, 54, 55
Centerline	51, 53, 52, 53, 53, 54
3 inches from West Wing Wall	54, 54, 55, 55, 54, 55
At Shear Wall	53, 53, 53, 54, 54, 52, 53

South Roof	
3 inches from East Wing Wall	51, 53, 52, 53, 53, 52
Centerline	53, 53, 51, 50, 53, 51
3 inches from West Wall	51, 51, 51, 52, 52, 52
At Shear Wall	53, 52, 52, 53, 53, 53, 53

WING WALLS - THICKNESS = 6 INCHES

Reading on approximately 15 inch intervals.

Measured from Base (inches)	Time x 10 <sup>-6</sup> seconds
<b>North-West</b>	
3	35, 37, 37
39	37, 39, 37
64	36, 39, 40
88	39, 38, 39
<b>North-East</b>	
3	35, 37, 39
39	39, 37, 37
64	36, 38, 36
88	38, 40, 40
<b>South-West</b>	
3	39, 37, 39
39	36, 35, 38
64	37, 39, 39
89	38, 39, 38
<b>South-East</b>	
3	36, 36, 38
39	40, 38, 38
64	38, 36, 37
88	39, 37, 39

## APPENDIX D

### METHODS FOR SEPARATING SHEAR AND BENDING DEFORMATION

This appendix provides the analysis and procedures used for data reduction and for designing the instrumentation for separating bending and shear stiffnesses.

The displacement field over the entire shear wall is non uniform; hence, the discussion of data reduction must begin by defining the deformation quantities to be measured.

## DEFINITIONS

Total Deformation. Total deformation is defined as the sum of the bending deformation and shear deformation:

$$\underline{\Delta} = \underline{\Delta B} + \underline{\Delta S} \quad , \quad (D-1)$$

where

$\underline{\Delta}$  = total deformation,

$\underline{\Delta B}$  = bending deformation,

$\underline{\Delta S}$  = shear deformation.

The underline indicates that the deformations are vector quantities. The total deformation, as defined, is related to certain appropriate measured displacements on the model during a test, and, in terms of measurements, it has the form

$$\underline{\Delta} = \underline{\Delta X} + \underline{\Delta Y} \quad , \quad (D-2)$$

where  $\underline{\Delta X} + \underline{\Delta Y}$  are defined in Fig. D-1.  $\underline{\Delta X}$  and  $\underline{\Delta Y}$  could be determined for either the upper left or right corner of the model. Any difference would be dependent upon the rigidity of the top plate in the model. The coordinate system defined in Fig. D-1 is the one used throughout this appendix.

Shear Deformation. Shear deformation is defined as the displacement in the X direction of the top of a model when deformed in simple shear, or

$$\underline{\Delta S} = H \tan \gamma \underline{e}_x \approx H \gamma \underline{e}_x \quad , \quad (D-3)$$

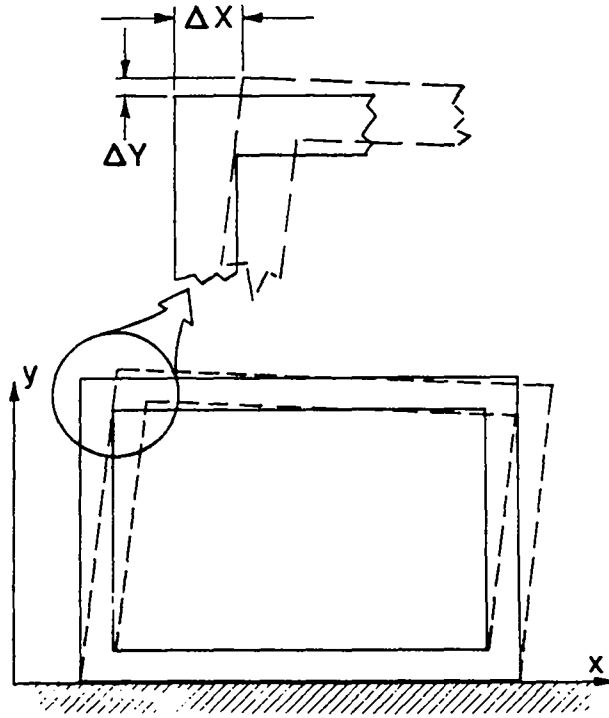


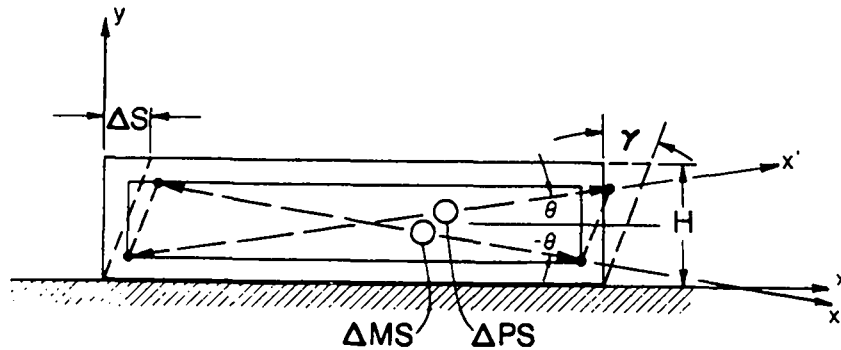
Fig. D-1. Component of total deformation.

where

- $\Delta S$  is the shear deformation,
- $H$  is the height of the model,
- $\gamma$  is the homogeneous shear strain,
- $e_x$  is the unit vector in the  $x$  direction.

Figure D-2 illustrates this quantity. In Eq. (D-3), it is assumed that the shear deformation is small, or  $\gamma = \tan \gamma$ . The value of  $\gamma$  used in calculating  $\Delta S$  from measurements will be the average shear strain over the height of the model. The shear strain at the center could also be used, but, because there is some gradient in shear strain, the average over the model is more useful in describing the overall shear deformation.





- NOTES: 1. SKETCH DRAWN WITH A LOW-ASPECT RATIO TO EMPHASIZE THE SHEAR DEFORMATION
2.  $\Delta MS$  AND  $\Delta PS$  ARE THE CHANGES IN THE LENGTH SHOWN

Fig. D-2. Displacement measurements for determining shear deformation.

The average shearing strain may be found by using the indicator reading on the two diagonals shown in Fig. D-2 to find the normal strain along each diagonal and then by using the strain transformation equation to find shearing strain in the  $x$ - $y$  coordinate system. Specifically,

$$\epsilon_x' = \frac{\Delta PS}{L_i} \quad (D-4)$$

$$\epsilon_x'' = \frac{\Delta MS}{L_i} \quad (D-5)$$

where

$\epsilon_x'$  is the normal strain along the diagonal having the positive slope,

$\epsilon_x''$  is the normal strain along the diagonal having the negative slope,

$L_i$  is the initial length of the diagonal.

For the case of pure shear, the normal strains,  $\epsilon_x$  and  $\epsilon_y$ , in the x-y coordinate system are zero, and, for this case, the strain transformation equations become

$$\epsilon_x' = \frac{\gamma}{2} \sin 2\theta \quad , \quad (D-6)$$

$$\epsilon_x'' = \frac{\gamma}{2} \sin (-2\theta) \quad , \quad (D-7)$$

where

$\theta$  is the angle between the unprimed and primed axis.

For pure shear,  $\epsilon_x'$  and  $\epsilon_x''$  would be equal in magnitude. To determine an average value for the shear strain, the equation

$$\left| \gamma_{\text{avg}} \right| = \frac{(|\Delta PS| + |\Delta MS|)}{L_j \sin 2\theta} \quad , \quad (D-8)$$

is obtained. The shear deformation is defined in terms of this average shear strain value.

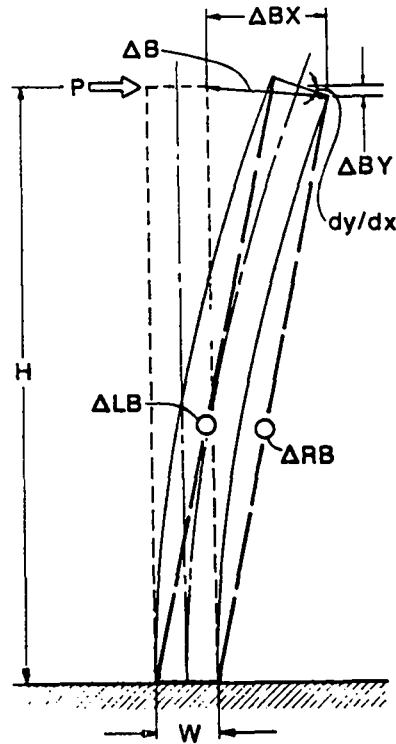
Bending Deformation. Bending deformation is defined as the displacement of an end corner of the cantilevered model as determined from simple beam theory. Figure D-3 shows this quantity and defines the terms to be used in the following derivations. From Fig. D-3,

$$\Delta B = \Delta BX + \Delta BY \quad . \quad (D-9)$$

Hence, the bending deformation is defined in terms of the displacement of either of the top corners of the model, as evaluated using beam theory. From beam theory,

$$\Delta BX = \frac{PH^3}{3EI} \quad , \quad (D-10)$$

and



- NOTES: 1. SKETCH DRAWN WITH AN ASPECT RATIO TO EMPHASIZE THE BENDING DEFORMATIONS  
 2.  $\Delta LB$  AND  $\Delta RB$  ARE THE CHANGES IN THE LENGTHS SHOWN

Fig. D-3. Displacement measurement for determining bending deformation.

$$\Delta BY = \frac{W}{2} \left. \frac{dy}{dx} \right|_H = \frac{W(PH^2)}{2(2EI)}, \quad (D-11)$$

where

P is the load applied to the end of the beam,

H is the height of the beam,

E is the modulus of elasticity,

I is the cross-sectional moment of inertia,

$\left. \frac{dy}{dx} \right|_H$  is the slope at the end of the beam,

W is the depth of the beam.

The relative displacement measurements made during a test that will be used to calculate  $\Delta BX$  and  $\Delta BY$  are defined in Fig. D-3 as  $\Delta LB$  and  $\Delta RB$ . These quantities are the changes in the defined dimensions. The derivation of the equations is based upon linear beam theory as follows:

$$\Delta LB = \int_0^H \epsilon_y dy \quad , \quad (D-12)$$

where

$\epsilon_y$  is the strain in the outer beam fiber, and

because  $\sigma_y = E \epsilon_y$  ,

$$\Delta LB = \int_0^H \frac{\sigma_y}{E} dy \quad . \quad (D-13)$$

For a cantilever beam,  $\epsilon_y$  varies linearly with  $y$ , hence,

$$\Delta LB = \frac{P(W/2)}{IE} \int_0^H y dy = \frac{PWH^2}{4EI} \quad , \quad (D-14)$$

and, similarly,

$$\Delta RB = - \frac{PWH^2}{4EI} \quad . \quad (D-15)$$

Using the deflection of the end of a cantilever beam ,

$$\Delta BX = \frac{PH^3}{3EI} \quad , \quad (D-16)$$

and, assuming that the average of the measured quantities is proportional to  $\Delta BX$ ,

$$\Delta BX = \frac{K(\Delta LB - \Delta RB)}{2} = \frac{PH^3}{3EI} \quad . \quad (D-17)$$

Here,  $K$  is the proportionality constant. By eliminating  $K$ ,  $P$ ,  $E$ , and  $I$  from the previous equation, the deflection may be expressed as

$$\Delta BX = \frac{2H}{3W} (\Delta LB - \Delta RB) \quad . \quad (D-18)$$

Using the slope equation,  $\Delta BY$  may be found from

$$\left. \frac{dy}{dx} \right|_H = \frac{PH^2}{2EI} \quad , \quad (D-19)$$

$$\Delta BY = \frac{W}{2} \frac{PH^2}{2EI} = \frac{W}{2} \frac{3\Delta BX}{2H} \quad , \quad (D-20)$$

$$\Delta BY = \frac{3W}{4H} \Delta BX \quad . \quad (D-21)$$

The bending deflection magnitude  $\Delta B$ , is given by

$$\Delta B = (\Delta BX^2 + \Delta BY^2)^{1/2} \quad . \quad (D-22)$$

The total deformation has now been defined two ways. One way is based upon measurements of the  $x$  and  $y$  deflection of the upper right or left corner of a structure, as shown in Fig. D-1. The second method is to use the relative displacement measurements as defined in Figs. D-2 and D-3. When the relative displacement measurements are used, the equation for total deformation magnitude is

$$\Delta = [(\Delta S + \Delta BX)^2 + (\Delta BY)^2]^{1/2} \quad . \quad (D-23)$$

As a result of the assumptions made in deriving the above equation, one would not expect exact agreement between the total deformation values as determined by these two methods.

#### COMPARISON OF RESULTS FROM ANALYSIS

The deformation definitions previously discussed will now be applied to the displacement fields of the TRG-4 test structure as determined by a two-dimensional, plane stress, elastic, finite element model. A point load was applied to the lower steel plate on an finite element model to simulate the actual loading condition. Eight node plane stress elements were used in the two-dimensional model of TRG-4 as shown in Fig. D-4. The bottom concrete slab was not modeled in the two-dimensional analysis, and nodes that would correspond to the shear wall/bottom slab interface were fully constrained. Measured average material properties were used in the analyses. This work was done to study the applicability of the definitions, the resolution of the transducers needed, and other characteristics of the measurement method. The applied load subjected the model to an average base shear stress of 100 psi. The deformed mesh for the structure shown in Fig. D-5. The results from the numerical model included displacements and strains ( $\epsilon_x$ ,  $\epsilon_y$ ,  $\gamma_{xy}$ ) extrapolated to the node points. These results were used to determine the following quantities:

1. Gage readings of the deformation measurements described in Section 1.
2. Shear strain based upon the diagonal gage readings.
3. Shear deformation based upon diagonal gage readings and the shear strain at a location near the center of the shear wall.
4. Bending deformation based upon the vertical gage readings.
5. Total deformation from the displacements at the top of the model ( $\Delta X$  and  $\Delta Y$ ) and from the vertical and diagonal gage readings.

Table D-1 summarizes the pertinent data obtained from the finite element model analysis, and the calculations using the TRG-4 data are described in detail below.

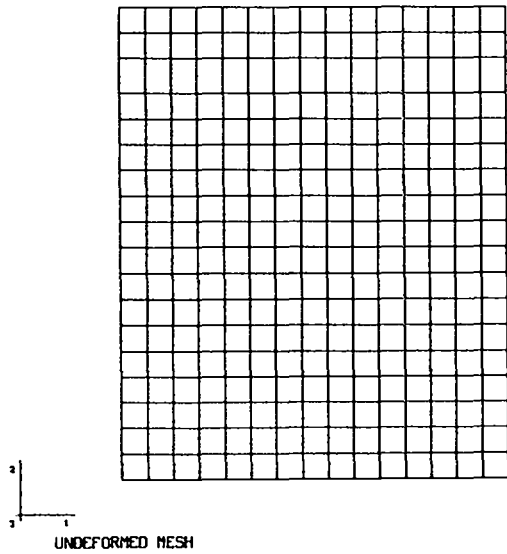


Fig. D-4. Two-dimensional finite element model of TRG-4.

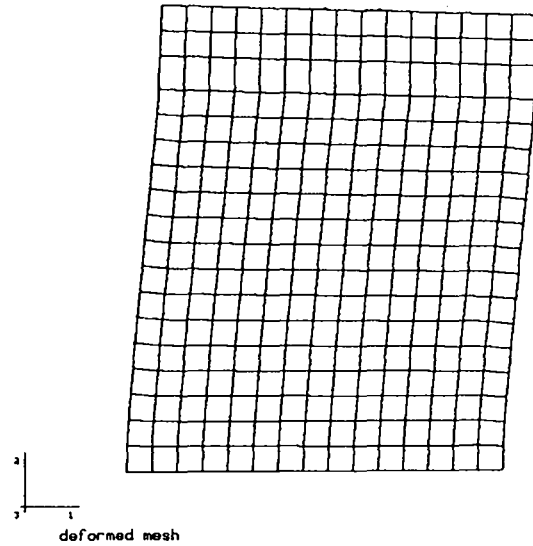


Fig. D-5. Deformed shape of TRG-4 when subjected to 54,000-lb load.

TABLE D-1

DATA FROM 2-D FINITE ELEMENT ANALYSIS OF TRG-4<sup>a</sup>

<u>Node<sup>b</sup></u>	<u>Horizontal Displacement <math>\Delta x</math> (in.)</u>	<u>Vertical Displacement <math>\Delta Y</math> (in.)</u>
1	0	0
2	$6.9514 \times 10^{-3}$	$-7.1860 \times 10^{-4}$
3	$6.9398 \times 10^{-3}$	$1.0137 \times 10^{-3}$
4	0	0
5	$3.6339 \times 10^{-4}$	$1.7480 \times 10^{-5}$
6	$6.3004 \times 10^{-3}$	$-5.6096 \times 10^{-4}$
7	$6.2672 \times 10^{-3}$	$8.8734 \times 10^{-4}$
8	$3.3742 \times 10^{-4}$	$1.0625 \times 10^{-4}$
9	0	0
10	$3.3690 \times 10^{-4}$	$-2.2061 \times 10^{-4}$
11	$6.3315 \times 10^{-3}$	$-1.0032 \times 10^{-3}$
12	$6.9316 \times 10^{-3}$	$-1.0018 \times 10^{-3}$

<sup>a</sup> Total horizontal force = 54,000 lb.

<sup>b</sup> Node locations are shown in Fig. D-6. Nodes 5-8 correspond to the terminal points of the relative displacement gages.

<sup>c</sup> Shear strain at the center of the shear wall =  $73.04 \times 10^{-4}$  radians.

### Calculation Outline

Figure D-6 shows the location of the nodes whose displacements have been reported for TRG-4 in Table D-1. Nodes 1 and 4 have no displacement components because they were constrained by the fixed boundary condition assumed to be provided by the bolted, rigid base. The diagonal gages shown in Fig. D-2 were assumed to run from Node 1 to Node 3 and from Node 4 to Node 2. The vertical gages shown in Fig. D-3 were assumed to run from Node 1 to Node 2 and from Node 3 to Node 4. Based on the displacements computed for the four nodes, the readings on the four gages would be as follows:

In Fig. D-2,

$$\Delta PS = 5.311 \times 10^{-3} \text{ in.} \quad (D-24)$$

and

$$\Delta MS = -5.096 \times 10^{-3} \text{ in.}$$

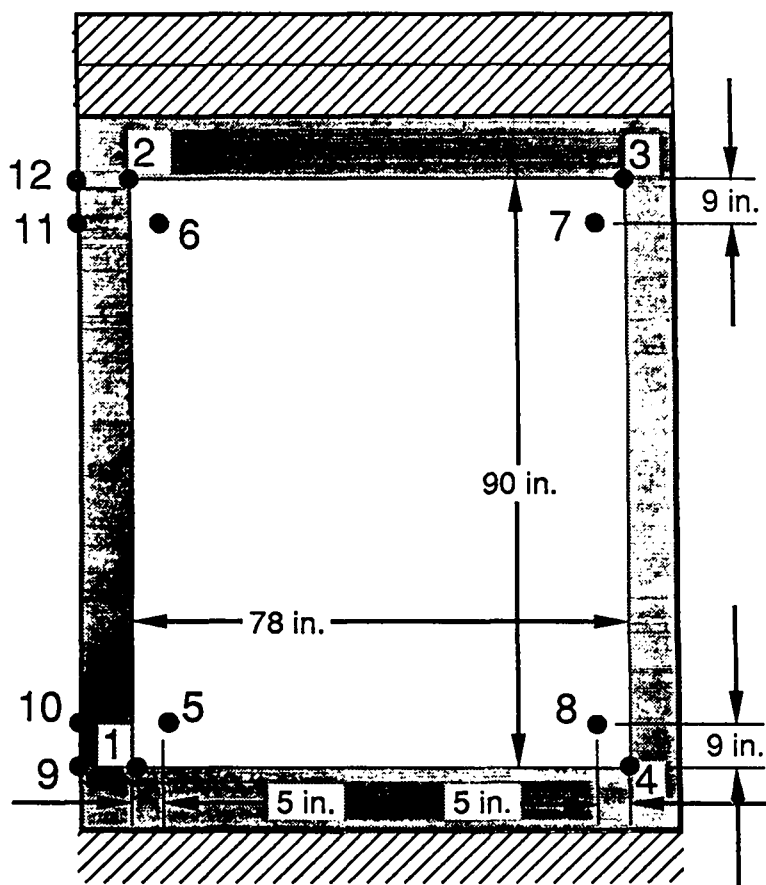


Fig. D-6. Sample problem node locations.



In Fig. D-3,

$$\Delta LB = 1.0140 \times 10^{-3} \text{ in.} \quad (D-25)$$

and

$$\Delta RB = -7.1833 \times 10^{-4} \text{ in.}$$

Even if these values are divided in half so that they correspond to the peak readings during a 50-psi cycle, the displacements will be detected by gages that can read accurately to  $4 \times 10^{-5}$  in.

It is assumed that the diagonal gages are measuring deformations caused by pure shear and that the average shear strain is given by Eq. (D-8).

In Eq. (D-8),  $L_i$  is the initial distance between Nodes 1 and 3 (or Nodes 2 and 4), and  $\theta$  is defined in Fig. D-2. Substituting the appropriate values from Eq. (D-8) yields

$$|\gamma_{avg}| = 66.07 \times 10^{-6} \text{ radians.} \quad (D-26)$$

It is again emphasized that this is an average strain value over the entire wall and that an actual wall and the computer model will have a nonuniform strain field. The average strain in the center element of the computer model was used for comparison. This strain value is

$$\gamma_{avg_c} = 73.04 \times 10^{-6} \text{ radians} \quad (D-27)$$

The lateral deformation of the top of the structure, assuming pure shear, is given by Eq. (D-3).

Using the values for the average shear strain calculated from the diagonal gage readings, the lateral deformation caused by shear is

$$\Delta S = 5.9461 \times 10^{-3} \text{ in.} \underline{e}_x \quad (D-28)$$

If the average shear strain for the center element in the finite element model is used, the lateral deformation becomes

$$\Delta S = 6.5736 \times 10^{-3} \text{ in. } \underline{e}_x \quad . \quad (D-29)$$

Now, if we assume that the vertical gages measure displacement caused purely by cantilever bending, then the displacement components are given by Eqs. D-18 and D-21. Substituting the appropriate values in those equations yields the following components of cantilever bending displacement:

$$\Delta BX = 1.4983 \times 10^{-3} \text{ in.}, \quad (D-30)$$

and

$$\Delta BY = 9.7390 \times 10^{-4} \text{ in.} \quad (D-31)$$

The magnitude of the total bending deformation is given by Eq. (D-22).

Substituting the components of the bending deformation in Eq. (D-22) yields

$$\Delta B = 1.7870 \times 10^{-3} \text{ in.} \quad (D-32)$$

The total deformation was defined as the vector sum of the deformation caused by bending and deformation caused by shear. Remembering that the deformation caused by shear has a component in the horizontal direction only, the magnitude of the total deformation is given by Eq. (D-23),

$$\Delta = 7.5078 \times 10^{-3} \text{ in.} \quad (D-33)$$

This value can be compared with the magnitude of the total deformation computed at either Node 2 or Node 3. For Node 2,

$$\Delta_2 = 7.0134 \times 10^{-3} \text{ in.}, \quad (D-34)$$

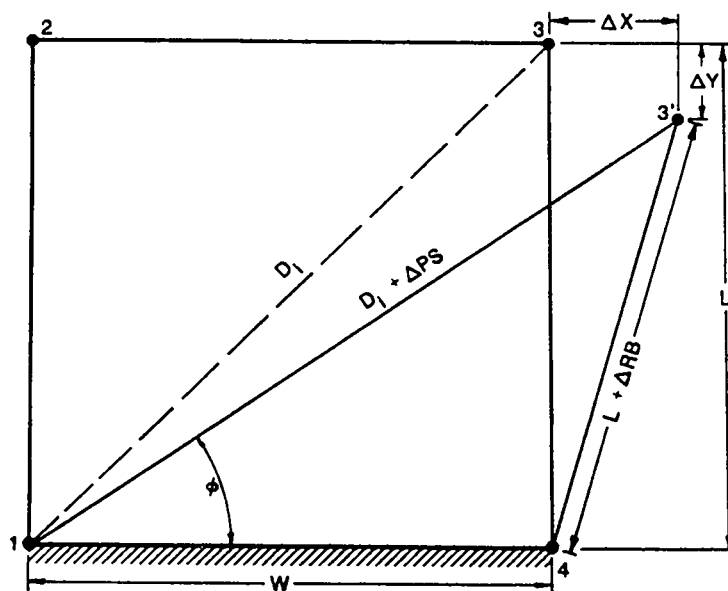
and, for Node 3,

$$\Delta_3 = 6.9884 \times 10^{-3} \text{ in.} \quad (D-35)$$

The total deformation as determined from the sum of the average shear and pure cantilever bending displacement components is about 7.2% larger than either of the computed displacements (Node 2 or Node 3). This increase comes as no surprise because the diagonal gages, from which the shear deformations were determined, give an average value of shear strain in the wall, and they may be influenced by the cantilever bending (or bending moment gradient) in the wall. Similarly, the vertical gages from which the bending deformation is determined may be influenced by the shear deformations. Hence, perfect agreement cannot be expected.

This data reduction method has been suggested because it permits independent determination of bending deformation and shear deformation which prevents errors or the effects of departure of actual behavior from idealized behavior in one of the deformation quantities from introducing errors or uncertainties in the other.

A third method for determining the total deformation can be developed by examining Fig. D-7. From Fig. D-7,



$$\Delta X = (D_1 + \Delta PS) \cos \phi - W$$

$$\Delta Y = (D_1 + \Delta PS) \sin \phi - L$$

$$\phi = \cos^{-1} \left[ \frac{W^2 + (D_1 + \Delta PS)^2 - (L + \Delta RB)^2}{2 W (D_1 + \Delta PS)} \right]$$

$\Delta PS$  = DIAGONAL DISPLACEMENT GAGE READING

$\Delta RB$  = VERTICAL DISPLACEMENT GAGE READING

Fig. D-7. A third method for calculating total deformations.

$$\Delta X = (D_i + \Delta PS) \cos \phi - W \quad , \quad (D-36)$$

$$\Delta Y = (D_i + \Delta PS) \sin \phi - L \quad , \quad (D-37)$$

$$\phi = \cos^{-1} \frac{W^2 + D_i + \Delta PS^2 - (L + \Delta RB)^2}{2 W D_i + \Delta PS} \quad . \quad (D-38)$$

This method eliminates the assumption that the angle  $\phi$  in Fig. D-2 remains unchanged during the deformation process. It was used to determine the total stiffness values reported in the main report.

It is of interest to use values in Eqs. (D-24)-(D-26) for the analytical deformation field on the shear wall presented in Table D-1, i.e., for

$$\Delta PS = 5.3111 \times 10^{-3} \text{ in.},$$

$$\Delta RB = -7.1833 \times 10^{-4} \text{ in.},$$

and

$$W = 78 \text{ in.},$$

$$L = 90 \text{ in.},$$

$$D_i = 119.0966 \text{ in.}$$

Rearranging Eq. (D-23) yields

$$\Delta S = -\Delta BX \pm \sqrt{\Delta^2 - \Delta BY^2} \quad , \quad (D-39)$$

and

$$\Delta S = 5.4224 \times 10^{-3} \text{ in.}$$

This compares with  $5.9461 \times 10^{-3}$  in. using the average strain method, an 8.8% difference. The deformations used to calculate the bending stiffnesses

reported in the main report were calculated as shown in Eq. (D-18). Shear deformations reported were calculated as shown in Eq. (D-39). For the ideal case, geometrically consistent results are obtained, i.e., the total deformation may be calculated from gage measurements, or the gage measurements may be calculated from the displacements.

Use of the diagonal displacement to calculate a total displacement does require that the diagonal gages and the vertical gages have the same terminal points. Also, the resulting total and shear deformation will not be for the complete shear wall but for the segment inside the gage points. A small amount of extrapolation to encompass the entire shear wall should be satisfactory for the precracked data. This extrapolation with the finite element analysis data produced negligible changes in the horizontal displacements when the data were extended along a horizontal plane to the exterior of the structure. Data for such a comparison are provided in Table D-1.

There is one potential advantage of using both the shear and bending deformations of the shear wall segment and the shear and bending deformations of the complete shear wall (based upon overall displacement measurements). Insight may be gained for understanding the contribution of the cracking at the wing wall joints by changing the proportion of the shear and bending deformation in the total deformation.

From the analysis of the numerical model, the following conclusions can be made. It must be remembered that these observations are based upon an analytical model loaded to a fairly low nominal shear stress level (100 psi).

1. The total deformation determined by the methods discussed in this appendix agree within 7.2%.
2. Measurement errors caused by the resolution of the digital displacement gages will not significantly affect the results.
3. The total deformation determined from displacements of the two top corners of the model agree within 1%.
4. The nonuniform distribution of shear strain causes the value of shear strain calculated from gage readings to be smaller than the value at the center of the shear wall as determined from the finite element analysis.

DISTRIBUTION

	<u>Copies</u>
Nuclear Regulatory Commission, RW, Laurel, Maryland	248
Technical Information Center, Oak Ridge, Tennessee	2
Los Alamos National Laboratory, Los Alamos, New Mexico	50
	<u>300</u>

NRC FORM 335 (2-84) NACM 1102, 3201, 3202 <b>BIBLIOGRAPHIC DATA SHEET</b> SEE INSTRUCTIONS ON THE REVERSE		U.S. NUCLEAR REGULATORY COMMISSION		1 REPORT NUMBER (Assigned by TSD; add Vol No., if any) NUREG/CR-5222 LA-11422-MS	
2 TITLE AND SUBTITLE Static Load Cycle Testing of a Low-Aspect-Ratio Six-Inch Wall TRG-Type Structure TRG-4-6 (1.0, 0.25)			3 LEAVE BLANK		
5 AUTHOR(S) Charles R. Farrar, Joel G. Bennett, Wade E. Dunwoody, and William E. Baker*			4 DATE REPORT COMPLETED MONTH: April      YEAR: 1989		
7 PERFORMING ORGANIZATION NAME AND MAILING ADDRESS (Include Zip Code) Los Alamos National Laboratory Los Alamos, NM 87545			6 DATE REPORT ISSUED MONTH: June      YEAR: 1989		
10 SPONSORING ORGANIZATION NAME AND MAILING ADDRESS (Include Zip Code) Division of Engineering Office of Nuclear Regulatory Research U.S. Nuclear Regulatory Commission Washington, DC 20555			8 PROJECT/TASK/WORK UNIT NUMBER  9 FIN OR GRANT NUMBER A7221		
12 SUPPLEMENTARY NOTES *Consultant at Los Alamos. Mechanical Engineering Department, University of New Mexico, Albuquerque, NM 87131.			11a TYPE OF REPORT Technical b PERIOD COVERED (Inclusive dates)		
13 ABSTRACT (200 words or less) <p>Quasi-static load cycle testing of a 6-in.-thick reinforced concrete shear wall structure is detailed in this report. The background of this program and results that led to this series of experiments are reviewed. Geometry of the test structure, design parameters, preliminary modal testing and analysis to verify undamaged dynamic properties, material property tests, instrumentation and results of this data reduction for stiffness, cracking values, and energy losses are given.</p> <p>Results are compared with other investigators' results, as well as with the American Concrete Institute 318-349 code predictions.</p>					
14 DOCUMENT ANALYSIS - a KEYWORDS DESCRIPTORS reinforced concrete structures stiffness				15 AVAILABILITY STATEMENT Unlimited	
b IDENTIFIERS OPEN ENDED TERMS				16 SECURITY CLASSIFICATION (This page) Unclassified (This report) Unclassified	
				17 NUMBER OF PAGES	
				18 PRICE	

**UNITED STATES  
NUCLEAR REGULATORY COMMISSION  
WASHINGTON, D.C. 20555**

**OFFICIAL BUSINESS  
PENALTY FOR PRIVATE USE, \$300**

**SPECIAL FOURTH-CLASS RATE  
POSTAGE & FEES PAID  
USNRC  
PERMIT No. G-67**